ON THE DETERMINATION OF BOILING WATER REACTOR CHARACTERISTICS BY NOISE ANALYSIS

ERIK KLEISS

Delftse Universitaire Pers

ON THE DETERMINATION OF BOILING WATER REACTOR CHARACTERISTICS BY NOISE ANALYSIS

ON THE DETERMINATION OF BOILING WATER REACTOR CHARACTERISTICS BY NOISE ANALYSIS

PROEFSCHRIFT ter verkrijging van
de graad van doctor in de
technische wetenschappen aan
de Technische Hogeschool Delft,
op gezag van de Rector Magnificus
prof. ir. B.P.Th. Veltman,
te verdedigen op
donderdag 16 juni 1983
te 14.00 uur door
ERIK BERNARDUS JOHANNES KLEISS
natuurkundig ingenieur
geboren te Schiedam

Delftse Universitaire Pers/1983

Dit proefschrift is goedgekeurd door
de promotor: Prof.dr.ir. H. VAN DAM

Aan mijn ouders
Aan alle vrienden

CONTENTS

Chapters 2 and 4 have been reprinted from Annals of Nuclear Energy with kind permission of Pergamon Press.
Chapter 3 has been reprinted from Nuclear Technology with kind permission of the American Nuclear Society.

SAMENVATTING.

In dit proefschrift wordt de analyse van ruissignalen van kokend-water reactoren (BWR's) behandeld. Omdat de belangrijkste ruisbron het kookproces in de reactorkern is en de belangrijkste variabele de neutronenflux, wordt de invloed van stoombellen op de neutronenflux gedetailleerd onderzocht.
In Hoofdstuk 2 wordt een experiment beschreven dat is uitgevoerd om in een kleine, onderkritieke reactor de responsie te meten van het signaal van een neutronen detector op de passage van een enkele luchtbel. Op deze wijze wordt het elementaire proces in een BWR gesimuleerd. Een theoretisch model voor de beschrijving van de responsie is getest en de resultaten stemmen goed overeen met de metingen. Daarnaast wordt een kwalitatieve verklaring van de metingen gegeven.
De overige hoofdstukken hebben betrekking op ruismetingen die verricht zijn in de kerncentrale te Dodewaard. In Hoofdstuk 3 wordt de constructie besproken van een tweeling self-powered neutronen detector, die ontwikkeld is om de snelheid te meten van de stoom in de splijtstofbundels. De detector-karakteristieken zijn bepaald en de detector blijkt goed geschikt te zijn voor deze toepassing.
In Hoofdstuk 4 wordt dieper ingegaan op het gedrag van de neutronenruis in het laagfrequente gebied. Hier worden afwijkingen van puntkinetica gevonden, die verklaard kunnen worden met een uitbreiding van de theorie van Hoofdstuk 2 naar vermogenscondities. Als een nuttig practisch gevolg blijkt het mogelijk te zijn om, uit het plaatsafhankelijk gedrag van de ruis, de overdrachtsfunctie tussen reactiviteit en reactorvermogen te bepalen.
In Hoofdstuk 5 wordt hier dieper op ingegaan. De uit de ruis bepaalde overdrachtsfuncties kloppen goed met die, welke gebaseerd zijn op onafhankelijke methoden: uit de meting van de responsie op een stapvormige beweging van een regelstaaf en uit modelberekeningen.
Hoofdstuk 6 behandelt het gebruik van het autoregressief model voor de analyse van de samenhang van een aantal signalen. Voor wat betreft neutronenflux, druk en stoomdebiet zijn de belangrijkste ruisbronnen bepaald. De kookruis is be-

langrijk, maar daarnaast treden ook onafhankelijke variaties in het stoomdebiet op (akoestische resonanties) en blijkt ruis in het regelsysteem van belang te zijn. Bovendien worden de overdrachtsfuncties tussen een aantal variabelen bepaald, waaruit schattingen verkregen kunnen worden voor enkele fysische grootheden die van belang zijn bij het reactorbedrijf.
In drie appendices worden metingen en theoretische onderwerpen behandeld die nodig zijn in hoofdstukken 4-6, maar die niet direct over de analyse van reactorruis gaan. In Appendix 1 worden de details besproken van de regelstaaf-stap experimenten, die werden gebruikt ter controle van de reactor overdrachtsfunctie die in Hoofdstuk 5 uit de ruis bepaald werd. Appendix 2 behandelt de achtergronden van de toepassing van het multivariate autoregressieve model bij ruisanalyse. Hierbij zijn enkele problemen die bij de practische toepassing kunnen onstaan opgelost en de methode wordt gedemonstreerd aan de hand van de analyse van enkele eenvoudige electrische netwerken. Tenslotte wordt in Appendix 3 een model afgeleid voor de dynamica van een kokend-water reactor en worden enkele resultaten voor de Dodewaard reactor gepresenteerd.

SUMMARY.

This thesis deals with the analysis of the noise signals in boiling water reactors. As the main noise source is the boiling process in the core and the most important variable the neutron flux, the effect of the steam bubbles on the neutron flux is studied in detail.

Chapter 2 deals with an experiment, performed in a small subcritical reactor, to measure the response of a neutron detector to the passage of a single air bubble. In this way the elementary process in a BWR is simulated. A mathematical model for the description of the response was tested and the results agree very well with the experiment. Also some attention is paid to the qualitative physical explanation.

The remaining chapters discuss noise measurements in the Dodewaard boiling water reactor in The Netherlands. Chapter 3 deals with the construction of a twin self-powered neutron detector, developed to perform steam velocity measurements in the core. Detector characteristics are measured and it appears that it is well suited for its purpose.

In chapter 4, the study concentrates on the low-frequency part of the neutron noise characteristics. Here deviations from a point-kinetics behaviour of the core are observed. An explanation can be obtained by an extension of the theory discussed in Chapter 2 to at-power conditions. As a useful practical result, it appears possible to determine the reactor transfer function between reactivity input and reactor power output, from the space-dependence of the neutron noise.

Chapter 5 goes deeper into the practical elaboration of this method. The resulting transfer functions exhibit a good agreement with ones obtained by independent means: control rod step experiments and model calculations.

In Chapter 6 the relations between several variables are studied with the use of autoregressive modelling techniques. The main noise sources in the reactor are identified in as far neutron flux, pressure and steam flow are concerned. Boiling noise is important, but also independent steam flow variations (acoustic waves) and control system noise play a substantial role. Furthermore the

transfer functions between several variables were obtained, yielding estimates for a number of parameters involved in reactor operation.
Three appendices are present which are not directly involved in the analysis of the Dodewaard noise, but which discuss measurements and theories necessary in the Chapters 4 to 6. Appendix 1 treats the control rod step experiments, used for an experimental validation of the noise-based reactor transfer functions obtained in Chapter 5. Appendix 2 deals with the application of the multivariate autoregressive modelling technique to the study of noise signals. Some newly discovered topics are discussed and the method is demonstrated by the analysis of some simple networks.
Finally, in Appendix 3 a model is derived for the dynamics of the Dodewaard boiling water reactor and some results are presented.

CHAPTER 1. INTRODUCTION AND OUTLINE.

Noise is a very general phenomenon in physical systems. It is the occurence of random fluctuations with time in the characteristic variables or output signals of the system under consideration. The causes for these fluctuations are manyfold; they range from the intrinsic probabilistic character of the elementary processes underlying the macroscopic system behaviour, to very clearly identifiable external perturbations. Often the presence of noise is considered a nuisance which limits the precision of measurements performed on the system, or which deteriorates system performance. However, if the noise is accepted as a phenomenon in its own right, useful results can be obtained from its analysis. This will be discussed in the following.

A general approach is to consider the observed noise as being caused by one or more noise sources, acting as inputs to the system. The characteristics of the output noise are determined by both noise source and system properties, e.g. spectral densities of the noise sources and transfer functions of the linear(ized) system. If the characteristics of the noise sources are known by some method, the system properties can be obtained. If on the other hand the system characteristics are available, the properties of the noise sources can be studied. Both alternatives have found their application to nuclear reactors.

For the case that reactor system properties are known sufficiently accurate, the noise sources can be investigated and the presence of 'abnormal' noise be detected. Excessive mechanical vibration of reactor components (with danger of wear or fatigue), insufficient coolant flow and associated unexpected coolant boiling (danger of fuel damage), loose parts and leakages in components are examples of topics that received much attention (1,2). It will be clear that this type of noise analysis can be of use in the safe operation of nuclear power plants; due to the generally large sensitivity of these techniques, it is expected that failures may be detected in an early stage before substantial damage to the plant occurs.

If the other approach is followed, the noise is considered as an actuating

input to the system and used to measure system properties. Noise analysis is sometimes able to yield parameters that are not or only with difficulty obtainable by other methods. Also, it may be impossible (technically or due to undesired interference with plant operation) to apply external input signals to the reactor system for the measurement of its response functions; the intrinsic noise is then a welcome alternative. The first applications of reactor noise analysis were based on this approach. The probabilistic nature of the fission process and neutron multiplication was already clear in the early years of reactor operation (3) and was used to measure e.g. criticality and neutron generation time. The success of these applications, often called zero-power reactor noise analysis, lies in the fact that the basic noise sources are very clear and the mathematical tools for its description were partly available from statistical physics (see e.g. 4). With the development of power reactors other noise generating processes, with less well-defined properties such as coolant density and temperature fluctuations due to turbulence and boiling, became important. Nevertheless, the noise sources can often be modelled sufficiently close or be measured to be used to obtain system properties. An early example is the stability monitoring of the EBWR (experimental boiling water reactor (5)), still a topic of interest(2). Another example is the measurement of coolant flow, also discussed in this thesis.
This type of noise analysis may contribute to a safe and economic operation of reactors, too. In the first place, measurements of physical parameters under operational conditions can be used as a check on the data and calculational methods applied in the design phase. This may lead to a reduction in conservative margins thus improving economic performance. Furthermore, monitoring of the system during fuel cycle may reveal slow deterioration of instrumentation, controller performance, dependence of stability on power and burnup conditions, etc.

This thesis focusses primarily on the second approach: the use of the intrinsic noise to measure system characteristics of boiling water reactors (BWR's). In these reactors, the boiling and steam transport processes in the core act as the dominating noise source. From reactor physical point of view, the interaction of this boiling noise with the neutron flux field in and around the reactor is one of the most interesting topics.
One description of the neutron flux response is the local/global concept of Wach and Kosaly (6). A steam bubble in the moderator gives rise to a neutron flux variation in its immediate vicinity (the local component, mainly due to decreased moderation). At the same time the neutron balance is influenced, so a reactivity effect occurs that affects the neutron flux in the core as-a-whole: the global component. This approach proved to be very fruitful in obtaining a qualitative understanding of the noise signals of incore neutron detectors used for the measurement of the steam velocity in the fuel bundles.

More quantitative results came available after the introduction of a method, based on perturbation theory, for the description of the detector responses (7-9). Chapter 2 of this thesis deals with an experiment that was carried out to test the applicability of this theory in practice. The response of a neutron detector to air bubbles injected in a small subcritical reactor was measured, thus simulating the BWR incore conditions in the laboratory.

The remaining chapters deal with the noise analysis of an actual BWR, the Dodewaard reactor; this is a small (54MWe), natural circulation boiling water reactor in The Netherlands. Chapter 3 deals with the development of a special neutron detector to be used for the accurate measurement of the steam velocity in the core of this reactor. As our research was not aimed at the study on two-phase flow and the validation of the design and operation programs, results obtained with this detector are not discussed. Instead, a study on the neutron flux behaviour is performed.

Apart from the explanation of the local noise component, the perturbation theory is in principle suited for a description of the global component, up to then generally neglected. For this purpose, the method had to be extended to include the effects of power variations on neutron cross sections. This is done in Chapter 4. In this way an explanation is found for the observed space-dependent effects in the low-frequency region of the noise. A direct result is the quantitative determination of the at-power reactor transfer function (RTF), outlined in Chapter 4 and discussed in more detail in Chapter 5. Due to the novelty of this rather indirect method, a validation must be obtained by comparison with independent methods. For this purpose experiments were performed with control rod movements to measure the RTF directly; these are discussed in Appendix 1. Also a theoretical model for the dynamic behaviour of the Dodewaard reactor was developed and is presented in Appendix 3.

In the course of the studies of Chapter 4 and 5, the necessity arose to introduce sophisticated methods for the analysis of the mutual interaction of many neutronic and process noise signals. The autoregressive modelling technique, not long before introduced into reactor noise work, seemed to offer good possibilities. Before a succesful application was possible, some pitfalls and theoretical problems had to be removed. These points are discussed in Appendix 2.

Apart from the applications of this method in Chapter 5, it appeared a powerful tool to obtain information on other reactor characteristics. Chapter 6 discusses the use of the developed methods to identify the most important noise sources in the reactor and to measure transfer functions between several variables and determine the associated physical parameters.

The three appendices form a rather substantial part of this thesis. As the treated topics do not directly discuss the analysis of reactor noise, they are added as appendices to avoid a disturbance of the main line of the chapters. However, the presented material forms a significant part of the research per-

formed.

This thesis is not meant as a documentation of the Dodewaard reactor and all its noise characteristics. The appreciation by the reader of the topics discussed will depend on his involvement in the trade. Although many details and conclusions may be specific for the Dodewaard reactor, it is believed that the developed techniques are fairly well applicable to other reactors.

CHAPTER 1.References.

1. SMORN-II, 2nd. Specialists meeting on reactor noise. M.M.R.Williams(ed). Progress in Nucl.Energy 1,73-804,(1977).
2. SMORN-III, 3rd. Specialists meeting on reactor noise. M.M.R.Williams(ed). Progress in Nucl.Energy 9,(1982).
3. Courant, E.D. and P.R.Wallace. Phys.Rev.72, 1038-1048,(1949).
4. Williams,M.M.R. Random Processes in Nuclear Reactors, Pergamon Press,(1974).
5. Thie,J.A. Nucleonics 17,102-109,(October 1959).
6. Wach,D. and G.Kosaly. Atomkerenergie 23,244-250,(1974).
7. Dam,H.van. Atomkernenergie 25,70-71,(1975).
8. Dam,H.van. Atomkernenergie 27,8-14,(1976).
9. Behringer,K., G.Kosaly and Lj.Kostic. Nucl.Sci.Eng. 63,306-318,(1977).

Annals of Nuclear Energy, Vol. 6, pp. 385 to 398
Pergamon Press Ltd 1979. Printed in Great Britain

ANALYSIS OF NEUTRON DETECTOR RESPONSE TO BUBBLES IN A WATER MODERATED REACTOR

E. KLEISS and H. VAN DAM
Interuniversity Reactor Institute, Mekelweg 15, Delft, The Netherlands

(*Received* 8 *January* 1979, *in revised form* 26 *February* 1979)

Abstract—The influence of air bubbles on the signal of a neutron detector has been investigated in a water moderated subcritical assembly using an average response technique. Qualitative and quantitative models are developed to explain the measured detector response. The quantitative one, based on perturbation theory, is in good agreement with experimental results.

1. INTRODUCTION

The formation and transport of steam bubbles is a very important source of the noise in boiling water reactors. Study of this noise can, in principle, reveal much information that is important for plant operation, e.g. steam velocities, void fraction and thermal hydraulic instabilities. In recent years much work has been carried out in this field, both experimentally and theoretically.

On the experimental side, void velocity and fraction are obtained and other two-phase flow characteristics were studied using the noise signals of both in- and ex-core neutron detectors (Ashraf Atta *et al.*, 1978; von Ceelen *et al.*, 1976; Crowe *et al.*, 1977; Kosaly *et al.*, 1977a).

On the theoretical side, models are developed to compute the response of an in-core neutron detector to steam bubbles. The idea behind this is that once the response of a detector to steam bubbles is known correctly, important information about the bubble flow can be derived from measurements of in-core neutron detector signals. Wach and Kosaly (1974) proposed the 'local-global' concept, founded on observed interference effects in the power spectral densities of in-core detectors. Here the global component of the noise was assumed to be the reactivity noise (partly caused by the steam bubbles), while the local effect was interpreted as the flux change in the vicinity of the detector. Following this, models were constructed to compute the local part of the response (Fuge, 1975; Kosaly and Mesko, 1976; Kosaly *et al.*, 1973; Kosaly, 1975).

A theoretical base was suggested by van Dam (1975, 1976), who applied time-dependent perturbation theory to compute the response of a neutron detector to bubbles. In a two-group model the connection with the local–global concept was apparent via the two relaxation lengths that apply to the neutron transport process (van Dam, 1975, 1976; Behringer *et al.*, 1976).

This paper deals with the results of experiments that were carried out in order to check the validity of the perturbation model, and tries to get a better insight into the processes that play a role in the origin of the response. In a subcritical assembly a BWR was simulated by injecting air bubbles into the water moderator. A neutron source and a neutron detector were present in the system and the influence of the bubbles on the signal of the neutron detector was measured using an average-response technique. The experiment is described in more detail in Section 4. In the next two Sections a qualitative model and a quantitative perturbation model for the description of the detector response are presented. In Section 5 the experimental results are displayed and compared with theory. Finally, in the appendices some comments on the computations are given.

2. QUALITATIVE DESCRIPTION OF THE DETECTOR RESPONSE

From the reactor physical point of view, the steam bubbles in the moderator can be treated as local changes in the macroscopic cross sections. These changes affect the behaviour of the neutron population. In this section we will consider the changes in detection probability for neutrons, due to cross section changes in the reactor, in a qualitative way, starting from the elementary interactions between neutrons and the moderator material: capture and scattering. It is appropriate to split the effects of scattering into two components: energy-change

("moderation") and direction change and following movement of the neutrons (here indicated as "diffusion").

We assume no changes in the fission cross section because the bubbles are formed in the moderator material and second order effects like spectral changes are neglected.

2.1. *Capture*

Introduction of a bubble into the moderator implies removal of neutron capturing material. The probability of the neutron being detected will increase because it has a greater chance to reach the detector.

The response will of course be proportional to the number of neutrons that undergo the influence of the bubble. The response will also be proportional to the chance of a neutron reaching the detector. (In the next section this probability will be described by the adjoint flux.)

2.2. *Moderation*

The bubble removes moderating material so that neutrons will have a smaller chance to become thermalized. If the neutron detector is one that detects mainly thermal neutrons (as most detectors do) the response will be negative. If however the detector is mainly sensitive to fast neutrons the response will be positive. The response will be proportional to the neutron flux and to the difference in detection probability for fast and thermal neutrons (as described by the difference of the fast and thermal adjoint flux in the next section).

2.3. *Diffusion*

This effect is somewhat more complex than the previous ones because it is determined by two opposing processes, depending on the travelling direction of the neutron. Neutrons travelling towards the detector will have an increased probability to be detected if scattering material is taken away, while neutrons moving away from the detector will have a smaller chance to be reflected towards the detector. The two processes act simultaneously, so the net effect will depend on the difference in the number of neutrons going in either direction, which is the component of the net neutron current vector in the direction of the detector. In the next section this directional dependence will be described by the inner product of the gradients of the flux and adjoint flux.

Summarizing: the total response of a neutron detector to a passing bubble is composed of three components:

—an always positive component due to decreased absorption;

—an always negative one due to decreased moderation, in the case of a thermal neutron detector and

—a geometry dependent component due to diffusion processes.

Clearly, the total response depends on the mutual proportion of the opposite processes and thus on the construction details of the specific reactor and the positions of bubble and detector therein.

Finally, it should be remarked that in the foregoing qualitative analysis only the influence of the bubble on neutrons going directly to the detector is considered. Changes in the production rate of neutrons and in information transferred by fission chains is neglected; in other words, reactivity effects are not considered. In fact only the local component of the response is thus evaluated.

For instance, with a thermal neutron detector the moderation component of the response would always be negative on the basis of the previous analysis; but in a reactor which is over-moderated, a positive reactivity effect occurs which will give rise to a positive "global" component in the response.

In the next section a more sophisticated model is developed in which the reactivity effects are (implicitly) considered.

3. COMPUTATION OF THE DETECTOR RESPONSE VIA PERTURBATION THEORY

The behaviour of the neutron population in a reactor is described by the Boltzmann equation:

$$\frac{\mathrm{d}}{\mathrm{d}t}\,\boldsymbol{\phi} = B\boldsymbol{\phi} + \mathbf{S}. \tag{1}$$

Here $\boldsymbol{\phi}$ is the state-vector of which the components are the energy and/or direction dependent (angular) neutron flux, delayed neutron precursor densities, etc.; $\mathbf{S}$ is the source vector and B is the transport operator.

Now we will consider cross section changes due to bubbles in the moderator, giving rise to changes in the neutron flux. We split the fluxes and the transport operator in a constant and a fluctuating part:

$$B = B_0 + \delta B$$

$$\boldsymbol{\phi} = \boldsymbol{\phi}_0 + \delta\boldsymbol{\phi}$$

and rewrite (1), neglecting second-order terms:

$$\frac{\mathrm{d}}{\mathrm{d}t}\,\delta\boldsymbol{\phi} = B_0\,\delta\boldsymbol{\phi} + \delta B\boldsymbol{\phi}_0 \tag{2.1}$$

$$B_0\boldsymbol{\phi}_0 = -\mathbf{S}_0 \tag{2.2}$$

Fourier-transforming (2.1) and eliminating the precur-

sor densities leads to

$$B(\omega)\delta\phi(\omega) = -\delta B(\omega)\phi_0, \tag{3}$$

where $B(\omega) = B_0(\omega) - i\omega E$, E being the unity matrix. In these equations the frequency-dependence of the variables is shown explicitly.

Now perturbation theory (Bell and Glasstone, 1970) is applied to compute the response of a neutron detector in the frequency domain. First, an adjoint operator $B^+(\omega)$ is constructed, operating on adjoint functions ϕ^+ which have the following property:

$$(\phi^+(\omega), B(\omega)\delta\phi(\omega)) = (\delta\phi(\omega), B^+(\omega)\phi^+(\omega)), \tag{4}$$

in which the inner product includes integration over space and energy variables.

For the construction of an operator B^+ which satisfies (4) we refer to van Dam (1977).

Adjoint functions are generated by the equation

$$B^+(\omega)\phi^+(\omega) + \Sigma_d = \mathbf{0}. \tag{5}$$

In this equation Σ_d is the macroscopic detection cross-section vector of the neutron detector under consideration, thus forming a kind of "adjoint source".

Combining (3)–(5), we finally get

$$(\Sigma_d, \delta\phi(\omega)) = (\phi^+(\omega), \delta B(\omega)\phi_0).$$

The LHS of this equation gives the fluctuation in the detector count rate which we define as the detector response:

$$R(\omega) = (\phi^+(\omega), \delta B(\omega)\phi_0). \tag{6}$$

Here the frequency dependence is shown. The adjoint flux $\phi^+(\omega)$ is frequency dependent because the adjoint operator B^+, which is related to $B(\omega)$, is frequency dependent.

If we restrict ourselves to a frequency region where $B(\omega)$ can be approximated as frequency-independent (e.g. the plateau region of the reactivity transfer function) then $B(\omega)$, B^+ and $\phi^+(\omega)$ are real and frequency-independent and (6) can then be inverse Fourier transformed into

$$R(t) = (\phi^+, \delta B(t)\phi_0) \tag{7}$$

which gives the detector response in time domain.

In fact, a "prompt response" approximation is applied here: the system relaxes infinitely fast to a stationary flux corresponding to the perturbed system and delayed effects do not play a role. In this frequency region the space dependence of the detector response to cross section changes, described by the adjoint flux and the stationary flux, is exact and no approximate methods (e.g. point model or quasi-static model (Kosaly *et al.*, 1977b)) are needed.

The above developed method is now applied to a two-group diffusion approximation with one group of delayed neutrons. The diffusion equations are:

$$\frac{\mathrm{d}}{\mathrm{d}t}\phi_1 = (\nabla D\nabla - \Sigma_{a_1} - \Sigma_{s_{12}} + \nu_1\Sigma_{f_1}(1-\beta))v_1\phi_1 + \nu_2\Sigma_{f_2}(1-\beta)v_1\phi_2 + v_1\lambda C + S_1v_1,$$

$$\frac{\mathrm{d}}{\mathrm{d}t}\phi_2 = \Sigma_{s_{12}}v_2\phi_1 + (\nabla D_2\nabla - \Sigma_{a_2})v_2\phi_2 + S_2v_2,$$

$$\frac{\mathrm{d}}{\mathrm{d}t}C = \beta\nu_1\Sigma_{f_1}\phi_1 + \beta\nu_2\Sigma_{f_2}\phi_2 - \lambda C.$$

Splitting the fluctuating quantities into a constant and a fluctuating part, Fourier transforming and eliminating the delayed neutron terms, we can write for $B(\omega)$:

$$B(\omega) = \begin{bmatrix} \nabla D_1v_1\nabla - \left(\Sigma_{a_1} + \Sigma_{s_{12}} + \dfrac{i\omega}{v_1}\right)v_1 + \nu_1\Sigma_{f_1}v_1\left(1 - \dfrac{\beta i\omega}{i\omega+\lambda}\right), & \nu_1\nu_2\Sigma_{f_2}\left(1 - \dfrac{\beta i\omega}{i\omega+\lambda}\right) \\ \Sigma_{s_{12}}v_2, & \nabla D_2v_2\nabla - \left(\Sigma_{a_2} + \dfrac{i\omega}{v_2}\right)v_2 \end{bmatrix}$$

Remembering that in multigroup diffusion theory the adjoint operator is the transpose of $B(\omega)$ and eliminating the frequency-dependence (plateau region) we get:

$$B^+ = \begin{bmatrix} \nabla D_1v_1\nabla - (\Sigma_{a_1} + \Sigma_{s_{12}})v_1 + \nu_1\Sigma_{f_1}v_1(1-\beta), & v_2\Sigma_{s_{12}} \\ v_1\nu_2\Sigma_{f_2}(1-\beta), & \nabla D_2v_2\nabla - \Sigma_{a_2}v_2 \end{bmatrix}.$$

The constant flux in the reactor is the solution of

$$\begin{bmatrix} \nabla D_1v_1\nabla - (\Sigma_{a_1} + \Sigma_{s_{12}}) + \nu_1\Sigma_{f_1}v_1, & v_2\Sigma_{f_2}v_1 \\ v_2\Sigma_{s_{12}}, & \nabla D_2v_2\nabla - \Sigma_{a_2}v_2 \end{bmatrix}\begin{bmatrix}\phi_1 \\ \phi_2\end{bmatrix} + \begin{bmatrix} v_1S_1 \\ v_2S_2 \end{bmatrix} = \mathbf{0}.$$

The bubbles cause fluctuations in D_1, D_2, Σ_{a_1}, Σ_{a_2} and $\Sigma_{s_{12}}$. The fluctuating part of the transport operator now reads

$$\delta B = \begin{bmatrix} \nabla\delta D_1 v_1 \nabla - v_1\delta\Sigma_{a_1} - v_1\delta\Sigma_{s_{12}}, & 0 \\ \delta\Sigma_{s_{12}} v_2 & , \quad \nabla\delta D_2 v_2 \nabla - \delta\Sigma_{a_2} v_2 \end{bmatrix},$$

where δD, etc. have a value at the position of the bubble and are zero elsewhere.

Using Green's divergence theorem, we can write for detector response:

$$R(\omega) = -\int \mathrm{d}V \{\delta D_1(\omega)\nabla\phi_1 \cdot \nabla\phi_1^+ + \delta D_2(\omega)\nabla\phi_2 \cdot \nabla\phi_2^+ + \delta\Sigma_{a_1}(\omega)\phi_1\phi_1^+ + \delta\Sigma_{a_2}(\omega)\phi_2\phi_2^+ + \delta\Sigma_{s_{12}}\phi_1(\phi_1^+ - \phi_2^+)\}, \quad (8)$$

the result given by van Dam (1976), or

$$R(t) = -\int \mathrm{d}V \{\delta D_1(t)\nabla\phi_1 \cdot \nabla\phi_1^+ + \ldots\} \quad (9)$$

using the prompt response approximation.

Because of the frequency independence we developed a useful tool for the computation of the response. The flux and adjoint flux can now be calculated once for every detector position (and every source position for subcritical systems) using any known technique. The method of computation for this work is discussed in the appendices. If the prompt response approximation is not applicable the adjoint flux should be computed for every frequency of interest separately, or, in the time domain, a space–time dependent reactor code should be used (Valko and Mesko, 1977). An example of the computed fluxes and adjoint fluxes is given in Fig. 3. Here the axial distribution is plotted for geometry 4*B* (see Section 4) for source strength of 1 n/s and a detector efficiency of 1 cps/unit flux.

4. EXPERIMENTAL SETUP AND EXPERIMENTS

Experiments were carried out in the light water moderated, natural uranium fuelled subcritical assembly LISA at Delft.

It consists of 253 fuel pins containing hollow uranium cylinders. These pins are placed in a hexagonal grid structure with a pitch of 45 mm, thus forming a core with a height of 82 cm and an equivalent diameter of 80 cm. The k_{eff} of the system is about 0.82 and the moderator–uranium volume ratio is 2.06. Some experiments were carried out in a modified core in which the fuel pins were re-assembled in another pattern (see Fig. 1). The M/F volume ratio in this core was 3.96, the core having a dia. of 92 cm and

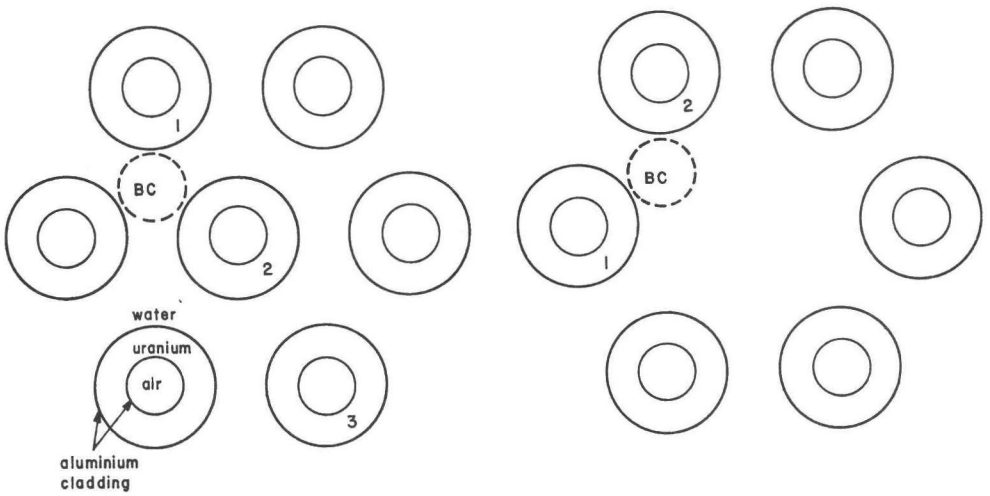

Fig. 1. Lattice cell configuration for the different geometries. Left figure: Normal fuel rod pattern. Detector in rod 1, neutron source in rod 3: configuration 1. Detector in rod 2, neutron source in rod 3: configuration 2. Detector in rod 3, neutron source in rod 2: configuration 3. Detector in rod 1, neutron source in rod 2: configuration 4. Right figure: Modified fuel rod pattern. Detector in rod 1, neutron source in rod 2: configuration 5. *BC* represents the bubble channel.

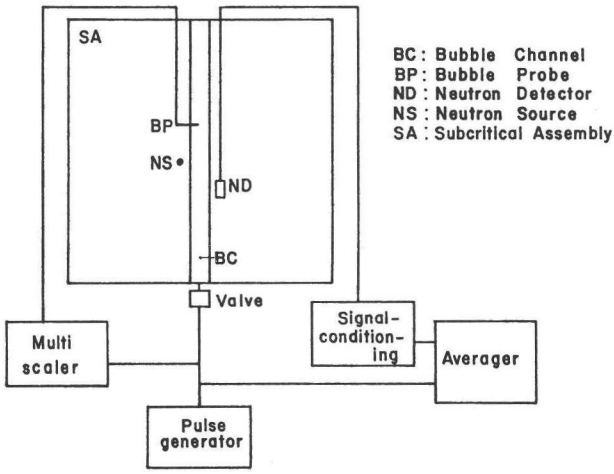

Fig. 2. Schematic survey of the experimental setup.

a k_{eff} of 0.85. A ^{252}Cf neutron source was placed in the centre of the core inside a fuel pin. A ^{3}He neutron detector (0.64 cm dia.) was placed inside another fuel pin. This detector was partly covered with cadmium, thus leaving a sensitive length of 2.5 cm.

Air bubbles were injected into the reactor in a bubble-channel positioned between the fuel pins. The bubbles were not generated continuously, but via a valve triggered by a pulse generator (pulse repetition time 10 s). At every pulse, the valve was opened and a bubble was generated which travelled upward in the system. The signal of the neutron detector was, after amplification, substraction of the mean level and anti-aliasing filtering fed into a 256-point digital signal averager. This averager was triggered by the same pulse that opened the valve. In this way an average-response technique for measuring the detector response was performed.

A bubble probe was positioned in the bubble channel, which detected the passing of a bubble through

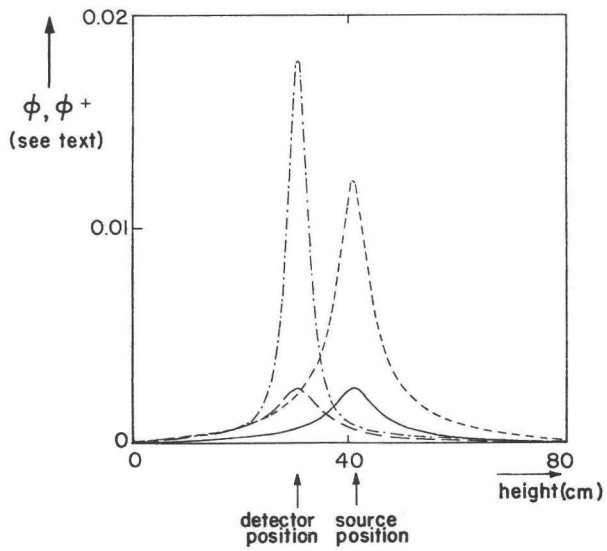

Fig. 3. Neutron flux and adjoint flux along the bubble channel in geometry 4*B*. ----- Fast flux. —— Thermal flux. ——— Fast adjoint flux. ——— Thermal adjoint flux.

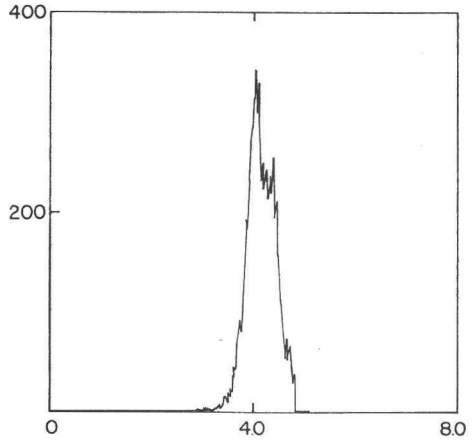

Fig. 4. Example of the bubble rise-time distribution. Horizontal axis: rise-time in seconds; vertical axis: counts per channel.

the channel. The signal of this probe was input to a multiscaler which was also triggered by the valve control pulse. In this way a bubble risetime distribution could be obtained (and from this a bubble velocity distribution) simultaneous to the response measurement. This bubble velocity appeared to be not very constant due to unknown circumstances, it could vary up to 20% r.m.s. during one experiment (see Fig. 4). The influence of this varying velocity will be discussed in Section 5. A schematic survey of the experimental setup is given in Fig. 2.

Measurements of the response have been carried out for several positions of the neutron detector and the neutron source around the bubble channel. This channel was always positioned at the centre of the core, the neutron source always at the middle of the core height at two different distances from the bubble channel.

All different combinations of the detector and source positions are coded by a number and a letter, the number applying to the geometry top view as displayed in Fig. 1, the letter to the height of the detector in the core: *A*: 41 cm (being mid-height); *B*: 31 cm; *C*: 21 cm; *D*: 36 cm and *E*: 33.5 cm.

5. RESULTS AND DISCUSSION

In this section both experimental and theoretical results are presented and compared.

The results are displayed in Figs 6–10. The responses are normalized to the computed and measured average count rate, respectively, to be independent of the exact value of source strength and detector efficiency. In the displayed curves no confidence intervals are given, but a good impression of the accuracy can be got from the spread of the measuring points in the figures.

To get a good understanding of the computed responses we compare these with the qualitative model, this being done with the aid of Fig. 5.

In this figure the five components of the detector response are drawn for four geometries: 1*B*, 2*B*, 3*B* and 4*B*. The five components are the contributions of fast and thermal absorption, fast and thermal diffusion and moderation, as they appear in (9). The curves in Fig. 5 are not normalized to the average count rate, but the values correspond to a unit source and detector strength. The qualitative model predicts for the absorption effect a positive contribution and for the moderation effect a negative one. This is in accordance with the computed results. The interesting difference between the pictures is the behaviour of the diffusion components, which should be dependent on the direction of neutron current relative to detector. When the bubble is far away at the top or bottom of the core, the net neutron current is directed outwards, away from the detector, and a negative (but small) contribution is expected. This is in effect the case.

When the bubble is closer to the detector, e.g. on the line detector–source, the response is positive if the bubble is in between detector and source and negative if the bubble is at the other side of either of them. Thus, a positive contribution is expected in 1*B* and 4*B*, and a negative one in 2*B* and 3*B*. This, too, is in accordance with Fig. 5 except for a small positive peak in the fast diffusion contribution in 3*B*. This can be explained by a closer look at the geometry: because the bubble is very near to the detector, and the source and detector are at 10 cm different height, there is a small region where the neutron current has a positive component in the direction of the detector. In this situation a small positive contribution should arise, as it does. In 2*B* the same effect occurs.

As a concluding remark it can be stated that the computed responses can be understood from the viewpoint of the elementary processes.

In Figs 6–10 the measured and computed responses are shown for comparison. However, direct comparison is not possible because the measured responses are influenced by bubble velocity variations (see Section 4). These velocity variations have a smoothing effect on the response, so that detail is lost. In principle this problem can be solved by "deconvoluting" the measured response with the measured bubble velocity distribution, but because of the statistical uncertainties in both this was practically impossible. Therefore the computed response was convoluted with the

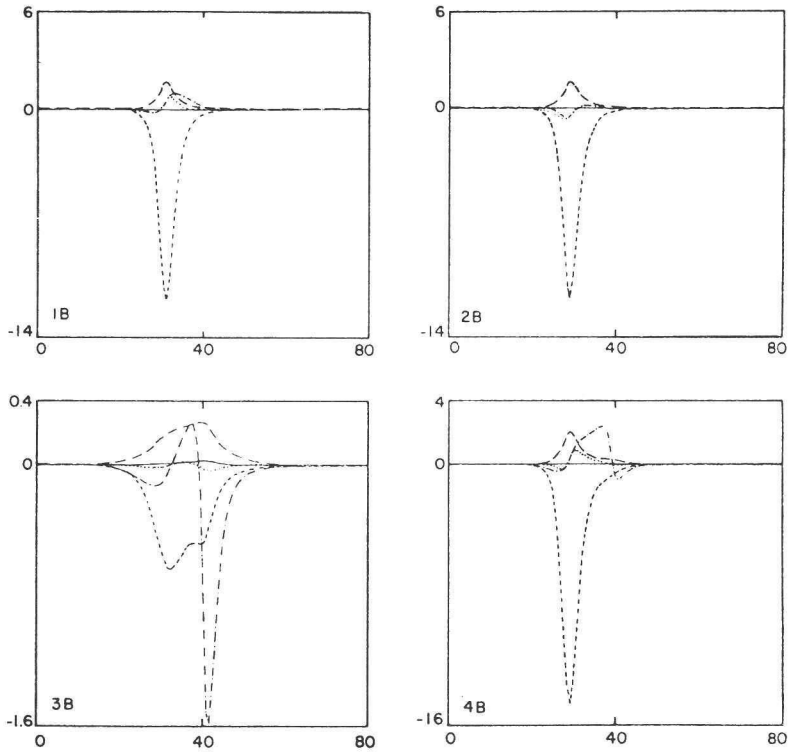

Fig. 5. The five components of the response as function of the bubble height for geometries 1*B*, 2*B*, 3*B* and 4*B*. —— Fast absorption. – – – – Thermal absorption. ----- Moderation. · · · · · · · · Fast diffusion. · · · · · Thermal diffusion. Horizontal axis: bubble position (cm); vertical axis: detector response in 10^{-7} counts/s.

measured velocity distribution, thus simulating the experiment, the results are also given in Figs 6–10. These figures consist of, from left to right, the plots:
—the computed response, for a bubble of 3.5 cm^3,
—this computed response convoluted with the velocity distribution and
—the measured response.

All curves are plotted against the axial position of the bubble in the channel. For the left curve this is obvious; for the centre and right curves, which are measured in time domain, this could be done using the average bubble velocity as obtained from the velocity distribution. In this way an easier comparison between experiments and theory is possible. A rather good correspondence between the calculated and the measured responses exists, apart from differences in the magnitude of the response of components thereof.

In all plots a major negative peak exists due to the moderation effect, and a smaller positive one in the situations where source and detector were not at the same axial position. This positive peak is partly due to the absorption effect and partly to the diffusion effect (cases 1*A*–*B*, 4*A*–*C*, 5*A*–*B*). In the cases 2 and 3 the diffusion effect should give a negative contribution, which agrees with the experiment.

In cases *A* only a negative peak is visible because all peaks coincide and the largest (moderation) dominates. Lowering the detector in the core leads to a shift and broadening of the diffusion peak; the moderation and diffusion peaks shift to different heights. This can be explained by the fact that, due to the different relaxation lengths of adjoint and regular flux, the moderation and absorption peaks will be near the detector, while the diffusion peak will have its maximum about where the bubble passes the line source–detector.

An interesting difference exists between geometries 1 and 2, where the moderation and absorption effects should be the same but the diffusion effect should change its sign. This indeed appears to be the case, especially in configuration *B*.

Another interesting difference exists between con-

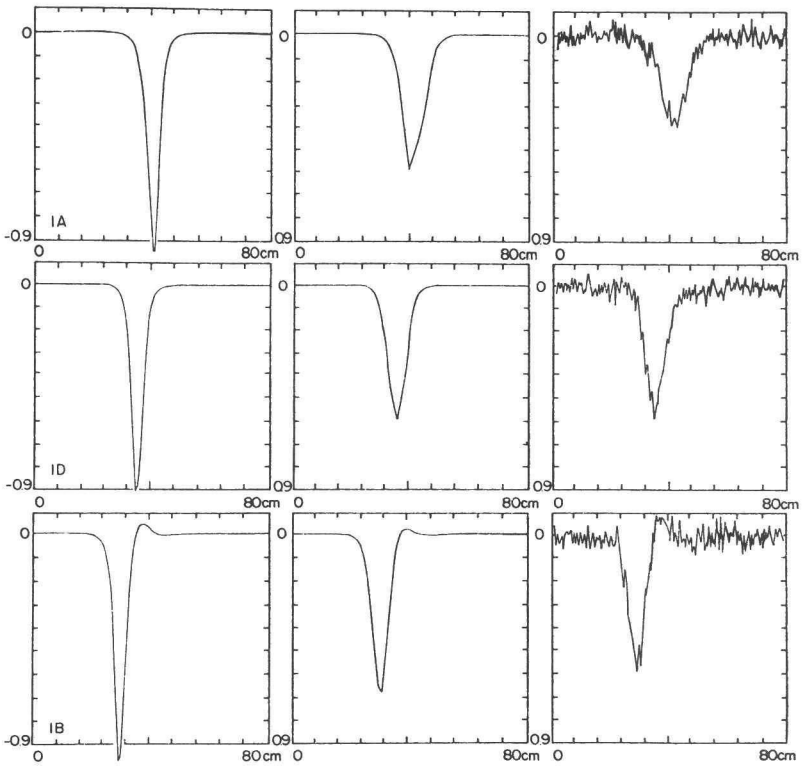

Fig. 6.

figurations 4 and 5. Here the detector and source are in the same positions but the M/F ratio is increased in configuration 5. This should lead to a reduction of the moderation effect because the difference between the fast and thermal adjoint fluxes decreases.

The question arises: Which effects cause the existing difference in magnitude between the computed and the measured responses? Some measurements agree well, while others are too large or have an incorrect ratio between the positive and negative peaks.

These differences may be explained by the following considerations.

The volume of the bubble was subject to slight variations, during a single measurement as well as between successive measurements. All calculations were done using a bubble volume of 3.5 cm^3.

In the calculation of the cross section set that was used for the computations some simplifying approximations are made that affect the cross sections. These have been calculated by the GGC-4 code which uses a homogenized reactor model with the same neutron energy spectrum for all the materials in all reactor zones. Spectral differences in the different materials would give a (slightly) different cross section set, especially in the thermal region.

The heterogeneities in the reactor also give rise to deviations of the flux that was computed for a homogeneous system. These heterogeneity effects have been accounted for in an approximate way and are commented on in Appendix 3.

The effect of the cadmium shield around the detector is neglected.

Perturbation theory itself might break down here, considering the large bubble dimensions. One would expect to have a smaller response then, and this tendency can be noticed in many of the pictures.

Considering the influence of the bubble velocity distribution on the response, uncertainties herein will also affect the correspondence between theory and experiment.

Now we will consider the experiment in connection with the local/global concept and in comparison with a similar experiment carried out in a critical facility (Fuge *et al.*, 1977; Valko and Mesko, 1977).

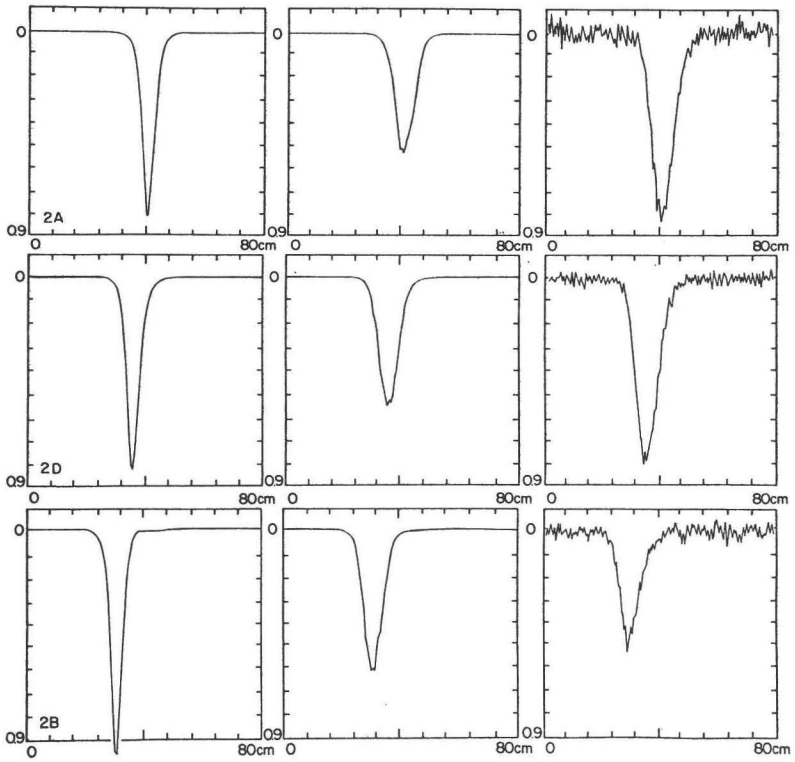

Fig. 7.

In the perturbation model the response is determined by the adjoint flux which can be characterized by two relaxation lengths in a two-group model. These relaxation lengths are, for a zero power reactor,

$$l_1 \approx L, l_2 \approx \sqrt{\tau G(\omega)}.$$

Here L is the thermal neutron diffusion length, τ the Fermi age and $G(\omega)$ the reactivity transfer function. l_1 and l_2 will be of the order of 1, respectively, 80 cm in the plateau region for a critical light water reactor. These distances can clearly be identified with a short-range or "local" sensitivity and with a long-range or "global" one.

In this experiment, however, the second relaxation length is about 6 cm, which certainly does not deserve the name "global". In this sense the responses computed here are local responses while a global effect does not occur. The global effect has also been identified as the reactivity component of the noise. In this experiment the reactivity effect of the bubble is negligible; it would give rise to relative responses of 10^{-6} only.

Summarizing, in the strongly subcritical system no global part of the response could be recognized in the experiments and in the theoretical treatment thereof. However, in a critical system the perturbation theory would give responses that can, partly, be considered as global.

The responses measured in this experiment show resemblance with an experiment described earlier (Fuge *et al.*, 1977; Valko and Mesko, 1977). There an average-response method was applied to a critical reactor and responses were obtained that showed similar behaviour, having positive and negative components. There are, however, important differences. Our responses are strictly local, but having a fine structure with negative moderation and sometimes positive diffusion components.

The responses in the critical system had a negative component which could be identified as global, and a local component that had a less pronounced structure. In our opinion this is mainly due to the fact that diffusion effects play a minor role because the flux gradients are much smaller in the critical system.

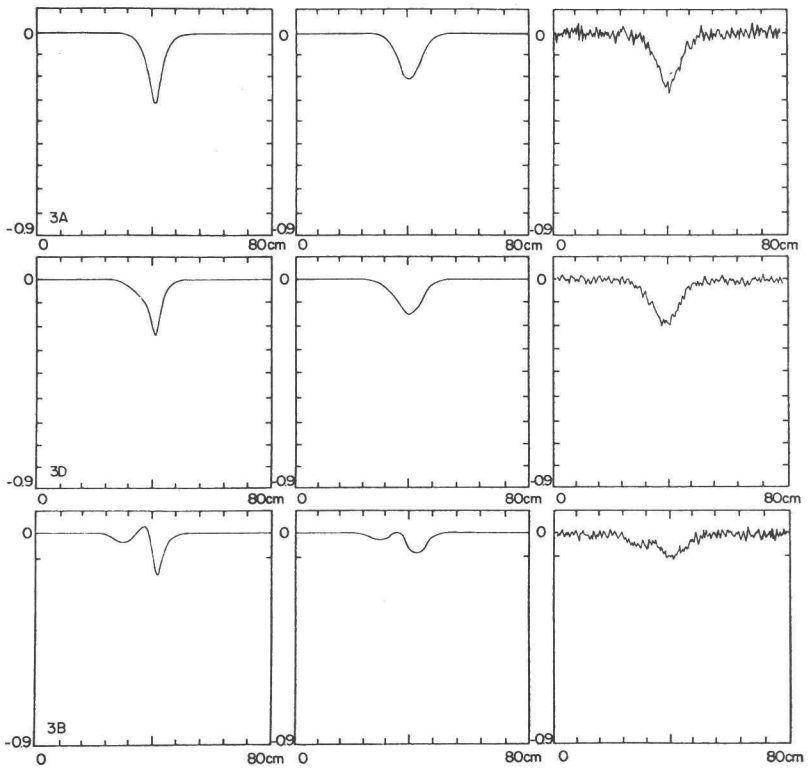

Fig. 8.

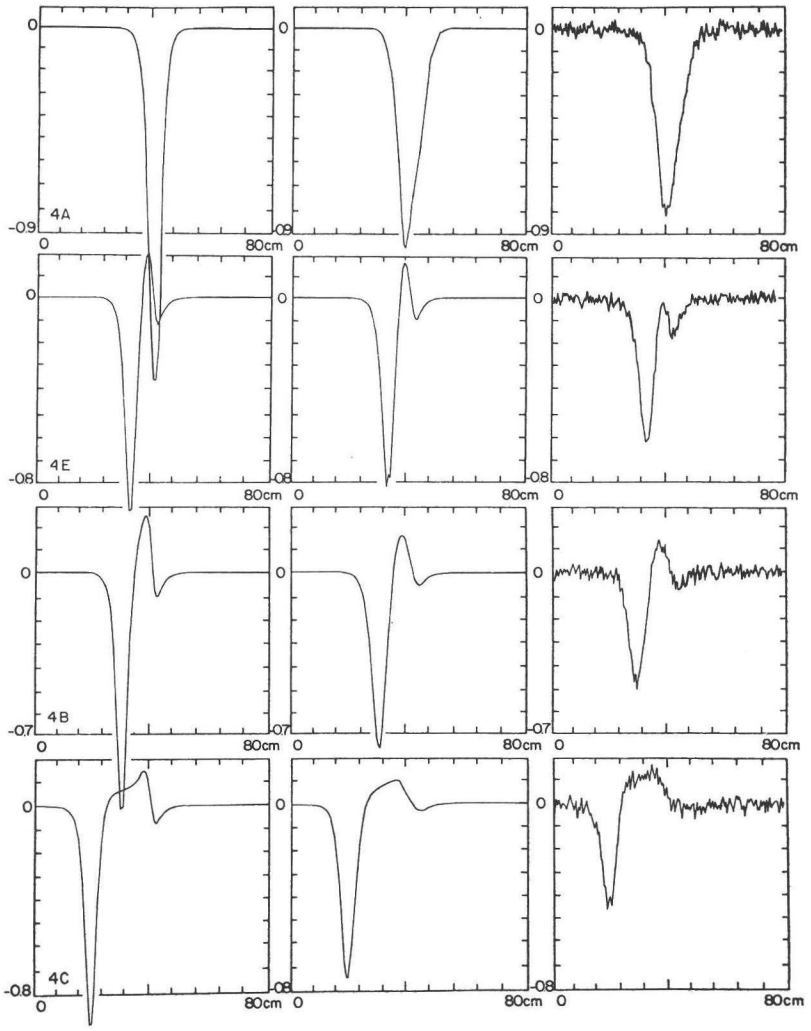

Fig. 9.

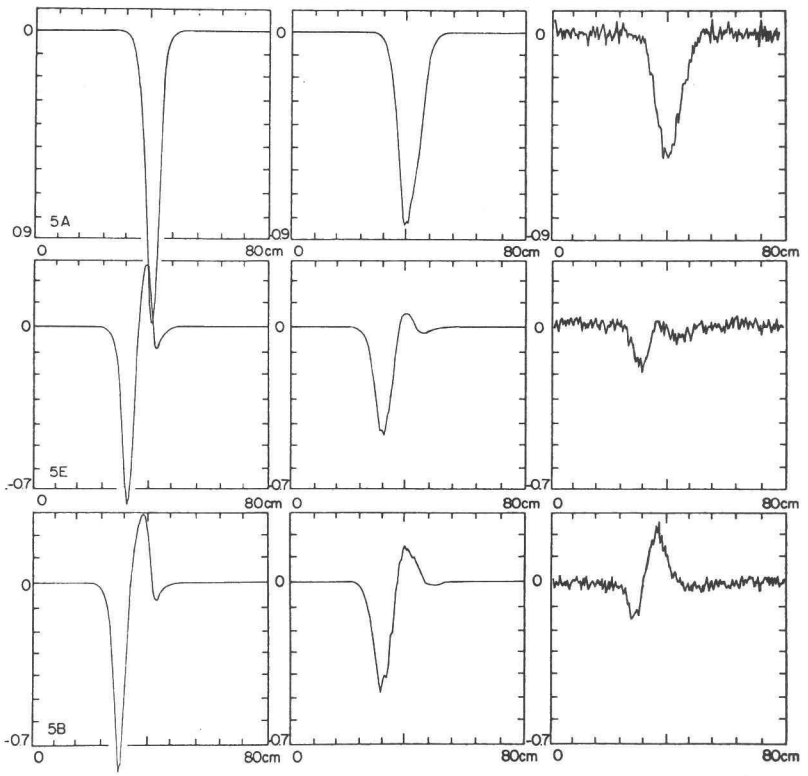

Fig. 10.

Figs 6–10. Computed and measured responses as function of the bubble height for configurations 1–5 for different detector heights. Horizontal axis: bubble position; vertical axis: response in % of average count rate.

The global behaviour of the response was clear from the response of an out-of-core detector.

However, the global component was slightly different for different detectors. This shows that the global component is not strictly the reactivity effect of the bubble. This space-dependence of the global component can be easily understood in the perturbation model: different detectors will have different adjoint fluxes and thus different responses.

6. CONCLUSIONS

The average response method is a good one for measuring the effect of air bubbles on the signal of a neutron detector in a (subcritical) reactor.

The perturbation model is well applicable to describe the above-mentioned experiment. Some differences between measurements and theory do exist but they are not considered as essential.

In the frequency region considered, the response of the system on the bubble can be considered as prompt. This facilitates the computation of the response, for no account has to be given to delayed (or "memory") effects.

The measured and computed responses can be considered as the "local" response in the local/global concept. Reactivity (or long range) "global" effects are negligible in the strongly subcritical system under consideration.

The responses can be understood from the viewpoint of a qualitative model.

REFERENCES

Adir J., Clark S., Froehlich R. and Todt C. J. (1967) Report *GA* 7157, San Diego.

Ashraf Atta M., Fry D. N., Mott J. E. and King W. T. (1978) *Nucl. Sci. Engng* **66**, 264.

Behringer K., Kosaly G. and Kostic Lj. (1976) Report *EIR-bericht* 303, Würenlingen.

Bell G. I. and Glasstone S. (1970) *Nuclear Reactor Theory*, Van Nostrand Reinhold, New York.
Ceelen D. von, Gebureck P. and Stegemann D. (1976) *Atomkernenergie* **27**, 239.
Crowe R. D., Eisenhawer S. W., McAfee F. D. and Albrecht R. W. (1977) *Prog. nucl. Energy* **1**, 85.
Dam H. van (1975) *Atomkernenergie* **25**, 70.
Dam H. van (1976) *Atomkernenergie* **27**, 8.
Dam H. van (1977) *Ann. nucl. Energy* **4**, 185.
Fowler T. B., Tobias M. L. and Vondy D. R. (1967) Report *ORNL*-4078, Oak Ridge.
Fuge R. (1975) Report *ZfK*-284, Rosendorf.
Fuge R., Valko J., Czibok T., Kätzmer D. and Vasilescu M. (1977) *Ann. nucl. Energy* **4**, 161.
Kosaly G., Maroti L. and Mesko L. (1973) *Ann. nucl. Energy* **2**, 315.
Kosaly G. (1975) Report *KFKI*-75-27, Budapest.
Kosaly G. and Mesko L. (1976) *Ann. nucl. Energy* **3**, 233.
Kosaly G., Kostic Lj., Miteff L., Varadi G. and Behringer K. (1977a) *Prog. nucl. Energy* **1**, 99.
Kosaly G., Mesko L. and Paszit I. (1977b) *Ann. nucl. Energy* **4**, 79.
Rhoades W. A. and Mynatt F. R. (1973) Report *ORNL-TM*-4280, Oak Ridge.
Schultz (1962) *Control of Nuclear reactors and power plants*, McGraw-Hill, New York.
Valko J. and Mesko L. (1977) *Prog. nucl. Energy* **1**, 205.
Wach D. and Kosaly G. (1974) *Atomkernenergie* **23**, 244.

APPENDIX 1

Calculation of the fluxes and adjoint fluxes

As stated in Section 3, the adjoint fluxes need only be computed once if the transport operator can be considered as frequency independent. It can be shown that the frequency dependence of the transport operator is related to the frequency dependence of the reactivity transfer function (van Dam, 1976; Behringer *et al.*, 1976). This transfer function is, for a far subcritical reactor, ($\rho_{\text{subcr}} \gg \beta$) constant up to frequencies of the prompt neutron decay constant α (Schultz, 1962).

In this reactor, $\rho_{\text{subcr}} \approx 0.21$, $\beta \approx 0.007$ and $\alpha = 4500\,\text{s}^{-1}$, so that the frequency independence is valid here.

The fluxes and adjoint fluxes have been computed with the aid of a numerical diffusion code. However, to reduce the complexity of the geometry, the simplifying approximation was made that the boundary effects in radial direction of the core are negligible in the region where source, detector and bubble channel are positioned. This implies that the (adjoint) fluxes are symmetrical around the source and the detector. Both flux and adjoint flux distributions (with respect to their sources) can be computed positioning the source and detector on the z-axis of the cylinder using a 2-dimensional R–Z geometry. Then, in a later stage, the response can be calculated with the computed flux distribution shifted to the actual position of detector and neutron source in the core.

The calculations were done for a homogenized reactor with the code EXTERMINATOR-II, a two-dimensional diffusion code (Fowler *et al.*, 1967). Cross sections were generated by the GGC-4 code (Adir *et al.*, 1967). The mesh covering the reactor had 128 equidistant points in the z-direction, thus giving the possibility to calculate the response for 128 points.

The convergence obtained was always better than 0.2%; tests, checking the influence of the convergence on the response, showed that this was acceptable. The adjoint fluxes were computed in the same way, using a thermal source representing the detector.

APPENDIX 2

A note on the perturbed cross section

A note must be made on the perturbed cross sections ($\delta\Sigma_a$, etc.) that are used in (9) to compute the response. Though the fluxes and adjoint fluxes are computed for a homogenized system, account must be taken of the inhomogeneities when considering the bubble; an air bubble in a homogeneous water–uranium mixture or a fuel suspension gives a quite different perturbation than a bubble in the pure water moderator between the fuel elements. Thus the perturbed cross sections must be related to the actual material in which they occur.

The magnitude of the changes is of course determined by the nuclear density changes in the moderator:

$$\Sigma_i = \sigma_i N,$$

where Σ_i and σ_i represent the macroscopic and microscopic cross sections, respectively, of the material for reaction type i, and N the nuclear density.

We assume σ not to change (no spectral changes) and find for the perturbed moderation and absorption cross sections $\delta\Sigma_i = \sigma_i \delta N$ and, when assuming vacuum in the bubble, $\delta\Sigma = -\Sigma$ because $\delta N = -N$.

For the diffusion component the situation is more complex. According to diffusion theory:

$$D = \frac{1}{3\Sigma_{\text{tr}}} = \frac{1}{3\sigma_{\text{tr}} N},$$

where Σ_{tr}, σ_{tr} are the neutron transport cross sections. This implies that for a bubble ($N \to 0$) D tends to infinity which leads to meaningless results. However, in the framework of a P_1 approximation to the transport equation (see Bell and Glasstone, 1978), the streaming term in the detector response reads:

$$-3\delta\Sigma_{\text{tr}} \mathbf{J}^+ \cdot \mathbf{J}_0,$$

where $\mathbf{J}^+$ and $\mathbf{J}_0$ denote the adjoint and unperturbed regular neutron current vectors, respectively, and are given by

$$\mathbf{J}_0 = -D\nabla\phi_0$$
$$\mathbf{J}^+ = D\nabla\phi^+.$$

This gives for the streaming term

$$\frac{\delta\Sigma_{\text{tr}}}{3\Sigma_{\text{tr}}^2} \nabla\phi_0 \cdot \nabla\phi^+.$$

Thus, for a bubble ($\delta\Sigma_{\text{tr}} = -\Sigma_{\text{tr}}$), the coefficient of this is equal to the diffusion coefficient in the unperturbed state: $\delta D = D$, which leads to the detector response:

$$R = \int -D\nabla\phi_0 \cdot \nabla\phi^+ \, \mathrm{d}V.$$

APPENDIX 3

Consideration of system heterogeneities

Since diffusion effects give an important contribution to the response, questions arise about the validity of the neg-

lect of the heterogeneous structure of the core, giving rise to flux gradients and flux variations around the fuel pins.

This problem can be handled as follows. The flux in the heterogeneous system will be described by

$$\phi_i(\mathbf{r}) = \phi_{i_H}(\mathbf{r})\{1 + \epsilon_i(\mathbf{r})\},$$

where ϕ_i is the real flux for group i, ϕ_{i_H} is the flux as computed from a homogenized core while ϵ_i is a shape function accounting for the microscopic flux distribution. ϵ_i can be estimated from lattice cell calculations if one assumes that the heterogeneities only affect the flux distribution in the radial direction.

Using this shape function, the effects of flux variations can be taken into account. The diffusion component changes as follows:

$$\delta R_D = -\int_{V_{\text{bubble}}} \delta D_i \nabla\phi_i \cdot \nabla\phi_i^+ \, dV.$$

where

$$\begin{aligned}\nabla\phi_i \cdot \nabla\phi_i^+ &= \nabla(\phi_{i_H}(1 + \epsilon_i)) \cdot \nabla(\phi_{i_H}^+(1 + \epsilon_i^+)) \\ &= (1 + \epsilon_i)(1 + \epsilon_i^+)\nabla\phi_{i_H} \cdot \nabla\phi_{i_H}^+ \\ &+ (1 + \epsilon_i^+)\nabla\phi_{i_H}^+ \cdot \nabla\epsilon_i + (1 + \epsilon_i)\nabla\phi_{i_H} \cdot \nabla\epsilon_i^+ \\ &+ \phi_{i_H}\phi_{i_H}^+ \nabla\epsilon_i \cdot \nabla\epsilon_i^+. \qquad \text{(A.1)}\end{aligned}$$

This expression must be integrated over the volume of the bubble.

If the bubble is symmetrically between the fuel elements (as is the case for geometries 1 to 4), the second and third term are zero, so that

$$\begin{aligned}\nabla\phi_i \nabla\phi_i^+ \approx (1 + \epsilon_i)(1 + \epsilon_i^+)\nabla\phi_{i_H} \cdot \nabla\phi_{i_H}^+ \\ + \phi_{i_H}\phi_{i_H}^+ \nabla\epsilon \cdot \nabla\epsilon_i^+.\end{aligned}$$

The $\nabla\epsilon_i \cdot \nabla\epsilon_i^+$ in the correction term is a constant that can be calculated from the lattice cell calculations.

For the absorption and moderation contributions, the same sort of corrections can be made. For the absorption, e.g.

$$\delta R_A = -\int dV \, \delta\Sigma_{a_i}\phi_i\phi_i^+,$$

where

$$\phi_i\phi_i^+ = \phi_{i_H}\phi_{i_H}^+(1 + \epsilon_i(1 + \epsilon_i^+).$$

The values of the (bubble volume averaged) ϵ's from cell calculations are:

$$\begin{aligned}\epsilon_1 &= -0.03, \\ \epsilon_2 &= 0.11, \\ \epsilon_1^+ &= 0.004, \\ \epsilon_2^+ &= -0.015, \\ \nabla\epsilon_1 \cdot \nabla\epsilon_1^+ &= -0.005 \text{ cm}^{-2}, \\ \nabla\epsilon_2 \cdot \nabla\epsilon_2^+ &= -0.016 \text{ cm}^{-2}.\end{aligned}$$

These cell calculations were performed using the code DOT-III. (Rhoades and Mynatt, 1973). Using these figures, one obtains corrections on the computed responses of the following magnitudes:

moderation	: reduction of 15%,
fast absorption	: reduction of 2.5%,
thermal absorption	: increase of 9%,
fast diffusion	: reduction of 2.5% and
thermal diffusion	: increase of 10%.

So the corrections do not have an extreme influence on the response.

The responses shown in Figs 6–9 have been corrected using the above mentioned method. For the geometry 5 (Fig. 10) the situation is more complex because the bubble is not in a symmetrical position in the lattice cell, so the second and third terms in (A.1) still play a role. Besides, cell calculations are more difficult to perform because of the far more complex geometry in the unit cell. For this case no corrections were made, but considering the magnitude of the corrections in the other cases, we feel that the computed results will not change drastically.

Acknowledgement—The authors wish to thank Mr J. C. Hamilton for his contribution in performing the measurements.

A TWIN SELF-POWERED NEUTRON DETECTOR FOR STEAM VELOCITY DETERMINATION IN A BOILING WATER REACTOR

E. B. J. KLEISS and H. VAN DAM *Interuniversity Reactor Institute*
Mekelweg 15, 2629 JB Delft, The Netherlands

Received July 9, 1980
Accepted for Publication November 25, 1980

A promptly responding self-powered detector was developed. It consists of two in-line mounted neutron sensitive elements, each containing one emitter of cadmium-magnesium alloy. It can be inserted into the core of an operating boiling water reactor to measure steam void velocity by cross correlating the two noise signals of the emitters. The short emitter length (2 cm) and distance (15 cm) provide sufficient coherence to determine void velocity and enable a good spatial resolution. The dc components of the signal currents appear to be affected by activation of the alumina insulator and a (possibly) thermal effect. From the noise measurements, the gamma sensitivity of the detector could be established.

I. INTRODUCTION

In recent years it has become a widespread field of research to measure void velocity and fraction in the fuel elements of boiling water reactors (BWRs) using the noise signals of in-core neutron detectors.[1-5] These noise signals are composed of a global part, due to reactor power fluctuations and a local part due to the steam bubbles generated in the fuel elements.[6-9]

This local component, which dominates in the frequency region above 1 or 2 Hz, carries information on the flow conditions in the fuel elements, from which, e.g., the steam velocity can be estimated. The information thus gathered is interesting when compared with the results of thermohydraulic calculations that are performed for plant operation. The measurements could be a check on the validity of the thermohydraulic models or parameters that are applied. On the other hand, good calculations could give an answer to the still existing question concerning the nature of the measured velocities (e.g., Ref. 4). In any case there is a need for velocity measurements for which the neutron noise signals are well suited. Neutron detectors commonly used for this purpose are often the ones available from standard reactor instrumentation, i.e., the fixed local power range monitor detectors and the movable traversing in-core probe (TIP) detectors with which most modern BWRs are extensively equipped. With this detector system the desired measurements can be performed at several radial and axial core positions, depending on the available detectors. Sometimes, however, measurements are desired with a better spatial resolution or at other positions than can be done using the existing detectors. This was one of the reasons to develop a twin neutron detector (being a string of two axially separated neutron sensitive elements) that can be inserted into the core using the existing TIP tubing systems. The detector can be positioned in any core position that can be reached with the TIP system at any desired height. The signals of the two elements can be correlated to measure local void velocity. The detector is of the self-powered type with a prompt response to neutron flux changes. Such detectors are widely used as in-core instruments and have shown a good performance.[10] A self-powered detector concept was chosen because this detector type is relatively simple and cheap to fabricate while robust constructions are possible. A detector was assembled and positioned in one of the TIP systems of the Dodewaard BWR [54 MW(electric), The Netherlands]. The design is discussed in Sec. II and some experiments that were carried out to test detector performance are described in Sec. III.

II. CONSTRUCTION

In order to determine steam transit times by cross correlation, two neutron detectors have to be inserted in the same TIP channel simultaneously. This can be realized by mounting the two detectors in line to a common signal/drive cable (Fig. 1). In this way the assembly can pass through the existing TIP tubing system into the core. The points that have to be considered when constructing the detector are the dimensions and the choice of applied materials.

II.A. Dimensions

The outer dimensions are limited by external factors. The detector has to pass through rather narrow and winding tubes. The maximum length of any rigid part that can pass there is ~10 cm. The desired distance between the two elements is longer, so it is clear that a detector cannot be made in one rigid housing. Therefore, two separate elements, each containing one neutron detector and small enough to pass through the system, are used. They are connected via a fairly flexible cable that is also the signal cable of the upper detector. The two elements have a 5-cm length and 5-mm o.d. Each element contains an emitter, insulated from the sheath by an alumina tube. The sheath functions as the collector of the so-formed self-powered neutron detector (SPND). The diameter of the emitters is 3 mm, which is the maximum possible; the length is chosen to be 2 cm, which is a compromise between two conflicting requirements. On one hand, the sensitivity of the detector is proportional to the emitter length, thus it should be as long as possible from the point of view of signal-to-noise ratio. On the other hand, we are interested in measuring the local flux changes due to steam bubbles so the sensitive length (field of view) over which the flux variations are measured should be as short as possible. Due to the diffusion process of neutrons in the reactor core, this sensitive length is on the order of emitter length plus thermal neutron diffusion length L (Refs. 8 and 9). Consequently, it is of no use making the emitters much shorter than L. A choice of 2 cm, being on the order of L, is considered a reasonable compromise.

The last dimension to be established is the distance between the two emitters. One has a rather large freedom to choose this parameter, as long as this distance is known accurately. This choice, however, is influenced by some conflicting considerations. As emitter distance increases, the coherence of the signals decreases due to the perturbation of void distribution (by boiling and turbulences) during the transit from lower to upper detector. This results in a smaller (absolute) statistical precision of the measured transit time. However, the transit time increases and the relative precision of the obtained transit time (thus of the velocity) increases if the coherence does not decrease too much. An optimal choice of the emitter distance is only possible after detailed knowledge of coherence-distance relations.

Furthermore, a systematic error in the computed velocity occurs when the velocity changes over measuring height,[11] as is the case in a BWR. This error is decreased when the emitter distance is chosen small enough. In this case also an improved spatial resolution of the measured velocity profile is possible. The detector was designed with an emitter distance of 150 mm; after assembling, a Röntgen picture showed it to be 151 mm.

II.B. Materials

The choice of the emitter material is governed by two aspects. First, the self-powered detector should have a fast response to neutron flux changes due to the high frequency nature of the bubble noise studied (up to 50 Hz). Therefore, a promptly responding type of SPND is required in which current is produced by Compton scattering of neutron-capture gamma rays. Secondly, because of the rather small emitter dimensions and the desired sensitivity (for noise measurements!), a strong neutron absorber is needed. Cadmium was considered as a good material, except for the low melting point (320°C). An alloy of cadmium and magnesium (60 wt% Cd–40 wt% Mg) with a melting point of ~500°C (Ref. 12) was applied instead of pure cadmium.

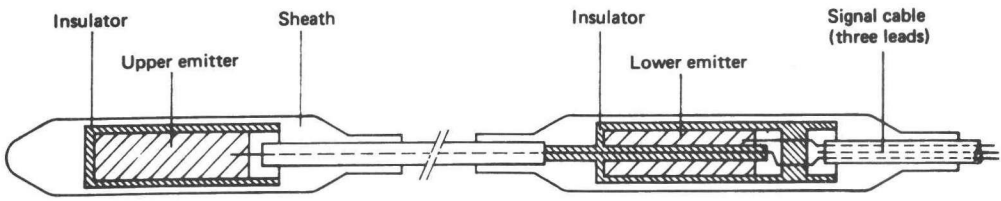

Fig. 1. Sketch of the TSPND.

The burnout rate of the emitter is ~2% per month. This is not considered as a handicap, because the detector is intended to be used only incidentally and is not left in the core permanently.

The insulators that separate the emitters from the sheath are Al_2O_3 tubes, the detector sheath is stainless steel. All cables used are Al_2O_3 insulated thermocoax cable with Inconel cladding.

The detector string is mounted to a three-lead cable. Two leads are connected to the two emitters; the third lead functions as a compensation for radiation-induced signals in the cable. The signal cable is surrounded by a spiralized drive cable to move the detector in and out the core. Figure 1 is a drawing of the twin self-powered neutron detector (TSPND). Note that the lower emitter is hollow to let the signal wire of the upper emitter pass through.

III. EXPERIMENTS

To test the performance of the detector, an experiment was carried out in which the detector was stepwisely inserted into the core and left at each position for ~6 min. The three signals (two emitters plus compensation) were amplified by low-noise preamplifiers and the compensation signal was subtracted from the emitter signals. The signals were recorded in two ways: on one track of the recorder directly to preserve the dc components and on another track after high-pass filtering (0.1 Hz) and further amplification to obtain the noise component.

The dc components of (compensated) emitter currents and compensation currents are given in Fig. 2 as a function of time. A positive signal is generated by the two emitters due to the electrons scattered from the emitter to the sheath. The lower emitter appears to have a larger sensitivity. (We will discuss this effect later.) The compensation current is negative; apparently the main current component is the one due to electrons scattered from sheath to lead. This current decreases (becomes more negative) when the detector is inserted further into the core, due to the greater length of irradiated cable. Also a positive component that settles exponentially is observed. This effect is most clear when at the end of the experiment the detector is removed from the core; only the positive, decaying component remains. Its half-life was found to be 2.25 ± 0.05 min, which proves it to be caused by the activation of the aluminum in the insulator, that decays (2.3 min half-life) by β^- emission and produces a current as in the delayed-response type self-powered detector. This alumina effect accounts for about −40% of the compensation current. It can also be noticed in the emitter signals but here it amounts to only a few percent. The signal of the lower emitter is constant

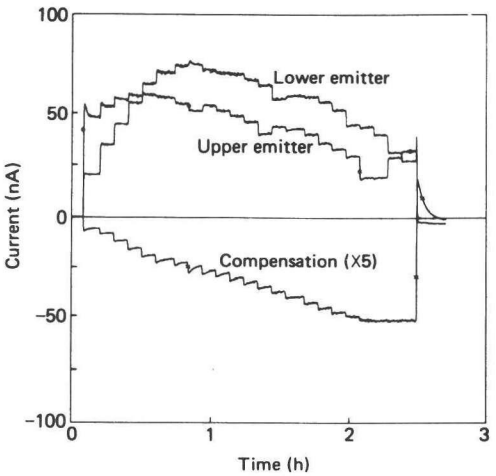

Fig. 2. The dc signals of upper and lower emitter and compensation during a stepwise insertion of the TSPND in the core.

in each interval (apart from reactor power fluctuations that cause the noise on the signal); that of the upper emitter has a decaying component after insertion into the core. The half-life of this effect is ~1.5 min, which does not correspond to the decay of activation products of any applied material. It might be caused by thermal effects; thermal effects on SPDs have been reported elsewhere.[13] The dc signals of the emitters as a function of their axial position in the core are given in Fig. 3. Here also is given a flux map obtained with a movable fission chamber (TIP). Comparison shows that the signals are in accordance with this flux map.

The gamma sensitivity of the detector is also an interesting parameter, because it reduces the usefulness of the detector for flux mapping. In principle, all promptly responding SPNDs are more or less gamma sensitive because they produce current by Compton scattering of gamma rays. This gamma sensitivity could not be obtained from the dc measurements, because the gamma flux distribution in the core was not known, but it can be estimated from the noise analysis results described hereafter.

The mentioned effects (gamma sensitivity, alumina activation, and thermal effect) reduce the suitability of the detector for flux mapping. They also influence the dynamic characteristics of the detector. However, thanks to the rather low frequency nature of these effects they do not influence the purpose of the TSPND: velocity measurement

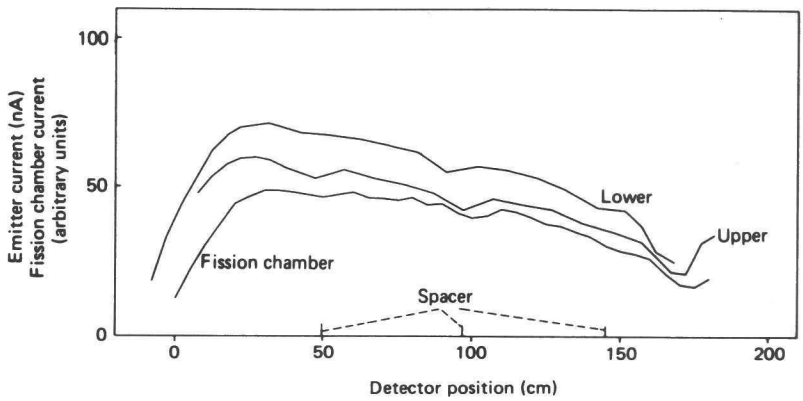

Fig. 3. The dc signals of upper and lower emitter and a fission chamber as function of axial detector position.

by cross correlating noise signals, where higher frequencies play a role.[1,2,6,7,11]

The noise signals were recorded and off-line analyzed on a minicomputer based Fourier analysis system. The auto and cross spectra of the emitter signals were obtained for every detector position. Figure 4 is an example of such analysis for an average emitter position of 67 cm above the bottom of the core. (Effective fuel length of the Dodewaard reactor is 180 cm.) Here the (normalized) auto power spectral densities (NAPSDs) of the two emitter signals are given, and their NCPSD, phase, and coherence. The coherence is sufficiently high to determine the phase curve slope for frequencies up to 20 Hz and to calculate the transit time. This is done using an iterative least-squares fit of the phase curve to a straight line. The frequency interval used for the fit is from 4 Hz to 4 Hz + $1/\tau$, where τ is the transit time from the previous iteration. In this way the effect of phase oscillations due to the global background[6,7] is reduced. Above 4 Hz, the signals are dominated by the local bubble noise. The coherence is used as a weight factor for the fit. Statistical precision of the obtained transit times is always better than 4% when 5 min of signal are analyzed.

Figure 5 gives a velocity profile as measured with the TSPND. A rather high spatial resolution is possible because of the small emitter distance and the possibility to position the detector at any desired height. For instance, the effect of the three spacers in the fuel elements on the flow can be noticed (the effect is also visible in the flux map of Fig. 3). In this paper, we do not go further into the evaluation of these results.

A special phenomenon to be noticed in Fig. 4 is that, in the frequency region where local noise

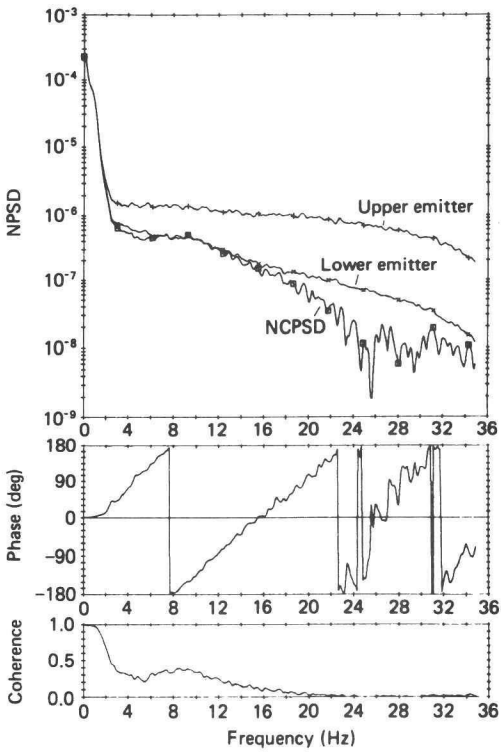

Fig. 4. The NAPSD of upper and lower emitter signals and their NCPSD, phase, and coherence.

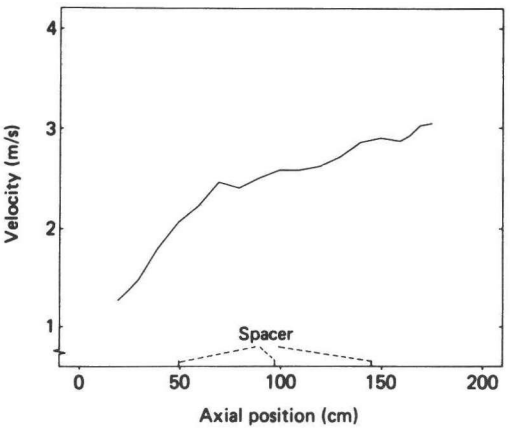

Fig. 5. Axial steam velocity distribution measured with the TSPND.

dominates, the NAPSD of the upper emitter is considerably larger than that of the lower one. Furthermore, comparison with the NAPSD of a fixed fission chamber at a height of 98 cm shows that the NAPSDs of the two emitters (when in a comparable core position) are larger. This effect can be explained by the gamma sensitivity of the TSPND. In the low frequency region, neutron flux and the larger part of the gamma flux fluctuate with reactor power, so the NAPSDs of different detectors are nearly equal, regardless of their sensitivity. In the high frequency region, however, noise is caused by local fluctuations of voids with a larger influence of the neutron flux than on the gamma flux. Because the NAPSD is obtained by division by the dc signal, the component due to gamma radiation influences the NAPSD. In formula, assuming no local gamma flux noise:

$$\text{NAPSD} = \frac{\sigma^2 \epsilon_n^2}{(i_n + i_\gamma)^2} ,$$

where

σ^2 = APSD of neutron flux noise

ϵ_n = neutron sensitivity of the detector

i_n and i_γ = neutron- and gamma-induced dc currents, respectively.

With $i_n = \epsilon_n \phi_0$ (ϕ_0 denoting the neutron flux) and because σ^2 is proportional to ϕ_0^2 (Refs. 7 and 9) according to

$$\sigma^2 = \sigma_0^2 \phi_0^2 ,$$

it follows that

$$\text{NAPSD} = \frac{\sigma_0^2 i_n^2}{(i_n + i_\gamma)^2} = \frac{\sigma_0^2}{\left(1 + \frac{i_\gamma}{i_n}\right)^2} .$$

For two detectors under comparable flow conditions, σ_0^2 is the same, so

$$\frac{[\text{NAPSD}]_{\text{det 1}}}{[\text{NAPSD}]_{\text{det 2}}} = \frac{\left[\left(1 + \frac{i_\gamma}{i_n}\right)^2\right]_{\text{det 2}}}{\left[\left(1 + \frac{i_\gamma}{i_n}\right)^2\right]_{\text{det 1}}} .$$

Assuming that for the fission chamber i_γ / i_n is much smaller than for the TSPND, we can compute the current components for emitter heights of 98 cm (measured from core bottom) using the NAPSD values at, for instance, 5 Hz. Results are given in Table I. Accuracy in the current components is ~5 nA. As seen from this table, the neutron-induced currents are about the same for the two emitters. The difference is mainly due to the different gamma currents. This gamma current is negative, which means that it is mainly caused by electrons scattered into the emitter. This has been reported earlier for cobalt SPNDs (Ref. 14). Assuming a typical gamma flux of 300 MR/h in the core, the sensitivity of the lower emitter is -3×10^{-17} A/(Rh^{-1}). This is in accordance with an experiment carried out with the detector in a ^{60}Co irradiation facility. When the detector was positioned in a flux of ~0.16 MR/h, a current of -15 ± 2 pA was measured, which is on the order of magnitude expected. The difference between the gamma currents of upper and lower emitter might be explained by the 15 cm (uncompensated) cable between the two emitters, in which a current is also generated. Kroon et al.[10] give measured sensitivities for Al_2O_3 insulated cable 1.57 mm in diameter for neutrons and ^{60}Co gamma rays. Using a neutron flux of 2×10^{13} n/cm^2·s and a gamma flux of 300 MR/h, which are typical values for this reactor, the 1.57-mm cable would produce 0.3 nA due to neutrons and −3.5 nA due to gamma rays. Considering the

TABLE I

Signal Components of the TSPND as Calculated from the NAPSDs

Detector Type	NAPSD at 5 Hz	i (nA)	i_n (nA)	i_γ (nA)
Fission chamber	0.92×10^{-6}	---	100%	---
Upper emitter	2.5×10^{-6}	42	69	-27
Lower emitter	1.25×10^{-6}	56	66	-10

different diameters, the uncertainty in the fluxes and in the measured currents, it cannot be proved that the cable causes the sensitivity difference, but indications are strong.

One more interesting signal to analyze is the compensation current. Figure 6 gives the spectra, phase, and coherence of this signal and that of an ex-core neutron detector. The TSPND was moved to the top of the core, so that the compensation cable was integrating flux fluctuations over nearly total core height. It appears that the two signals resemble each other quite strongly; no phase differences and a good coherence are found. The resemblance indicates that the compensation current can be used quite well as a measure for average fuel bundle power fluctuations. For frequencies above 5 Hz, background noise (from amplifier, recorder, etc.) dominates the compensation current. At low frequencies, the NAPSDs deviate due to misnormalization caused by the effects of ^{28}Al decay and constant gamma background in the core; these effects, however, partially cancel each other out because of their opposite contributions to the signal.

Because the spectrum of the compensation current decreases rather strongly with increasing frequency, compared with that of the emitters, it does not contribute significantly to the signal of the emitters in the higher (>4-Hz) frequency region, although the dc component can amount to more than 50% of emitter current (Fig. 2). The main advantage of the compensation wire is that it considerably reduces the 50-Hz hum picked up in the cable.

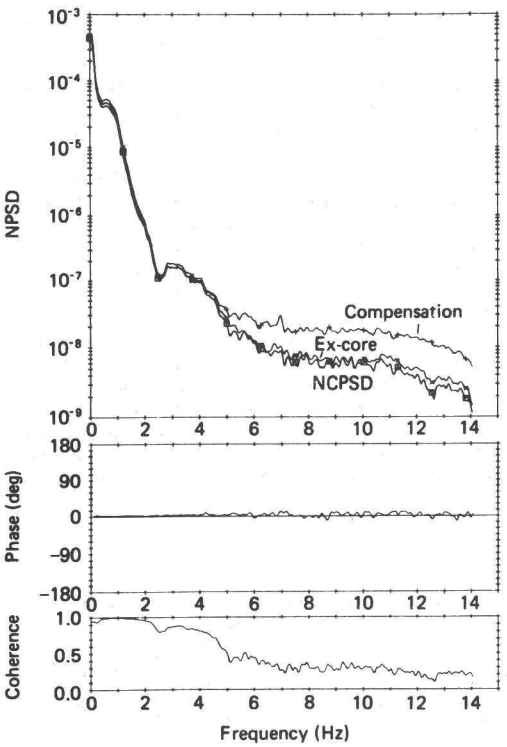

Fig. 6. The NAPSD of compensation signal and ex-core detector signal and their NCPSD, phase, and coherence.

IV. CONCLUSIONS

The TSPND proved useful for steam velocity measurements in a BWR. The signals produced were large enough to enable noise analysis. The dc and low frequency components of the emitter signals are influenced by several effects: reactor gamma background, aluminum activation, and a possible thermal effect. These effects reduce the usefulness of the detector for flux mapping. Because of their low-frequency nature, they do not influence the cross correlation process performed to measure steam transit times. These could be determined quite accurately, within short time intervals. The advantage of the TSPND over fixed in-core detectors is also that measurements can be done at any desired height, and due to the rather small distance of the emitters a good spatial resolution is possible.

REFERENCES

1. M. ASHRAF ATTA, D. N. FRY, J. E. MOTT, and W. T. KING, "Determination of Void Fraction Profile in a Boiling Water Reactor Channel Using Neutron Noise Analysis," *Nucl. Sci. Eng.*, **66**, 264 (1978).

2. D. VON CEELEN, P. GEBURECK, and D. STEGEMANN, "Bestimmung der Dampfblasengeschwindigkeit und des Dampfgehalts in SWR Brennelementen mit statistischen Analyseverfahren," *Atomkernenergie*, **27**, 239 (1976).

3. W. SEIFRITZ and F. CIOLI, "On-Load Monitoring of Local Steam Velocity in BWR Cores by Neutron Noise Analysis," *Trans. Am. Nucl. Soc.*, **17**, 451 (1973).

4. G. KOSALY, "Noise Investigations in Boiling Water and Pressurized Water Reactors," KFKI-1979-57, Magyar Tudomanyos Akademia Kozponti Fizikai Kutato Intezete, Budapest (1979).

5. J. A. THIE, "Core Motion Monitoring," *Nucl. Technol.*, **45**, 5 (1979).

6. D. WACH and G. KOSALY, "Investigation of the Joint Effect of Local and Global Driving Sources in In-Core Neutron Noise Measurements," *Atomkernenergie*, **23**, 244 (1974).

7. H. VAN DAM, "Neutron Noise in Boiling Water Reactors," *Atomkernenergie*, **27**, 8 (1976).

8. G. KOSALY and L. MESKO, "Theory of the Auto-Spectrum of the Local Component of Power Reactor Noise," *Ann. Nucl. Energy*, **3**, 233 (1976).

9. E. KLEISS and H. VAN DAM, "Analysis of Neutron Detector Response to Bubbles in a Water Moderated Reactor," *Ann. Nucl. Energy*, **6**, 385 (1979).

10. J. C. KROON, F. M. SMITH, and R. I. TAYLOR, "Self-Powered Flux Detectors: Status and Prospects," *Trans. Am. Nucl. Soc.*, **23**, 459 (1976).

11. G. KOSALY, Lj. KOSTIC, L. MITEFF, G. VARADI, and K. BEHRINGER, "Investigation of the Local Component of the Neutron Noise in a BWR and Its Application to the Study of Two-Phase Flow," *Prog. Nucl. Energy*, **1**, 99 (1977).

12. M. HANSEN, *Constitution of Binary Alloys*, McGraw-Hill Book Company (1958).

13. H. BÖCK, "Incore Neutron Detector Behaviour During Reactor Transient Operation," *Nucl. Instrum. Methods*, **125**, 327 (1975).

14. R. B. SHIELDS, "A Platinum Incore Flux Detector," *IEEE Trans. Nucl. Sci.*, **20**, 603 (1973).

Annals of Nuclear Energy, Vol. 8, pp. 205 to 214, 1981
Printed in Great Britain

0306-6549/81/050205-10$02.00/0
Pergamon Press Ltd

INCORE POWER FEEDBACK EFFECTS DEDUCED FROM NEUTRON NOISE MEASUREMENTS

E. B. J. KLEISS and H. VAN DAM
Interuniversity Reactor Institute, Mekelweg 15, 2629 JB Delft, The Netherlands

(*Received* 28 *November* 1980)

Abstract—Reactor noise measurements were performed in a BWR using incore neutron detectors at different radial core positions. Some systematic space dependent effects on the coherence of the detector signals were observed in the low frequency region. These can be explained by an uncorrelated distributed noise source working on detectors with a frequency dependent field of view due to power feedback effects. The measurements can be used to estimate the at-power reactivity transfer function of the reactor.

1. INTRODUCTION

In the study of the noise signals of incore neutron detectors in BWRs, much attention has been paid to the relations between the signals of axially separated detectors, at the same radial core position. This is motivated by the possibility to measure interesting parameters as void velocity in this way. Experiments and theoretical work (see Kosaly, 1979 for a review) have shown that the incore neutron noise field can be described as being composed of a local component due to the steam void formation and transport in the core and a global component attributed to reactivity fluctuations. The white local noise dominates in the higher frequency region of the spectrum (above 1 or 2 Hz) and enables the determination of void velocity by the slope of the phase curve. The global noise dominates in the lower frequency region. Because of the reactivity type of this noise it influences all neutron detectors in the same way and leads to a high coherence and zero phase shift of the signals. As an example, Fig. 1 gives the spectra, phase and coherence of the signals of two incore neutron detectors at 15 cm distance in the core of the Dodewaard Reactor (Netherlands), as measured with a twin detector. This is a string of two neutron detectors that can be inserted in the reactor core to measure void velocity (Kleiss and van Dam, 1981). All characteristics of the local and global noise field are clearly demonstrated in this figure.

However, the picture changes if one does not consider axially separated detectors but incore detectors at different radial positions. Firstly, the local noise is not any more correlated so the coherence in the high frequency region is drastically reduced. But also for low frequencies a systematic decrease in coherence can be noticed. Figure 2a gives the coherence of the three combinations of three incore detectors located at the same axial position (98 cm above the bottom of the fuel, that has an effective length of 180 cm) at different radial positions. The detector positions in the core are shown in Fig. 2b. From Fig. 2a two systematic phenomena can be observed in the coherence:

(1) for a specific frequency, the coherence decreases as the detector distance increases;
(2) for every detector combination, the coherence is dependent on frequency, i.e. it decreases with decreasing frequency (except for a peak at about 0.02 Hz).

This phenomenon is quite unexpected and not in line with the assumed global character of the low frequency noise. Similar behaviour for the Browns Ferry reactor has been reported earlier by Sides *et al.* (1977). It is an indication that this noise is not sufficiently described with a reactivity perturbation and point reactor kinetics, even in such a small core as that of the Dodewaard reactor. The validity of the point reactor model and the description of the global noise component has already been the subject of some research (Kosaly, 1979; van Dam, 1976; Behringer *et al.*, 1977) for the zero-power case. We will adopt their method (extended to the at-power case) and use it to explain the observed effects, in the next section. This will also allow us to extract useful information from the observations.

2. THEORETICAL BACKGROUND

In the approach of van Dam (1976) and Behringer *et al.* (1977) the detector noise signal is caused by

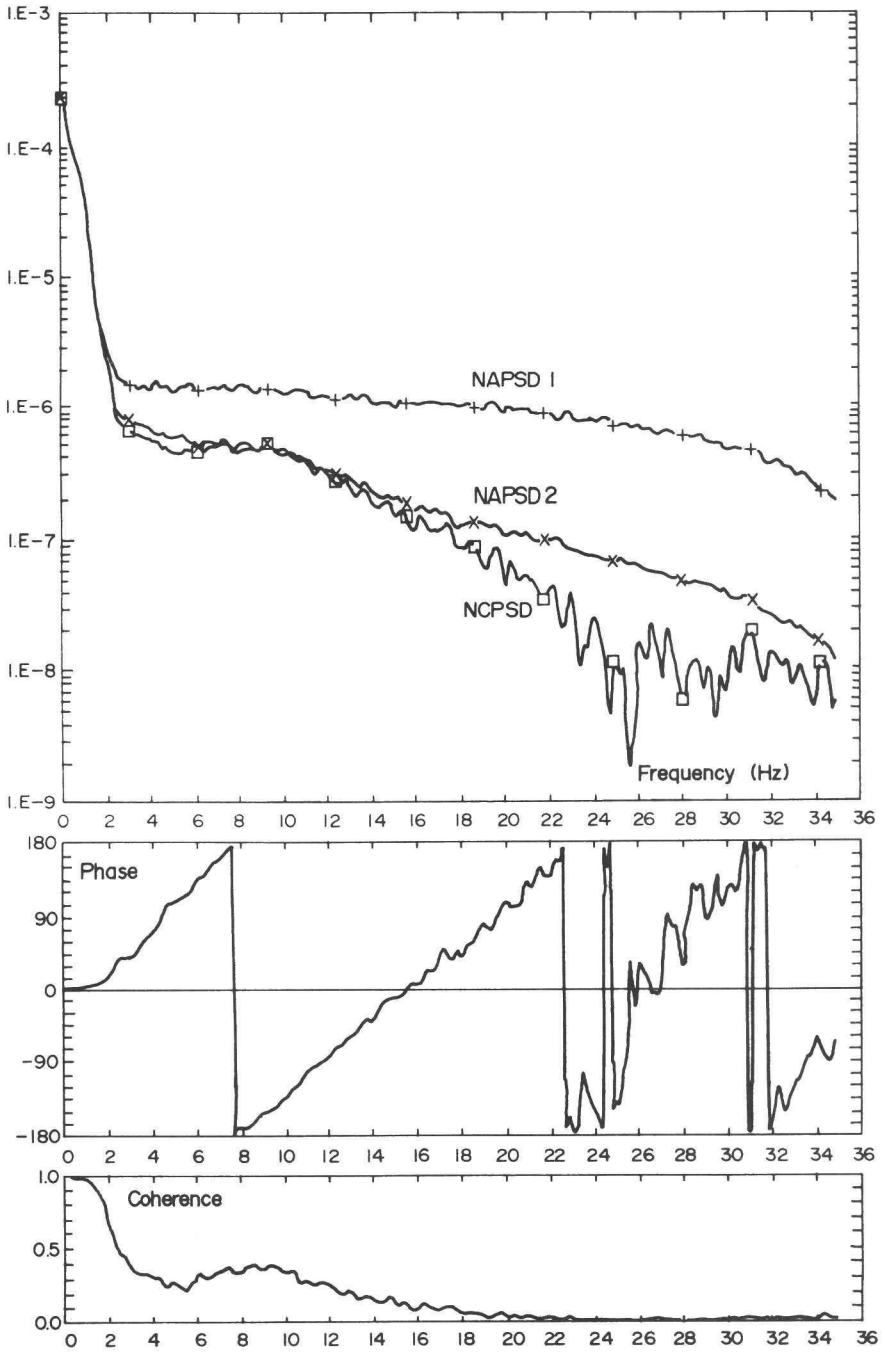

Fig. 1. Auto-, cross-, phase- and coherence-spectra for two axially separated incore neutron detectors.

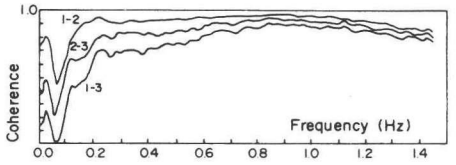

Fig. 2a. Measured coherences for three combinations of radially separated incore neutron detectors.

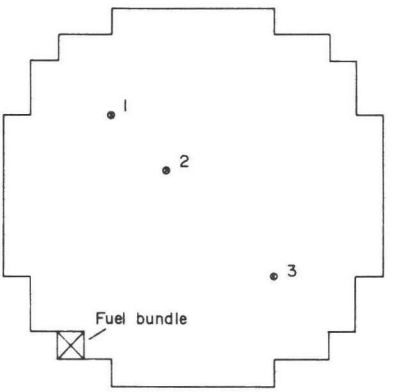

Fig. 2b. Core top view with detector positions (1, 2, 3).

parametric (cross-section) fluctuations in the core and is observed by the detector via a 'field of view' associated with it. This field of view is determined by some typical relaxation length, depending on core parameters (diffusion length, migration area, reactivity). If this relaxation length is much larger than the core dimension, the global noise field can be handled with point reactor kinetics. If this condition is not satisfied, space dependent effects will occur. Apparently this is the case in our experiment. Now we can explain the observed effect on the coherence by two assumptions, which are rather obvious:

(1) The field of view of each detector is frequency dependent (as will be demonstrated later);
(2) the noise source driving the detector signal fluctuations is spatially distributed in the core and uncorrelated in the horizontal plane. (Such a noise source can easily be found in the boiling process in a BWR).

If two neutron detectors are positioned in a medium with such a noise source, both will see a somewhat different region of the source. This is clarified in Fig. 3 where the fields of view of the two detectors are sketched. Because of the uncorrelated character of the noise source, the coherence of the detector signals will be determined by the region of the source common to both detectors (i.e. the overlapping area drawn in Fig. 3) relative to the total region in the field of view. It will be clear now that if the distance between the detectors increases, the coherence will decrease (when the field of view does not change). On the other hand, if the field of view changes the coherence will be affected too (shown by the dashed curves in Fig. 3). This change in the field of view can be imagined as follows. The field of view is in fact determined by the propagation of the neutron wave caused by the fluctuating cross sections. This propagation is dependent on core parameters and it is damped due to feedback effects. These feedback effects are generally frequency dependent and consequently also the neutron wave propagation and detector field of view.

Thus we obtained an understanding in the processes involved in the coherence measurements. To obtain useful results, however, a mathematical framework is needed. For the description of the neutron field in the core we use a two energy group model with one group of delayed neutrons, which covers the most important features of BWR neutron noise. In the zero-power case, the neutron flux fluctuations are coupled to the noise source via the equations (in fre-

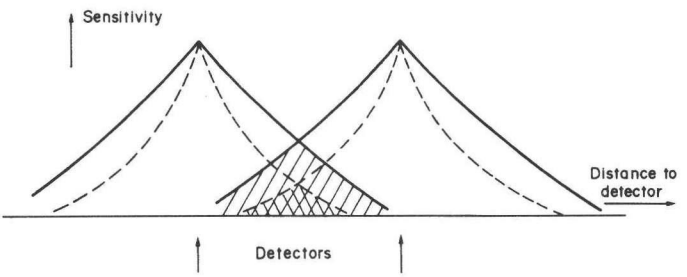

Fig. 3. Schematic representation of detector sensitivities ('fields of view') for two frequencies (solid and dashed curves). The coherence of detector signals stems from the shaded area.

quency domain) (van Dam, 1976):

$$D_1\nabla^2\delta\phi_1 - \left(\Sigma_1 + \Sigma_{12} + \frac{j\omega}{v_1}\right)\delta\phi_1 + \nu\Sigma_f\left(1 - \frac{j\omega\beta}{j\omega + \lambda}\right)\delta\phi_2 = S_1$$

$$D_2\nabla^2\delta\phi_2 - \left(\Sigma_2 + \frac{j\omega}{v_2}\right)\delta\phi_2 + \Sigma_{12}\delta\phi_1 = S_2. \tag{2.1}$$

Here S_1 and S_2 are the fast and thermal neutron noise source, respectively. They consist of terms like $\phi_{1_0}\delta\Sigma_1$ etc. According to equations (2.1) the neutron noise field is governed by two relaxation lengths l_1 and l_2, being the roots of the coefficient determinant of (2.1). For the zero-power case and a very large reactor ($k_\infty \approx 1$) as has been treated by van Dam (1976) and Behringer (1977), they are

$$l_1^2 \approx \left(\frac{1}{L^2} + \frac{1}{\tau}\right)^{-1} \approx L^2$$

$$l_2^2 \approx (L^2 + \tau)R(\omega) = M^2R(\omega). \tag{2.2}$$

Here L is the thermal neutron diffusion length, τ the Fermi age (or fast neutron diffusion area), M^2 the migration area and $R(\omega)$ the zero-power reactivity transfer function, which takes for a critical reactor the form

$$R(\omega) = \left[\frac{j\omega\beta}{j\omega + \lambda} + j\omega\Lambda\right]^{-1}.$$

For a smaller reactor the second relaxation length appears to be a generalization of equation (2.2) (see Appendix):

$$l_2^2 = \frac{M^2}{k_\infty}R_\infty(\omega) \tag{2.2a}$$

where $R_\infty(\omega)$ is the transfer function of the infinite medium:

$$R_\infty(\omega) = \frac{1}{\phi_0}\frac{\delta\phi}{\delta\rho_\infty} = \frac{1}{\dfrac{j\omega\beta}{j\omega + \lambda} + j\omega\Lambda - \rho_\infty}. \tag{2.3}$$

The numerical values of l_1 and l_2 (of the order of 2 cm resp. 100 cm for the plateau region of the zero-power transfer function) clearly indicate their connection with the local and global flux behaviour.

In the Appendix it will be shown that for the at-power case the same type of relations hold:

$$l_1^2 \approx L^2$$

$$l_2^2 \approx \frac{M^2}{k_\infty}G_\infty(\omega) \tag{2.4}$$

where G_∞ is the at-power reactivity transfer function of the infinite medium. It includes the power–reactivity feedback effects that occur in the core medium. Because of these effects, G_∞ differs from R_∞ in the lower frequency region. Both zero-power and at-power transfer functions R_∞ and G_∞ are related to the reactivity transfer functions of the actual finite reactor considered, that are defined by

$$R(\omega) = \frac{1}{P_0}\frac{\partial P}{\partial\rho}\bigg|_{\text{zero-power}}; \quad G(\omega) = \frac{1}{P_0}\frac{\partial P}{\partial\rho}\bigg|_{\text{at-power}} \tag{2.5}$$

via the relations (see Appendix, equation (a.14))

$$\frac{1}{G} = \frac{1}{G_\infty} + \frac{M^2B^2}{k_\infty} \tag{2.6a}$$

$$\frac{1}{R} = \frac{1}{R_\infty} + \frac{M^2B^2}{k_\infty} \tag{2.6b}$$

where B^2 is the geometrical buckling of the core.

Following van Dam (1976), we apply perturbation theory to obtain the detector response. The set of equations adjoint to (2.1) is

$$D_1\nabla^2\phi_1^+ - \left(\Sigma_1 + \Sigma_{12} + \frac{j\omega}{v_1}\right)\phi_1^+ + \Sigma_{12}\phi_2^+ = 0$$

$$D_2\nabla^2\phi_2^+ - \left(\Sigma_2 + \frac{j\omega}{v_2}\right)\phi_2^+ + \nu\Sigma_f\left(1 - \frac{j\omega\beta}{j\omega + \lambda}\right)\phi_1^+ = \Sigma_d \tag{2.7}$$

where Σ_d is the detection cross section of the thermal neutron detector. Its response can be found to be

$$Z(\omega) = \int_{V_{\text{core}}} \Sigma_d\delta\phi_2(\bar{r}, \omega)\,\mathrm{d}\bar{r}$$

$$= \int_{V_{\text{core}}} (S_1(\bar{r}, \omega)\phi_1^+(\bar{r}, \omega) + S_2(\bar{r}, \omega)\phi_2^+(\bar{r}, \omega))\,\mathrm{d}\bar{r} \tag{2.8}$$

Here we see the meaning of ϕ_i^+ as a field of view of the detector. It is governed by the same relaxation lengths l_1 and l_2 that apply to the neutron flux.

When two neutron detectors are present, the two signals can be correlated leading to the cross- and autospectra:

$$\Phi_{12}(\omega) = \langle Z_1^*(\omega)Z_2(\omega)\rangle$$

$$= \left\langle \int \mathrm{d}\bar{r} \sum_i \phi_{1i}^{+*}(\bar{r}, \omega)S_i^*(\bar{r}, \omega) \times \int \mathrm{d}\bar{r}' \sum_j \phi_{2j}^+(\bar{r}', \omega)S_j(\bar{r}', \omega)\right\rangle$$

$$= \iint \mathrm{d}\bar{r}\,\mathrm{d}\bar{r}' \sum_i \sum_j \phi_{1i}^{+*}(\bar{r}, \omega)\phi_{2j}^+(\bar{r}', \omega) \times \langle S_i^*(\bar{r}, \omega)S_j(\bar{r}', \omega)\rangle \tag{2.9}$$

where ϕ_{ij}^{+} is the jth group adjoint function for detector i. Analogous equations hold for the auto-spectra Φ_{11} and Φ_{22}. In equation (2.9) we denoted the complex conjugate of the adjoint functions, because these will generally be complex, due to the fact that the coefficients in (2.7) are complex, leading to phase differences between the signals. For the at-power case, equations like (2.7) hold which can be derived from the Appendix. This leads to detector responses similar to (2.8) but with different adjoint functions. The coherence of the signals is defined by

$$\gamma_{12}^{2} = \frac{|\Phi_{12}(\omega)|^{2}}{\Phi_{11}(\omega)\,\Phi_{22}(\omega)}. \tag{2.10}$$

The values of the coherence and spectra are dependent on the behaviour of the adjoint functions (besides, of course, the characteristics of the noise source). This behaviour is governed by l_1 and l_2. Both local and global noise spectra (as far as the noise is caused by the boiling process), have an upper break frequency $f_H = v/2\pi l$ where v is the steam void velocity and l is the applicable relaxation length. This means that the local noise has a much larger bandwidth than the global noise and dominates in the higher frequency region of the spectrum, as can be noticed in Fig. 1. In the low frequency region the global noise component associated with l_2 dominates. Because l_2 is connected to the reactivity transfer function via (2.4) and (2.6), measurements of l_2 via the coherence behaviour for low frequencies give a way of determining the transfer function. The coherence is used, because this quantity is independent of the spectral characteristics of the noise source, because these are eliminated in (2.10). Only the spatial characteristics remain of influence and have to be known in order to determine $G(\omega)$ from the experiments. A method to derive the transfer function from the measurements is demonstrated in the next section.

3. APPLICATION

We will now demonstrate the application of the theory to derive the Dodewaard reactor transfer function from the coherences of Fig. 2a. As has been discussed earlier, the local noise component does not contribute significantly to the detector signal below 1 Hz, where the measurements were performed. Therefore, we can describe the noise field with a one-group model taking only the l_2 root into account, thus reducing the complexity of the problem. The adjoint functions are then determined by the equation

$$\nabla^{2}\phi^{+} - \frac{1}{l^{2}}\phi^{+} = \frac{\Sigma_{d}}{D} \tag{3.1}$$

where

$$\frac{1}{l^{2}} = \frac{k_{\infty}}{M^{2}G_{\infty}(\omega)}. \tag{3.2}$$

The noise source driving the detector noise is to be discussed next.

It is formed by the boiling process in the core, inducing density fluctuations in the water moderator and giving rise to a fluctuating absorption and moderation cross section. We will neglect streaming contributions by the neutron flux gradients (van Dam, 1976; Kleiss, 1979) because these are generally small compared to the moderation effect. The density fluctuations due to boiling are axially correlated due to the steam transport in the fuel element but can be considered radially uncorrelated for different (sub)-channels in the fuel. If we limit our treatment to a two-dimensional R–ϕ or X–Y geometry we can neglect the axial dependence of the core parameters and boiling process by a suited averaging to obtain lumped parameters. The density fluctuations $\delta\sigma$ can then be considered spatially uncorrelated:

$$\langle \delta\sigma^{*}(\bar{r},\omega)\delta\sigma(\bar{r}',\omega)\rangle = \langle \delta\sigma(\bar{r},\omega)^{2}\rangle\delta(\bar{r}-\bar{r}'). \tag{3.3}$$

This relation can also be used for weakly correlated fluctuations, as long as the correlation distance is small compared with l.

The noise source is related to the density via

$$S(\bar{r},\omega) = \phi_{0}(\bar{r})\Sigma_{a}\frac{\delta\sigma(\bar{r},\omega)}{\sigma_{0}(\bar{r})}$$

where ϕ_0, Σ_a and σ_0 are the stationary flux, absorption cross section and density. If we assume the neutron flux and variance of the density fluctuations constant over the core area, the noise source takes the form

$$\langle S^{*}(\bar{r},\omega)S(\bar{r}',\omega)\rangle = C(\omega)\delta(\bar{r}-\bar{r}') \tag{3.4}$$

These assumptions are justified by considering the power distribution in the core, which is pursued to be flat for economic reasons.

The detector response is computed from (2.8) as

$$Z_{i}(\omega) = \int \phi_{i}(\bar{r},\omega)\,S(\bar{r},\omega)\,\mathrm{d}\bar{r}. \tag{3.5}$$

The auto- and cross-spectra are evaluated as

$$\begin{aligned}\Phi_{ij}(s) &= \langle Z_{i}^{*}(\omega)Z_{j}(\omega)\rangle \\ &= \Big\langle \iint \mathrm{d}\bar{r}\,\mathrm{d}\bar{r}\;\phi_{i}^{+*}(\bar{r},\omega)\phi_{j}^{+}(\bar{r}',\omega) \\ &\quad \times S^{*}(\bar{r},\omega)S(\bar{r}',\omega)\Big\rangle \\ &= C(\omega)\int \mathrm{d}\bar{r}\,\phi_{i}^{+*}(\bar{r},\omega)\phi_{j}^{+}(\bar{r},\omega) = C(\omega)I_{ij}(\omega)\end{aligned} \tag{3.6}$$

and the coherence as

$$\gamma_{ij}^2(\omega) = \frac{|I_{ij}(\omega)|^2}{I_{ii}(\omega)I_{jj}(\omega)} \tag{3.7}$$

and thus only dependent on the behaviour of the adjoint functions via I_{ij}. With three detectors available, we can measure three coherence points for every frequency. From these measurements we can fit the relaxation length l and thus the transfer function. This is established in the following way. We rewrite equation (3.1) as

$$\nabla^2\phi_i^+ - A\phi_i^+ = \delta(\bar{r} - \bar{r}_{D_i}). \tag{3.8}$$

where $\bar{r}_{D_i}$ is the position of the detector under consideration. Now we calculate a set of adjoint functions for several values of A, for each detector. This is done using the computer code EXTERMINATOR-II (Fowler *et al.*, 1967) with an $X-Y$ geometry. The mesh width is chosen as 6.35 cm (half the fuel bundle width). Detectors are represented by a neutron source contained in one mesh element, corresponding approximately with the position of the actual detector used in the experiment. Because of difficulties in describing boundary conditions of the cylindrical core in an $X-Y$ geometry, the core is surrounded by a strong neutron absorbing material to complete the square mesh. In this way we established a zero flux boundary around the core. The geometry is given in Fig. 4.

After having calculated the adjoint functions for every detector for several values of A, we can calculate the adjoint flux product integrals used in equations (3.6) and (3.7) and from this a set of coherences. These are shown in Fig. 5. The possible values of A are bounded by $-B^2(-0.00072)$ for criticality reasons: no stationary adjoint functions exist in a supercritical system. Furthermore we have limited ourselves to real values of A only (see Discussion). Now using A as parameter, we fit the measured and calculated coherences for each frequency using a least

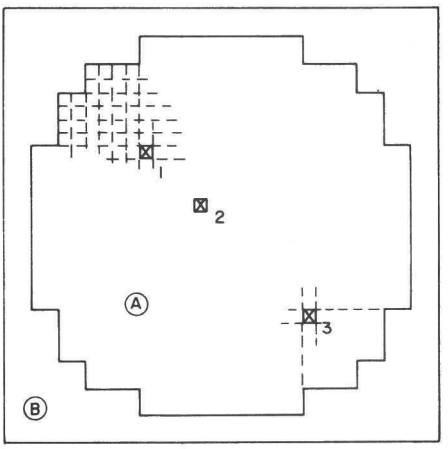

Fig. 4. Geometry for adjoint flux calculations. Region A represents the core, B the absorber surrounding it. The mesh is indicated (core, top left); mesh elements marked 1, 2, 3 represent the neutron detectors.

squares criterion, leading to a best-fitting value $A_{\text{fit}}(\omega)$. Using equations (3.1) and (3.2) we find that

$$G_\infty(\omega) = \frac{k_\infty}{M^2 A_{\text{fit}}(\omega)} \tag{3.9}$$

and

$$G(\omega) = \frac{k_\infty}{M^2(A_{\text{fit}}(\omega) + B^2)} = \frac{1 + M^2B^2}{A_{\text{fit}}(\omega)M^2 + M^2B^2}. \tag{3.10}$$

Assuming a migration area of 80 cm^2 for the Dodewaard reactor at full power conditions (Bruggink, 1978) we find a transfer function that is given in Fig. 6. The accuracy of the obtained transfer function is, of course, dependent on the accuracy in the migration area. Furthermore, it is dependent upon the goodness of the fit and of the variance in the measured coher-

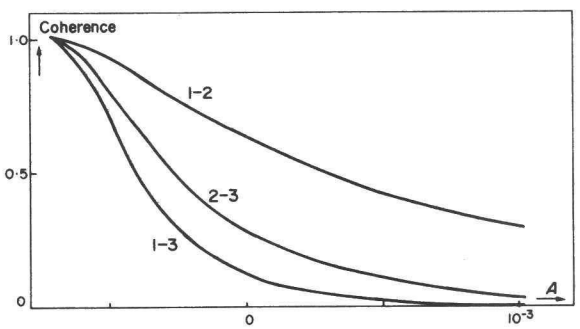

Fig. 5. Calculated coherences as function of the parameter A for three detector combinations.

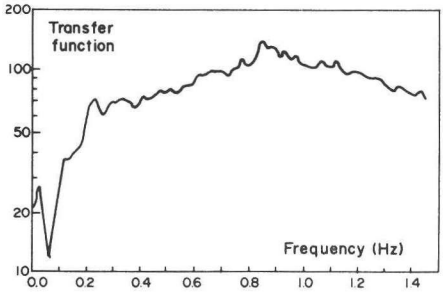

Fig. 6. Reactor transfer function fitted from the data of Fig. 2a.

ences. The standard deviation of the measurements is for all measuring points better than 0.022. The difference between observed and fitted coherence is always less than 0.05 (mostly 0.02) in the frequency region of 0.1–0.9 Hz, resulting in an accuracy better than 10% (mostly 5%) in the transfer function. Outside this frequency region the fit was worse.

The resulting transfer function in Fig. 6 is not unrealistic. For low frequencies it decreases due to power feedback effects (mainly void reactivity). On the high frequency side it tends to reach values of 130–140, which are in the range of the plateau region. The burnup conditions of the core during the measurements (about 30% Pu-fission power production) indicate a β of 0.6%, so a plateau of 165. This level is not reached in the region to 0.9 Hz due to the presence of the feedback and at higher frequencies due to reasons discussed later. However, no other indications of the correctness of the transfer function are available at this moment, because the at-power reactivity transfer function of the Dodewaard reactor has never been measured.

4. DISCUSSION

Although the results of the fit appear rather good, some remarks have to be made on the assumptions underlying the results and on details of the fitting procedure.

1. There is the question whether the measured coherences are the result of only the type of noise source that is considered in this paper. In the high frequency region this is certainly not the case. At frequencies above 2 Hz the signals are fully determined by the local bubble noise, that spoils all 'global coherence'. This effect can already be observed in Fig. 6 where at frequencies above 0.9 Hz the coherence and associated transfer function decrease. One would not expect the upper break frequency of the transfer function to be at such a low frequency (indicating a neutron generation time of 1 ms which is too large for a LWR). So we can conclude that due to the local noise contribution, transfer functions cannot be measured at frequencies higher than about 1 Hz.
   On the low frequency side of the spectrum another effect occurs. It can be noticed that at two frequency points where one coherence function reaches the same value, the other coherences do not (e.g. at 0.02 and 0.1 Hz). This inconsistency is an indication of the presence of some other noise source that influences the coherence. For instance, from other experiments we have indications that the 0.02 Hz peak is induced by the pressure control system. This type of noise source would give rise to erroneously high coherence. This problem could be overcome using a partial coherence technique to eliminate the effect of other noise sources (e.g. Fukunishi, 1977).
2. A second point to consider is the number of dimensions used. Our adjoint flux calculations were done in a 2-D $X-Y$ geometry. In this plane, the noise source can realistically be considered as uncorrelated. However, in the actual reactor core correlations in the noise source do occur in vertical direction due to void transport. Also the flux shape associated with the point detector in a 3-D geometry is different from that in the 2-D calculation (which in effect considers a line detector). One solution to these problems is to perform 3-D calculations, requiring however much more computer time. Another solution would be to use very long detectors (with a length equal to core height) so that the experiment would approximate a 2-D geometry. This would have the extra advantage that such detectors would give a much smaller signal contribution from local noise, thus enabling the determination of the transfer functions at frequencies substantially higher than 1 Hz.
3. In the model, the approximation was made that the noise source strength is constant over core area (equation (3.4)). If this is not the case, the results would change.
   To estimate the influence of this effect, coherences were calculated with the noise source set to zero in the outer ring of fuel elements, thus simulating a more centred power distriction. It appeared that the coherences changed less than 0.005. This is caused by the fact that the centre region of the core contributes most to the cross spectra. So the effect will only be large if there is a very tilted flux and/or power distribution in the core, which is usually avoided.

4. In the fitting procedure, we have only considered real values of A, leading to only real values of $G(\omega)$. This means that a zero phase curve of $G(\omega)$ is assumed, which is certainly not true. Phase shifts in $G(\omega)$ would in principle give rise to phase shifts between the detector signals. The magnitude of the phase shifts is not directly predictable; e.g. detectors in symmetrical core positions would never show phase shifts, regardless of the phase of $G(\omega)$. No significant phase shifts are measured between any pair of incore detectors. Extending the fitting procedure to complex values of A would enable phase curve determination, if the coherence appears to be sensitive to the transfer function phase.

Although the mentioned effects reduce the value of the actually obtained transfer function, it is clear that the method itself is valuable. As discussed, more research will be necessary to include all effects. However, the results already obtained with rather simple means show promising.

REFERENCES

Behringer K., Kosaly G. and Kostic Lj. (1977) *Nucl. Sci. Engng* **63,** 306.

Bruggink J. A. (1978) Private communication.

Dam H. van (1976) *ATKE* **27,** 8.

Fowler T. B., Tobias M. L. and Vondy D. R. (1967) Report ORNL-4078, Oak Ridge, Tennessee, U.S.A.

Fukunishi K. (1977) *Nucl. Sci. Engng* **62,** 215.

Kleiss E. B. J. and van Dam H. (1979) *Ann. nucl. Energy* **6,** 385.

Kleiss E. B. J. and van Dam. H. (1981) *Nucl. Technol.* To be published.

Kosaly G. (1979) Report KFKI-1979-57, Budapest. *Prog. nucl. Energy.* To be published.

Sides W. H. Jr, Mathis M. V. and Smith C. M. (1977) *Prog. nucl. Energy* **1,** 119.

APPENDIX

In order to derive equation (2.4) we follow the method of van Dam (1976) and Behringer (1977) but include power effects. The two energy group equations with one group of delayed neutrons are

$$D_1\nabla^2\phi_1 - (\Sigma_1 + \Sigma_{12})\phi_1 + \nu\Sigma_f(1-\beta)\phi_2 + \lambda C = \frac{1}{v_1}\frac{\partial\phi_1}{\partial t}$$

$$D_2\nabla^2\phi_2 - \Sigma_2\phi_2 + \Sigma_{12}\phi_1 = \frac{1}{v_2}\frac{\partial\phi_2}{\partial t} \qquad \text{(a.1)}$$

$$\beta\nu\Sigma_f\phi_2 - \lambda C = \frac{\mathrm{d}C}{\mathrm{d}t}.$$

Now we split the cross sections and fluxes in a fluctuating part, linearize and Fourier transform to perform the rest of the analysis in frequency domain. The Fourier transforms of the fluctuating parts are from now on denoted by $\delta\Sigma$ and $\delta\phi$. For ease of methematics we assume that the noise is caused by fluctuations $\delta\Sigma_a$ in the thermal absorption cross section Σ_2. Furthermore, reactor power fluctuations (proportional to thermal flux fluctuations) cause variations in Σ_1, Σ_2, Σ_{12}, $\nu\Sigma_f$ (and D, which we shall neglect here). The relation between these flux- and cross-section-fluctuations determines the power feedback characteristics of the core. In order to include these effects, we need a way to incorporate them in the developed formalism. This can be done without much loss in generality for BWRs by two assumptions:

(1) we consider axially averaged cross sections, so in fact a two-dimensional core model as used in Section 3;
(2) In this model no radial heat diffusion occurs, so that cross-section fluctuations are only caused by the local power fluctuations and not by those in adjacent fuel elements.

In such a case, we can write for the cross-section variations due to feedback:

$$\begin{aligned}
&\delta\Sigma_1 = G_r\delta\phi_2 \text{ (resonance absorption)}\\
&\delta\Sigma_2 = G_a\delta\phi_2 \text{ (absorption)}\\
&\delta\Sigma_{12} = G_m\delta\phi_2 \text{ (moderation)}\\
&\delta\Sigma_f = G_f\delta\phi_2 \text{ (fission)}
\end{aligned} \qquad \text{(a.2)}$$

Here G_r, G_a, G_m and G_f are transfer functions which can take any form for a specific reactor. Combining (a.1) and (a.2) and above remarks, we obtain

$$\left[D_1\nabla^2 - \left(\Sigma_1 + \Sigma_{12} + \frac{j\omega}{v_1}\right)\right]\delta\phi_1 + \left[\nu\Sigma_f\left(1 - \frac{j\omega\beta}{j\omega+\lambda}\right) - \phi_{1_0}(G_r + G_m) + \phi_{2_0}G_f\left(1 - \frac{j\omega\beta}{j\omega+\lambda}\right)\right]\delta\phi_2 = 0 \qquad \text{(a.3)}$$

$$\left[D_2\nabla^2 - \left(\Sigma_2 + \frac{j\omega}{v_2}\right) - \phi_{2_0}G_a + \phi_{1_0}G_m\right]\delta\phi_2 + \Sigma_{12}\delta\phi_1 = \delta\Sigma_a\phi_2.$$

Here the subscript zero denotes the stationary value. Set (a.3) is the base set of equations from which (2.2), (2.3) etc. will be derived. The noise source is represented by $\delta\Sigma_a\phi_{2_0}$.

Now to determine G_∞, the transfer function for the infinite medium as defined by

$$G_\infty = \frac{1}{P_0}\frac{\delta P}{\delta\rho_\infty} = \frac{1}{\phi_{2_0}}\frac{\delta\phi_2}{\delta\rho_\infty} \qquad \text{(a.4)}$$

we can set $\nabla^2\delta\phi_i = 0$.

Using furthermore the relations

$$\begin{aligned}
k_\infty &= \frac{\nu\Sigma_f\Sigma_{12}}{\Sigma_2(\Sigma_1+\Sigma_{12})}\\
\rho_\infty &= \frac{k_\infty - 1}{k_\infty}\\
\frac{\delta\Sigma_a}{\Sigma_2} &= -\frac{\delta k_\infty}{k_\infty}\\
l_\infty &= k_\infty\cdot\Lambda = \frac{1}{v_1(\Sigma_1+\Sigma_{12})} + \frac{1}{v_2\Sigma_2}
\end{aligned} \qquad \text{(a.5)}$$

and

$$\frac{\omega}{v_1(\Sigma_1 + \Sigma_{12})} \ll 1, \quad \frac{\omega}{v_2\Sigma_2} \ll 1 \tag{a.6}$$

we find after some algebra

$$G_\infty(\omega) = \left[\frac{j\omega\beta}{j\omega + \lambda} + j\omega\Lambda - \rho_\infty + \left(\phi_{1_0}\frac{G_r + G_m}{\nu\Sigma_f} + \phi_{2_0}\frac{G_a}{\Sigma_2 k_\infty} - \phi_{1_0}\frac{G_m}{\Sigma_2 k_\infty} - \frac{\phi_{2_0}G_f[1 - 8j\omega\beta/(j\omega+\lambda)]}{\nu\Sigma_f}\right)\right]^{-1}. \tag{a.7}$$

If no power feedback occurs (all G_x are zero), equation (a.7) reduces to

$$R_\infty(\omega) = G_\infty(\omega)|_{\text{zero-power}} = \left[\frac{j\omega\beta}{j\omega + \lambda} + j\omega\Lambda - \rho_\infty\right]^{-1}. \tag{a.8}$$

Note that the infinite transfer functions R_∞ and G_∞ do not have the usual physical meaning of a transfer function. However, their appearance in the model, their form and their relation to $R(\omega)$ and $G(\omega)$ justify the name.

The second problem is to derive the expression for the relaxation lengths l_1 and l_2 used in Sections 2 and 3 and to show their relation with G_∞. We use equation (a.3) again where we introduce

$$\nabla^2\phi_i = \frac{1}{l^2}\phi_i$$

to find the eigenvalues l from the equation:

$$\left[\frac{D_1}{l^2} - \left(\Sigma_1 + \Sigma_{12} + \frac{j\omega}{v_1}\right)\right]\left[\frac{D_2}{l^2} - \left(\Sigma_2 + \frac{j\omega}{v_2}\right) - \phi_{2_0}G_a + \phi_{1_0}G_m\right] - \Sigma_{12}\left[\nu\Sigma_f\left(1 - \frac{j\omega\beta}{j\omega + \lambda}\right) - \phi_{1_0}(G_r + G_m) + \phi_{2_0}G_f\left(1 - \frac{j\omega\beta}{j\omega + \lambda}\right)\right] = 0. \tag{a.9}$$

Writing

$$\frac{1}{l^2} = \alpha,$$

(a.9) takes the form

$$\alpha^2 - b\alpha + c = 0 \tag{a.10}$$

where

$$b = \frac{\Sigma_1 + \Sigma_{12} + \frac{j\omega}{v_1}}{D_1} + \frac{\Sigma_2 + \frac{j\omega}{v_2} + \phi_{2_0}G_a - \phi_{1_0}G_m}{D_2}$$

$$c = \frac{\left(\Sigma_1 + \Sigma_{12} + \frac{j\omega}{v_1}\right)\left(\Sigma_2 + \frac{j\omega}{v_2}\right) + \phi_{2_0}G_a - \phi_{1_0}G_m}{D_1D_2} - \frac{\Sigma_{12}\nu\Sigma_f}{D_1D_2}\left[\left(1 + \frac{\phi_{2_0}G_f}{\nu\Sigma_f}\right)\left(1 - \frac{j\omega\beta}{j\omega + \lambda}\right) - \phi_{1_0}\frac{G_r + G_m}{\nu\Sigma_f}\right]. \tag{a.11}$$

The solutions of (a.10) are

$$\alpha_{1,2} = \tfrac{1}{2}b\left[1 \pm \sqrt{\left(1 - \frac{4c}{b^2}\right)}\right].$$

When we assume

$$4c \ll b^2, \tag{a.12}$$

then

$$\alpha_1 = b \text{ and } \alpha_2 = \frac{c}{b}.$$

Assuming furthermore

$$\frac{\phi_{x_0}G_x}{\Sigma_x} \ll 1 \tag{a.13}$$

and using equations (a.5) and (a.6) we obtain without any further approximations

$$\frac{1}{l_1^2} = \frac{\Sigma_1 + \Sigma_{12}}{D_1} + \frac{\Sigma_2}{D_2} = \frac{1}{\tau} + \frac{1}{L^2} \approx \frac{1}{L^2}$$

$$\frac{1}{l_2^2} = \frac{k_\infty}{(L^2 + \tau)}\frac{1}{G_\infty(\omega)} = \frac{k_\infty}{M^2G_\infty(\omega)} \tag{a.14}$$

which are the results of van Dam (1976) and Behringer (1977) but now proven to be also applicable to the at-power case.

The assumptions (a.12) and (a.13) are justified as follows. Realistic values for the magnitude of the transfer function G are between 10 and 150. From this we can estimate the magnitude of the feedback components $\phi_{x_0}G_x/\Sigma_x$:

$$\frac{1}{G_\infty} = \frac{1}{G} - \frac{M^2B^2}{k_\infty} = \frac{1}{G} - \rho_\infty$$

for a critical reactor and using (a.7) we find for the low-frequency region

$$\left|\frac{\phi_{x_0}G_x}{\Sigma_x}\right| \approx \left|\frac{1}{G}\right| < 0.1$$

where

$$\frac{\phi_{x_0}G_x}{\Sigma_x}$$

denotes the sum of the feedback components. Using (a.11), we find

$$\frac{c}{b^2} = k_\infty\frac{L^2}{\tau}\frac{\left(-\rho_\infty + \frac{\phi_xG_x}{\Sigma_x} + j\omega\Lambda + \frac{\beta j\omega}{j\omega + \lambda}\right)}{\left(1 + \frac{L^2}{\tau} + \frac{\phi_{2_0}G_a}{\Sigma_2} - \frac{\phi_{1_0}G_m}{\Sigma_2}\right)^2} \ll 1$$

for all LWRs, even if (a.12) would not hold, because

$$\frac{L^2}{\tau} \ll 1 .$$

The relations (2.6) between G_∞ and G can be derived as follows. Using simple one-group neutron kinetics with delayed neutrons and an absorption type noise source:

$$D\nabla^2\delta\phi + \nu\Sigma_f\left(1 - \frac{j\omega\beta}{j\omega + \lambda}\right)\delta\phi - \Sigma_a\delta\phi - \frac{j\omega}{v}\delta\phi = \delta\Sigma_a\phi_0$$

we obtain

$$M^2\nabla^2\delta\phi - k_\infty\left(\frac{j\omega\beta}{j\omega + \lambda} + j\omega\Lambda - \rho_\infty\right)\delta\phi = \frac{\delta\Sigma_a}{\Sigma_a}\phi_0$$

where

$$\left(\frac{j\omega\beta}{j\omega + \lambda} + j\omega\Lambda - \rho_\infty\right)$$

can be denoted as $[R_\infty(\omega)]^{-1}$.

For the at-power case replace R_∞ by G_∞:

$$M^2\nabla^2\delta\phi - \frac{k_\infty}{G_\infty(\omega)}\delta\phi = \frac{\delta\Sigma_a}{\Sigma_a}\phi_0 . \qquad \text{(a.15)}$$

For the infinite reactor, $\nabla^2\delta\phi = 0$ and

$$\frac{\delta\Sigma_a}{\Sigma_a} = -k_\infty\delta\rho_\infty$$

so we obtain

$$\frac{\delta\phi}{\phi_0} = G_\infty\delta\rho_\infty$$

as expected.
For the finite reactor,

$$\nabla^2\delta\phi = -B^2\delta\phi \text{ and } k = \frac{k_\infty}{1 + M^2B^2} = \frac{\nu\Sigma_f}{\Sigma_a + DB^2} .$$

From this,

$$\frac{\delta\Sigma_a}{\Sigma_a} = -k_\infty\,\delta\rho$$

which leads to

$$\frac{\delta\phi}{\phi_0} = \frac{\delta\rho}{\dfrac{1}{G_\infty} + M^2B^2/k_\infty} .$$

The r.h.s. is by definition $G(\omega)\delta\rho$ so we obtain the relation:

$$\frac{1}{G(\omega)} = \frac{1}{G_\infty(\omega)} + \frac{M^2B^2}{k_\infty} . \qquad \text{(a.16)}$$

CHAPTER 5. THE DETERMINATION OF THE REACTOR TRANSFER FUNCTION FROM THE SPACE DEPENDENCE OF THE NEUTRON NOISE.

5. Abstract.

Using the theory developed in Chapter 4, the practical application is given to derive the reactor transfer function (RTF) from the space dependent properties of the neutron flux noise, both for incore and excore detectors. The distributed noise source is obtained and the adjoint function calculations and fitting procedure are discussed. To validate the estimated RTF's, comparisons are made with RTF's obtained from control rod step experiments and reactor dynamic model calculations. The results generally agree. Finally the effect of vessel pressure noise and pressure feedback is investigated.

5.1. Introduction

In the previous chapter it has been shown that the neutron noise field exhibits some remarkable characteristics (space- and frequency dependence of the coherence in the low frequency region). It is shown that these can be used for the determination of the reactor transfer function (RTF). The principles of the method and the theoretical background have been discussed.

In this chapter the practical application of the theory is presented. The space dependent characteristics of the noise source are derived and the calculation of the adjoint functions of the detectors, involved in the experiments, is discussed. It is shown that, apart from the incore detectors which have been used in the previous chapter, also the ex-core neutron detectors can be used and with some advantages over the incores. The fitting procedure to obtain the RTF from the measured coherences and the elimination of some parasitic effects due to pressure fluctuations are also treated. Finally a comparison is made with RTF's obtained by independent methods.

5.2.Experimental conditions.

The measurements discussed in this chapter are based on the results of two specific experimental sessions: the two control rod experiments that were performed (see Appendix 1), in combination with measurements of the associated reactor noise signals. Of the many performed noise measurements, these offer the opportunity to obtain a comparison of the noise-based RTF's with the ones based on independent methods. Combined experiments are necessary, as results obtained at different instants may be incomparable due to changes in reactor conditions.

The results from the first experiment (EXP1) could be used without complications: noise signals and the accompanying control rod step response signals were measured under satisfactory conditions. The measurements were performed at March 17,1981 at a reduced thermal power level of 135 MW.

A second experiment (EXP2) was performed at Jan 6,1982, with the intention to obtain more accurate results from the control rod experiments. However, the extreme change in power distribution due to the insertion of only the central control rod for this experiment, decreased the stability of the reactor and a large peak at 0.15 Hz appeared in the spectra of the neutron signals. This is ascribed to decreased stability of the bubble column above the core and the chimney which had been observed earlier(1). This peak (to be interpreted as an extra reactivity noise source at that frequency) completely masks the normal behavior of the neutron detector signal coherence in the low frequency region and thus inhibits the application of the presently discussed methods to obtain the RTF. Noise measurements were available at full power conditions (162 MW), immediately preceding the power reduction thus some useful results can be obtained from EXP2.

In the experiments, noise signals were recorded of in- and ex-core neutron detectors,vessel pressure, steam flow to the turbine and several other process variables. Figure A1.3 (Appendix 1) shows a top view of the core with the different neutron detector positions. Note that the ex-core detectors are actually located in the concrete biological shield, approximately 2m from the core surface. The measured spectra and coherences are based on the following recorded signal durations: EXP1, incores 1.9h; EXP1, excores 4.1h; EXP2, excores 3.8h. For more details on the experimental conditions is referred to Appendix 1.

5.3.Estimation of the noise source distribution.

The coherence of the observed neutron noise signals is determined by the detector fields-of-view (in the analysis represented by the adjoint functions) and by the spatial distribution of the boiling noise source in the core. This has been derived in the previous chapter. For spatially uncorrelated noise sources, the (cross)spectra S_{ij} of the signals i and j are given by

$$S_{ij}(f) = \int_{V_{core}} \phi_i^{+*}(\underline{r},f)\phi_j^{+}(\underline{r},f)\phi_0^2(\underline{r})\sigma^2(\underline{r},f)d\underline{r} \qquad (1)$$

where ϕ_i^+,ϕ_j^+ are the detector adjoint functions, $\phi_0(\underline{r})$ the stationary neutron flux distribution and $\sigma^2(\underline{r},f)$ the space dependent spectrum of the moderator density fluctuations due to the boiling process. Eq.(1) can be rewritten as

$$S_{ij}(f) = \int_{V_{core}} \phi_i^{+*}(\underline{r},f)\phi_j^{+}(\underline{r},f)Q(\underline{r},f)d\underline{r} \qquad (2a)$$

$$Q(\underline{r},f) = \phi_0^2(\underline{r})\sigma^2(\underline{r},f) \qquad (2b)$$

with Q the effective neutron noise source that causes the signal fluctuations. The signal coherence γ^2 can be computed from the spectra:

$$\gamma_{ij}^2(f) = S_{ij}^*(f)S_{ij}(f)/S_{ii}(f)S_{jj}(f) \qquad (3)$$

If it is assumed that the noise source can be split into a space- and a frequency-dependent part, the spectral properties of Q are eliminated when the signal coherence is considered. Only the spatial properties of Q and the space/frequency dependence of ϕ^+ remain. From now on, we will neglect the spectral properties of Q and refer to $Q(\underline{r})$ as the spatial distribution.
In Chapter 4, it was assumed that Q was constant over the core area. This is the most simplified approximation, which is not valid in practice. In Sect.5.5 it will be shown that the assumed spatial distribution has a substantial effect on the fitted RTF so a realistic estimate is required. This can be obtained by considering the flux- and power density distributions in the core, which are obtained by the flux mapping system and associated computer program TIPPEL (1). According to Eq.(2b), the moderator density fluctuation distribution $\sigma^2(\underline{r})$ has to be known. It will be clearly dependent on bundle power but the exact degree is not known. It will be assumed that a proportionality with the bundle power exists:

$$\sigma^2(\underline{r}) = \text{constant}.P(\underline{r}) \qquad (4)$$

At present no better model was available. Some indication of the correctness may be found in the approximate proportionality of the neutron noise NAPSD with power level observed at EXP2 (see Fig.5.1). For the noise source distribution Q is thus found, apart from a constant factor that is lost in the coherence calculation,

$$Q(\underline{r}) = \phi_0^2(\underline{r})P(\underline{r}) \qquad (5)$$

Note that Q is dependent on the cube of the power, leading to a proportionality with power of the normalised spectra. For EXP1, the flux- and power distribu-

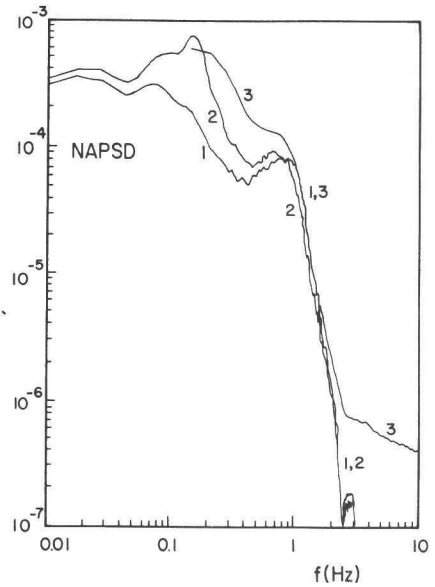

Fig. 5.1
Spectra of excore flux N5 at full power (1) and reduced power (2) and incore AT (3).

tions were available from measurements and could be used to obtain $Q(\underline{r})$. For EXP2, the distributions were measured at reduced power (142MW). As the noise measurements at reduced power were not suited, the noise measurements at full power (i.e.162MW) were analysed. The actual power and flux distributions were estimated from the measured reduced power case via the comparison of reactor thermal power reduction and the associated ex-core flux decrease. From the power reduction (162 to 142 MW) and the flux decrease (11.2%) the power depression in the central bundles due to the control rod insertion was estimated and compensated for in the determination of the full power flux distribution.

				21	17	17		28	27	21				
		15	24	34	42	47		80	66	37	22	14		
	15	28	42	55	74	88		106	99	74	56	69	14	
	25	42	91	97	132	143		162	154	145	127	58	21	
21	34	57	103	96	116	185		168	152	161	149	70	33	19
18	43	80	143	128	145	191		159	167	161	166	90	48	20
16	46	94	161	203	193	184	337	206	173	169	194	175	92	58	20
						243	206	221	233					

Fig. 5.2
Noise source distributions (arbitrary units) for the two experiments. Left: EXP1 (135 MW); Right: EXP2 (162 MW).

The obtained noise source distributions are shown in Fig.5.2. Except for the four central bundles, the core is symmetrical so only one quadrant is shown. It appears that the noise source is mainly concentrated in the core centre where flux and power density are maximal.

5.4.The estimation procedure for the RTF.

The RTF is obtained by fitting the measured coherences between the several detector signals with computed ones. The computed coherences are obtained by Eqs.(1-3) from the detector adjoint functions, calculated for varying values of the core parameter A (See Chapter 4). These calculations were performed with one-group diffusion theory in a two-dimensional square X-Y geometry shown in Fig.5.3. The mesh width, etc are discussed in Chapter 4. The geometry differs from the one used there, since also ex-core detectors had to be included. The choice of this geometry is motivated by the following considerations.

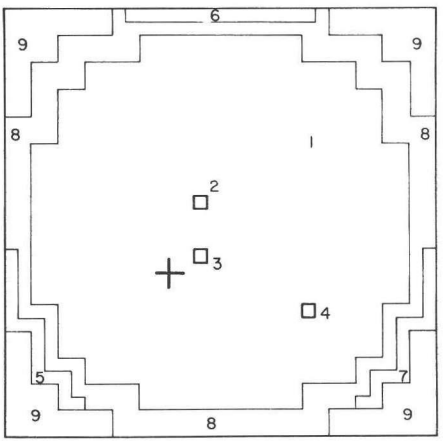

Fig.5.3
Geometry for the EXTERMINATOR-II adjoint function calculations. Control rod and incore detector positions are shown for EXP1.

The core is represented by region 1. Inside the core, the regions 2, 3 and 4 represent the incore detectors available at EXP1. These regions act as sources for the adjoint function calculation. The regions denoted 5, 6 and 7 represent the ex-core neutron detectors N5, N6 and N7 respectivily. This is not precisely according to the actual geometry, which is however far too complex for the present analysis. The ex-core detectors are positioned in the concrete of the biological shield, approximately 3 meters outside the core centre, separated from the core by the reflector water, construction parts, pressure vessel, etc. The choice for the used geometry can be motivated by the following considerations. The ex-core detector signal coherence is determined by the boiling noise source distribution and neutron diffusion process inside the core (if no other noise sources of importance are present). For neutrons escaping the core and penetrating the reflector, the actual geometry only determines the detection efficiency for neutrons produced in different core regions. Due to the distance of the detector to the core surface (more than two meters) and the occurence of neutron scattering in reflector and vessel/shield, it can be assumed that neutrons escaping from the six fuel elements facing N6 will have an equal chance of reaching N6. The detector efficiency for these bundles is approximately equal; the geometry to represent N6 is chosen to simulate this

condition. The regions representing N5 and N7 are chosen such that a similar field-of-view for these detectors around the core is obtained as for N6.
Region 8 represents the water reflector surrounding the core, it is added as an extension of the geometry used in Chapter 4 to enable the inclusion of the ex-core detectors. Region 9 is given a strong neutron absorption cross section and is used to simulate a cilindrical zero-flux boundary condition around the core within the rectangular geometry.
The choice of the cross sections used in the one-group diffusion calculation requires some comments. For the core region (1) and the reflector region (8) the diffusion equations for the adjoint functions are

$$D_1\nabla^2\phi_1^+ - \Sigma_{eff}\phi_1^+ + \Sigma_d = 0 \qquad (6a)$$

$$D_8\nabla^2\phi_8^+ - \Sigma_{a8}\phi_8^+ + \Sigma_d = 0 \qquad (6b)$$

Here Σ_{eff} is a sum of frequency dependent absorption and production cross sections and is related to the core parameter A introduced in Chapter 4,Eq.3.8 to be fitted from the measured coherences. The terms Σ_d represent the adjoint neutron sources and are given a non-zero value in the mesh elements representing the in- or ex-core neutron detector in the applicable case. For ease of computation and comparability with Chapter 4, the equations are normalised to have a unity effective diffusion coefficient in the core region (like Eq.3.1 from Chapter 4), by division by D_1:

$$\nabla^2\phi_1^+ - A\,\phi_1^+ + \Sigma_d' = 0 \qquad (7a)$$

$$\frac{D_8}{D_1}\nabla^2\phi_8^+ - \frac{\Sigma_{a8}}{D_1}\phi_8^+ + \Sigma_d' = 0 \qquad (7b)$$

with A given by

$$A = \frac{1}{\ell^2} = \frac{\Sigma_{eff}}{D_1} \qquad (8)$$

with ℓ^2 discussed in Chapter 4. It represents a kind of effective neutron migration area.
As the diffusion process of neutrons in water is poorly described by one-group diffusion theory (thermal absorption, fast diffusion) the cross sections used for the reflector water have to be approximated. The thermal absorption cross section is used. The diffusion coefficient D_8 is chosen to give the correct neutron migration area (Fermi age plus thermal diffusion area). It is assumed that in this way the description of both absorption and diffusion processes is sufficiently well approximated. For D_1, the fast group diffusion coefficient is used. The numerical values actually used: Σ_{a8}=0.012cm^{-1}; D_8=0.53cm; D_1=1.45cm.

The effective buckling B^2 to be used in the fit can be found by the value of A for which the core is critical and appears to be 5.09 10^{-4} cm^{-2}. It was experienced that the fitted RTF is hardly sensitive to the actual values of the reflector cross sections as long as the correct buckling is used (the buckling does depend on the chosen values).
Adjoint functions have been computed using the computer code EXTERMINATOR-II (2) for several values of A. The coherence between the detectors was then obtained using the estimated noise source distribution. A plot of the obtained coherences γ^2 versus A (actually $\log(1-\gamma^2)$ vs. $\log(A+B^2)$) shows a smooth curve (Fig.5.4) that could be approximated by a polynomial. In this way an interpolation for any value of A was possible.

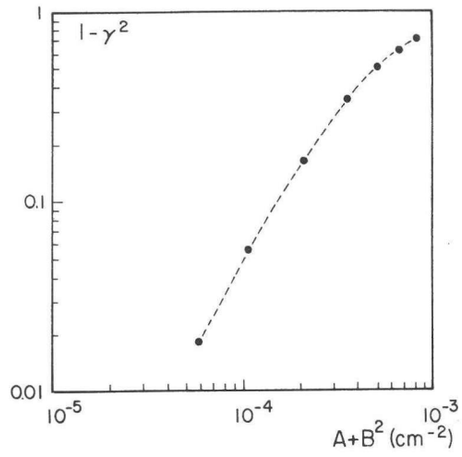

Fig.5.4
Relation between parameter A and calculated coherence γ^2 of N5 and N6.

The relations between A and the coherences thus obtained, were used in a least-squares procedure to fit the measured coherences of the desired detector combinations; in this way a value A(f) was derived for every frequency point. Together with B^2 and an assumed value of the migration area M^2 of 80 cm^2, the reactor transfer function G(f) is found (see Chapter 4):

$$G(f) = \frac{1+M^2B^2}{M^2(A(f)+B^2)} \qquad (9)$$

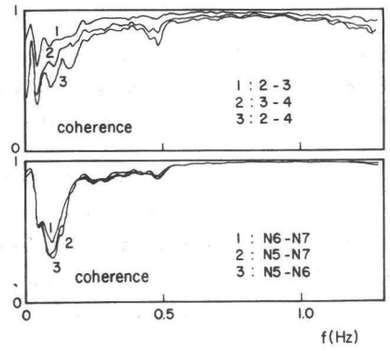

Fig.5.5a and b.
Measured coherence at EXP1:
a: incore detectors 2,3 and 4
b: excore detectors N5,6 and 7

Fig.5.5c
RTF's obtained from coherence of Figs.5.5a and 5.5b:
1: based on incore detectors.
2: based on excore detectors
3: as 2, using flat noise source

Fig.5.5a (top) ,5.5b (bottom)

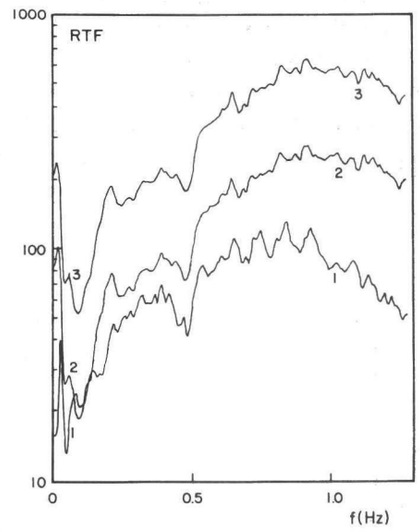

Fig.5.5c

5.5.Results and discussion.

5.5.1.Estimation of the RTF from EXP1. Figure 5.5a shows the measured coherences between the three incore detectors present at EXP1. As discussed in the previous chapter, the essentials of the space dependence are clearly shown: a decrease of coherence with detector distance and a frequency dependence. Fig5.5b. shows the coherences of the ex-core detectors. Due to the approximate symmetry of the detectors around the core, these coherences are nearly equal. Only at low frequencies some differences exist.
The RTF's fitted from these data are shown in Fig.5.5c (curve 1 and 2). The RTF based on the incore measurements is smaller than the one based on the ex-core measurements. Common features of the two estimates are an increase with frequency, as expected from the model calculations in Appendix 3. A peak at 0.02 Hz exists due to a peak in the coherence at that frequency. At frequencies above 0.8Hz, the incore-based RTF decreases; the incore-based RTF reaches a maximum of approximately 100, the other one of 250.
The quite large differences may be explained by the following arguments. The incore detector signal is dominated by local noise, i.e. noise due to the passing of steam bubbles along the detector, at frequencies above 1.5Hz (Fig.5.1

and Chapter 3 and 4). This noise is uncorrelated for different detectors and spoils the coherence. Its influence becomes significant above 0.8Hz and is misinterpreted as a decrease in the fitted RTF. The excore detectors are much less sensitive to this effect.

The remaining difference may be explained by the geometry used in the adjoint calculations. The theoretical coherence for the incore detectors is calculated in a two-dimensional X-Y geometry, in which the detectors are effectively line-shaped. This is a poor approximation for point-shaped detectors. As the adjoint functions tend to decrease faster with distance around a point source than around a line source, the calculated detector fields-of-view are too wide and the coherence is over-estimated. This leads to an underestimation of the RTF. The excore detectors are less sensitive to this effect due to their large distance to the core: neutrons escaping the core surface at different heights contribute about equally to the excore detector signal, so the vertical dependence of the detector field-of-view is of lesser importance. In this case the two-dimensional geometry will be approximated better. Concluding so far, it can be stated that the incore detectors give a good qualitative picture of the space dependent effects but the ex-core detectors are suited better for a quantitative treatment.

Thus assuming that the adjoint functions can be estimated sufficiently correct, a second source of error may be the estimate of the distributed noise source. This effect was investigated by fitting the RTF again using calculated coherences based on a flat (spatially constant) noise source, as in Chapter 4. The resulting RTF is given as curve 3 in Fig.5.5c. It has nearly the same shape but is larger by a factor two. This is an extreme case; it may be expected that errors in the estimated noise source distribution are much smaller, leading to only small deviations in the fitted RTF. No further analysis of this topic was performed.

Apart from the systematic errors discussed above, the statistical precision of the the estimated RTF is of importance. This is determined by the statistical precision with which the coherence can be obtained in the available observation time. Two ways are open to handle this problem. The first is an analysis of the statistical properties of the measured coherence which will give, together with an analysis of the sensitivity of the fitted RTF to variations in the input coherence, a precision of the estimate. Due to the nonlinear fitting procedure this way was considered to be too complex. A second, more straightforward way, is to split the available signals in three sequential parts. For each part, the coherences were calculated and the RTF estimated. This gives three independent estimates for every frequency point from which an average value and an indication of its variance were obtained. Fig.5.6 shows the obtained RTF and its one-sigma standard deviation range. As the estimate of the variance is based on only three points, it is not very precise and exhibited large variations from point-to-point. The curves actually shown were

obtained after a smoothing over three frequency points. From this figure we can conclude that the precision is of the order of 5% for all frequencies, based on the four hours of available signal.

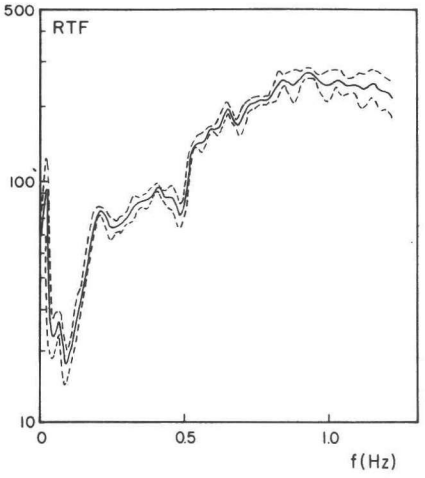

Fig. 5.6
Accuracy estimate of the RTF from three separate analyses. The dashed curves represent the one-sigma standard deviation range.

In order to validate the results obtained previously, comparisons can be made with the results from the first control rod experiment (CRE1,see Appendix 1) and the reactor dynamics model (Appendix 3). Figure 5.7a shows the RTF's based on the responses of the three ex-core detectors. The error intervals are one standard deviation. Due to the excentric position of the control rod, the response of N5 is larger than that of N7 and N6 (see Fig.A1.3). (The difference of the responses is in itself an indication of the deviation from point-kinetics behaviour of the core due to the power feedback; an analysis using the calculated adjoint functions was in qualitative agreement with these observations).

Apart from the difference in the responses, a constant factor may be present in the comparison due to the normalisation of the response measurements. The data is based on a rod step worth of 30pcm (Appendix 1). A more clear comparison can be obtained if the response of N5, N6 and N7 are averaged to estimate the overall reactor power variation. If it is furthermore assumed that the rod worth is 45pcm, the square data points in Fig.5.7b are obtained which are shown together with the noise-based RTF. A very good agreement is obtained above 0.2Hz; even the step-like increase at 0.5Hz can be found in the different results.

At low frequencies, the curves differ. The noise-based RTF's decrease stronger than the step-response based ones. Two possible causes for this deviation were considered. The first is that the responses were observed over only 10 seconds to obtain the indicated datapoints. This limits the resolution and (mainly in the low frequency region) deviations may be expected. A new calculation over

20 and 40 seconds showed that this effect was, however, quite small; except at 0.0Hz, the variations in all points were smaller than the indicated precision intervals. A second possibility is the presence of parasitic pressure noise, which is discussed in more detail in paragraph 5.6.

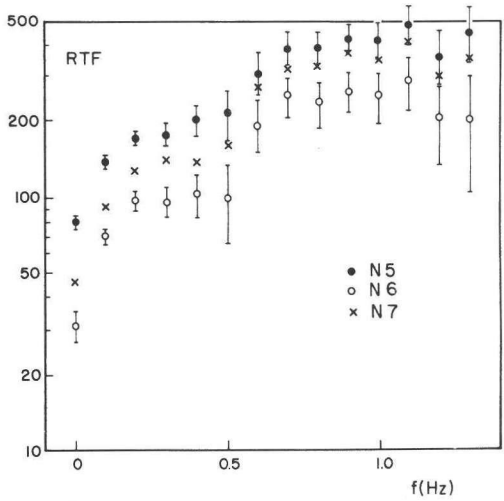

Fig.5.7a

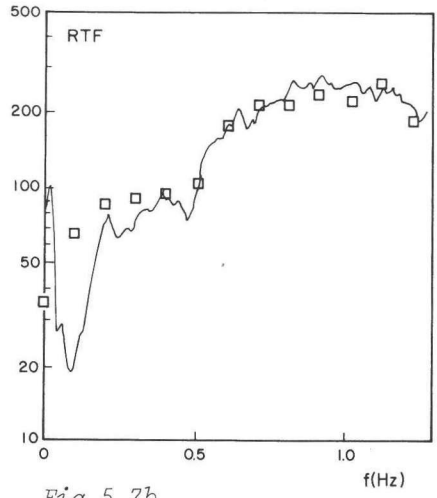

Fig.5.7b

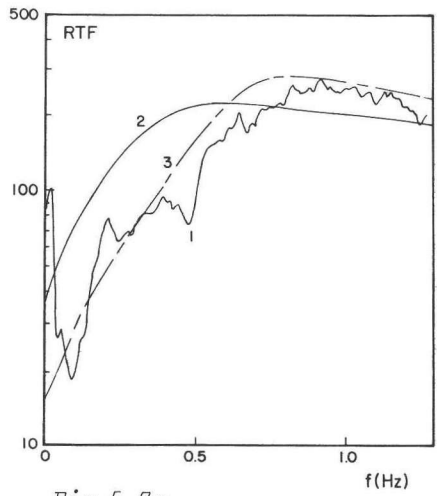

Fig.5.7c

Fig.5.7a-c
a:RTF's from the responses of N5, N6 and N7 at rod step exp CRE1.

b:Comparison of noise-based RTF with average of N5/6/7 response and larger rod step reactivity.

c:Comparison of noise-based RTF (1) with reactor model results for ρ_α*=-0.09 (2), resp. -0.27 (3).*

In Figure 5.7c the noise-based RTF is given, together with results from the model calculations of Appendix 3. Two cases are presented, based on different void reactivity coefficients of -0.09 and -0.27. The agreement is reasonable, specifically for the case with the larger reactivity coefficient. The theoretical curve reaches it maximum at slightly lower frequencies and is somewhat 'steeper'; this difference may be explained by the effect of a smaller effec-

tive fuel time constant than used in the model. The observed fine-structure (a dip at 0.5Hz and a small peak at 0.2Hz) are not present in the model. They are probably due to the details of the steam transport and thermohydraulics in the core and require a more detailed analysis than used in the model.
The required larger void reactivity coefficient (-0.27 instead of -0.09 as has been estimated in Appendices 1 and 3) may be physically correct, referring to the discussion in A1.6. The apparent larger rod step worth of 45 pcm, together with a smaller void fraction change of 0.6% instead of 1% per percent power change leads to a value of -0.25 for the void coefficient.

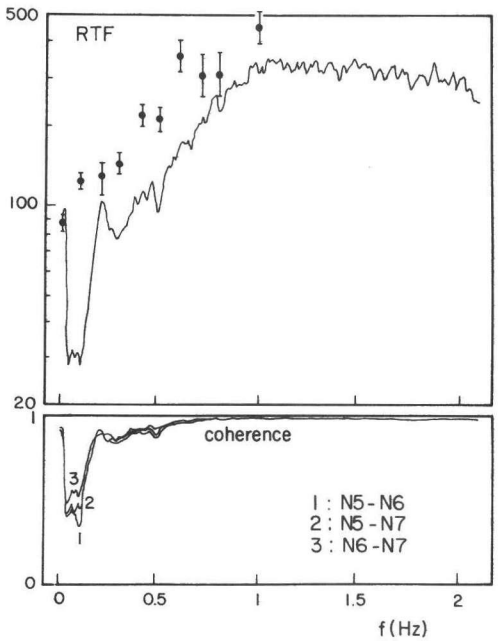

Fig. 5.8
Coherences of N5/6/7 at EXP2 and RTF's obtained from coherence and from N5 response at CRE2.

5.5.3. Estimate of the RTF from EXP2. Figure 5.8 displays the RTF calculated from the coherence of the ex-core neutron detectors at the full power measurements of EXP2. A larger bandwidth was analysed than in the previous section, to demonstrate the ability to obtain the RTF at higher frequencies with the ex-core detectors. The estimated RTF, based on the associated step response measurements (CRE2, see Appendix 1), is also given. Again, a larger value for the rod step worth than the assumed 30 pcm may explain the systematic difference between the results. Two points limit the usefulness of the presently discussed experiment: the smaller accuracy of the step response measurements as compared with CRE1 (due to the larger neutron noise under CRE2 conditions), and the fact that the noise measurements and the step response measurements were performed at different power levels, which reduces the comparability.
Apart from these remarks the results agree reasonably in the region 0.2-1.0Hz (above 1Hz the CRE2 results become too inaccurate to obtain a reasonable com-

parison). The RTF reaches a level of 300. This is too large with respect to the model calculations, unless extreme values for the void reactivity coefficient and the fuel time constant are assumed. One explanation may be an inaccurate estimation of the noise source distribution for this case (Fig.5.3b). A more centred distribution will give smaller values for the RTF.
A second cause may be the presence of other noise sources which give an extra, coherent, contribution to the detector signals. Such a noise source may be the pressure noise, that acts coherently on the void content of all fuel elements. This effect is discussed in the next paragraph.

5.6.Effects of pressure noise.

Due to the large effect of moderator density and void fraction on the reactivity of a BWR and the compressibility of the steam in the core, the reactor power and neutron flux are quite sensitive to variations in the vessel pressure. This leads to an influence on the neutron signals, and thus on the measured RTF's, via two different mechanisms.
The first is the presence of independent reactor pressure noise. In Chapter 6 it will be shown that the ex-vessel steam flow exhibits characteristic oscillations at 1.7 and 3.5 Hz which cause pressure fluctuations and which contribute substantially to the ex-core neutron detector signals.
A second mechanism is the reactivity coupling of different regions in the core via vessel pressure. This may be clarified as follows. Pressure fluctuations are generated by the neutron flux fluctuations, which in turn are caused by the boiling noise in the elements. In this way the power fluctuations in one element give rise to power fluctuations in another element via a kind of spatial feedback loop (actually feed-forward) that short-circuits the neutron diffusion process on which the theory of the previous and this chapter is based.
In order to obtain correct estimates of the reactor transfer functions, the pressure noise source and the pressure-to-power feedback loops must be eliminated. Such an elimination can be achieved by a system identification procedure based on the fitting of a multivariate autoregressive (MAR) model to the measured signals. This method is treated in detail in Appendix 2. After a sufficiently close fit of the measured correlation functions or spectra is achieved, the contributions of the intrinsic noise sources of all signals to all other signals are obtained, together with the transfer functions between the signals. Using these data, the elimination of pressure effects on the neutron flux can be accomplished.
This method will be demonstated on the noise measurements of EXP2. The signals of interest are the three ex-core neutron detector signals N5, N6 and N7 and the vessel pressure D. As much of the pressure noise is generated by fluctuations in the steam flow W_s (Chapter 6), also this signal will be included in the analysis.

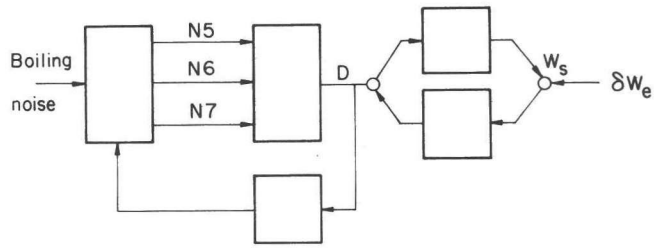

Fig.5.9 *Fig.5.9*
Relations between neutron flux N5,N6 and N7, pressure D and steam flow W_s; the noise sources are δW_e and the distributed boiling noise.

Identification procedure details. The physical relations between the variables of interest are shown in Fig.5.9. The indicated structure suggests that the identification, as far as the neutron signals are considered, will give the same results if only the pressure signal is included and if both pressure and steam flow are included. In practice, however, slightly different results are obtained (see also Chapter 6). Therefore three separate analyses were performed, based on the signal sets (N5,N6,N7,D,W_s), (N5,N6,N7,D) and (N5,N6,N7,W_s). The signals were anti-aliasing filtered at 2.0Hz and sampled with a frequency of 50 samples/second. In total 3.8 hours of signal were processed. Correlation functions and spectra were calculated with a FFT-based algorithm.

As will be discussed in Appendix 2, a sufficiently high sampling rate must be chosen to assure that the indentified noise sources are uncorrelated if the physical noise sources are uncorrelated. For the analyses including the steam flow W_s, 20ms sampling interval appeared not yet fully sufficient; a correlation coefficient of approximately 0.05 remained between the steam flow and neutron flux noise sources. For the analysis excluding W_s, 80ms appeared sufficient to decrease the identified correlation coefficient between pressure and neutron flux noise to less than 0.015. The identified intrinsic noise sources of the neutron signals were found to be fairly strong correlated (0.20 at 20ms) as may be expected from physical reasons. In the analysis, they can be combined and be considered as a single neutronic noise source, uncorrelated with pressure and flow noise sources. All presented results are based on analyses with 20ms sampling interval for ease of comparison. No smaller sampling interval was possible with the available computer system without sacrificing the frequency resolution. A model order of 400 was required for a sufficiently close fit of the coherences, including the 0.02Hz peak.

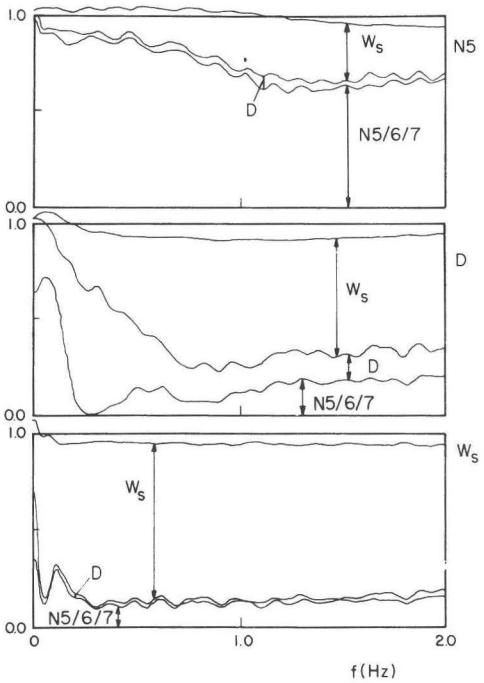

Fig.5.10
Noise Contribution Ratios (NCR's) to neutron flux N5 (top), pressure D (centre) and steam flow W_s (bottom). The areas between the curves represent the relative contribution of the intrinsic noise sources of flux, pressure and steam flow to the signals (see text and Appendix 2).

Results. From the MAR analyses, the noise contribution ratios (NCR's) of the signals are obtained. These give the fraction of the power in each signal, generated by the intrinsic noise sources of all signals. They are defined in Appendix 2. Resulting NCR's of signal N5 and D are shown in Fig.5.10. Due to the remaining correlation between the noise sources in the analyses with W_s, the sum of the NCR's does not precisely equal unity at those cases.

It can be seen that a substantial part of the neutron signal noise is caused by the intrinsic steam flow/pressure noise, up to 30% at higher frequencies. Using the established model, it is easy to eliminate the effect of this noise source by recalculating the coherences with the noise source left out of the model. In a similar way, the effect of pressure feedback is eliminated by leaving the transfer functions from pressure and steam flow to neutron flux out of the calculation. Figure 5.11 shows the results for the five-signal analysis for three cases: 1) coherence based on the complete system; 2) coherence based on eliminated pressure and flow noise sources; 3) coherence based on eliminated pressure feedback (thus implicitly including case 2). The corresponding RTF's from the four-signal analyses differ only slightly and are not given.

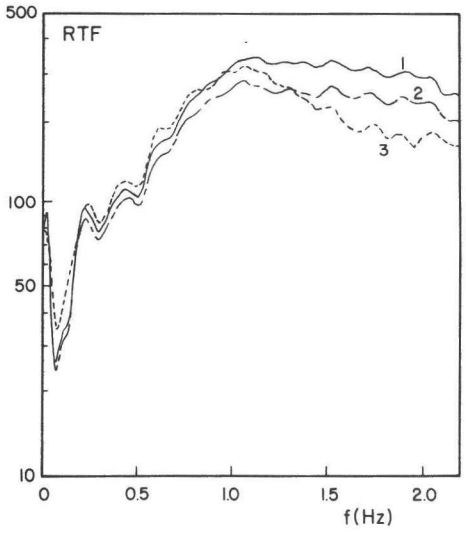

Fig.5.11
RTF's obtained from modified coherences using the fitted AR model:
1: complete system
2: without pressure noise source
3: without pressure to power feedback.

As can be expected, the elimination of the non-neutronic noise gives rise to smaller values for the RTF at higher frequencies. The elimination of the pressure feedback causes a further decrease above 1.0Hz. A small increase is observable at low frequencies. The peaked RTF that remains may be correct; the reactor model calculations exhibit a similar maximum at approximately 1 Hz if the larger value for the void reactivity coefficient is used (see Fig.5.7b). The interpretation of such a variation is difficult. The elimination of the pressure noise can be interpreted as an improvement of the reactor pressure control system. Appendix 3 shows that such an operation hardly affects the RTF, certainly at higher frequencies where the reactivity-generated pressure fluctuations become very small due to the damping by fuel time constant and vessel volume. This point may be related to the identification problems arising in the power-pressure-steam flow complex to be discussed in Chapter 6.
The main conclusion of this paragraph is that the presence of steam flow and pressure noise does have an effect on the RTF's inferred from the noise measurements. The elimination of these effects gives rise to slight variations in the RTF.

5.7.Concluding discussion.

The reactor transfer function, obtained from the space-dependent neutron flux noise, must be validated by comparison with RTF's obtained by independent methods. These are the CRE results and the model calculations. A direct comparison is hindered by the fact that these independent methods contain some free parameters for which a value has to be assumed: the rod step reactivity worth and the void reactivity coefficient. Realistic values can be found, which give a fairly good agreement with the noise-based results.

On the other hand,the present method (although it is quite indirect and perhaps conceptually intricate) is based only on measurements and some parameters which are much better known (power distribution, migration area and geometry). As far as the RTF is sensitive to different parameters of the reactor, it is in principle possible to use the method for the determination of these parameters, which may be difficultly obtained elsewise. In combination with an (improved) reactor dynamics model, e.g. reactivity coefficients and fuel time constants may be measured. The reasonable precision of the RTF estimate (approx. 5% in four hours observation time) accentuates this point, if e.g. compared with the accuracy and experimental problems associated with the step response experiments.

The use of ex-core detectors, in contrast with in-core detectors, enables the determination of the RTF at higher frequencies, in the plateau region of the RTF and perhaps even up to the prompt neutron break frequency (enabling the estimation of the neutron generation time). For that purpose parasitic noise components such as pressure noise (or instrumental noise) have to be eliminated. A possible way to eliminate the pressure noise has been explored but the results are not yet fully satisfactory.

Finally the interpretation of the obtained RTF must be commented. It is strictly defined as a point-kinetics quantity which does not allow for space dependent effects. Precisely these effects are used for its estimation, which leads to inconsistencies in its interpretation. In practice, these points are less severe. A RTF could be defined on basis of the total reactor power which allows for some power profile variations. Furthermore, many reactivity effects normally involved in reactor operation are of a global nature (pressure, coolant temperature), which can be described much better by point reactor models.

5.References.

1. Hoekstra,J. Private communication.
2. Fowler,T.B.,M.L.Tobias and D.R.Vondy. EXTERMINATOR-II: A FORTRAN-IV code for solving multigroup neutron diffusion equations in two dimensions. Report ORNL-4078, Oak Ridge,1967.

CHAPTER 6. AUTOREGRESSIVE MODELLING OF REACTOR NOISE SIGNALS.

6.Abstract

In this chapter examples are given of the kind of information obtainable by autoregressive modelling of the reactor noise signals. For incore neutron detectors, a clear picture is obtained of the transport-like character of the local noise component.

For the combination of steam flow, vessel pressure and reactor power, the noise sources of importance are obtained. These are boiling reactivity noise at low frequencies and acoustical oscillations in the main steam line at higher frequencies. The possibility is demonstrated to obtain information on fuel time constant and vessel steam volume from the measurements, although the results are not very accurate. Larger measuring times will be meaningful.

A further analysis incorporating the controlled pressure and control valve position signals locates some of the steam flow noise in the control system. It appears that the controller produces, at low frequencies, a large part of the steam flow and pressure noise. Finally the pressure controller transfer function and valve coefficients were obtained.

6.1.Introduction.

In the previous chapters, we concentrated on the analysis of the noise signals of neutron detectors. Although this is a very important topic, specifically from reactor physical point of view, also the noise behaviour of other reactor signals is of interest. Such variables may be pressure, temperatures, steam flow, feedwater flow, the in- and outputs of several control systems, generated power, etc. In the first place, the noise in these variables is connected with the neutronic noise and the interaction must be understood to obtain a complete picture of the neutron noise characteristics. In the second place, the noise is interesting in itself as it offers the possibility to obtain information on the characteristics of the auxiliary systems and may thus contribute to improvements in plant operation and safety.

This chapter deals mainly with the study of such process variables. These are generally related via complex feedback loops. The noise is caused by intrinsic fluctuations in some (or all) variables (noise sources), that also affect the other ones. The analysis of such loops requires sophisticated methods, because standard input/output analysis may fail in those configurations. One possible method is the use of autoregressive (AR) modelling techniques, introduced into reactor noise research by Fukunishi(1-3). This technique has been adopted; the principles, applicability conditions and some related topics are discussed in Appendix 2 of this thesis. In this chapter some applications are presented.
Section 6.2 deals with the analysis of the signals of incore neutron detectors. In Sect.6.3 the relation between reactor power, vessel pressure and ex-vessel steam flow is investigated. The main noise sources and some transfer functions are obtained. Finally, Sect.6.4 deals with the behaviour of the pressure control system.

6.2.Analysis of incore detector signals.

A nice demonstration of the usefulness of the AR model to obtain insight in the cause-and-effect relations between signals, can be found in an application to the noise signals of axially separated incore neutron detectors, which are used for steam velocity measurements (see Chapters 2 and 3). Examples of such an application are given in Refs.1 and 4; a more detailed analysis will be given here.

Measurement conditions. Signals were available of a Cobalt self-powered neutron detector (D1) at approximately 120cm from core bottom and a movable fission chamber of the TIP-system (D2), both located at position 2E in the core. Four measurements were performed with varying detector distances of -17cm, -2cm (D2 below D1), 13cm and 28cm (D2 above D1), at full power conditions. The obtained spectra are not shown here, they exhibit the normal characteristics of incore detectors as shown in Chapter 3-5. Detailed information is given in Ref.5. A linear dependence of phase from frequency, due to the dominating local noise component, is present above approximately 2Hz; an in-phase component due to reactivity fluctuations dominates at lower frequencies. Steam transit times τ could be obtained, yielding an average steam velocity of 3.2m/s at this position.
Table 6.1 gives an overview for the four cases, with the available measuring time and fitted steam transit time. The signals were anti-aliasing filtered at 25Hz and sampled with a sampling interval of 14ms.

case number	detector distance (cm)	τ (ms)	T_{meas} (h)	model order	ρ_{12}
1	-17	-53.4	0.54	43	0.12
2	-2	-7.4	0.05	26	0.83
3	13	40.5	0.62	42	0.06
4	28	78.6	1.21	42	0.11

Table 6.1. Measurement and analysis parameters for different incore detector distances.

AR analysis results. Bivariate autoregressive models were fitted to the measured data. The applied model orders, given in Table 6.1 are based on the firstly reached minimum of the AIC (see App.2). It appears that with shorter measuring times (case 2) lower model orders suffice. The remaining correlation coefficient ρ_{12} between the identified noise sources is given, too. The main results from the present analysis are the noise contribution ratios (NCR) of the two identified noise sources to the signal power.

Before the results are presented, some discussion is required to obtain a correct understanding of the results. The fitted AR model will have, inherently, two noise sources for the two signals, which suffice to model the spectra correctly. However, at least three different physical noise sources can be envisaged, that will, in some sense, be distributed over the two modelled ones. This complicates the physical interpretation of the obtained model.

The first noise source is the transport process of the void fluctuations generated below the lower detector. It causes a noise signal in the lower detector and a delayed signal in the upper detector; it will be modelled as the intrinsic noise source of the lower detector signal. A second noise source is the deformation of the void profile due to turbulence and void production between the detectors; as this does not affect the lower detector signal it will form the intrinsic noise source of the upper detector signal, with no contribution to the lower detector signal. The AR model would be very suited for this case, if not a third noise source was present in the reactivity fluctuations, producing simultaneous fluctuations in both signals and dominating at low frequencies. Due to the simultaneousness of the fluctuations, this noise source will give a correlated contribution to the two identified noise sources, in the low frequency region. Two more expected noise sources due to the instrumentation noise, appear to be neglectable from the coherence of the signals at case 2 (5).

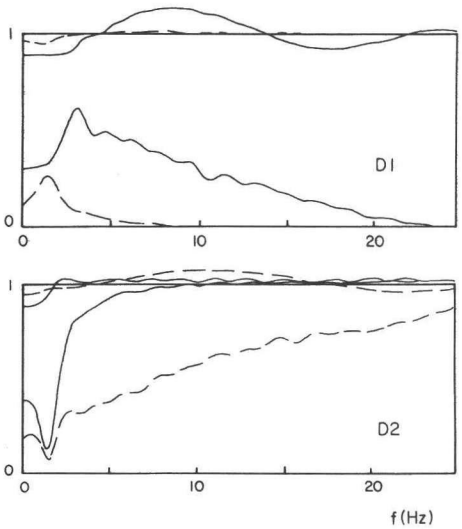

Fig.6.1
Noise contribution ratios of incore detectors D1 and D2.
solid curves: D1 below D2.
dashed curves: D2 below D1.

The discussed points can all be observed in the results. Figure 6.1 displays the NCR's of the two signals for case 1 and 3. Due to the remaining correlation (see Table 6.1) the sum of the NCR's is not unity. This might be improved somewhat by the choice of a higher sampling rate but this effect was not investigated. In the frequency region above 5Hz, it can be seen clearly that the lower detector signal contributes significantly to that of the upper detector, while the reverse is not the case. At lower frequencies (5Hz, minor effects up to 10Hz) both noise sources contribute to the signals as expected from the reactivity noise.

The observed high noise source correlation at case 2 can be commented separately: as the transit time between the detectors (7ms) is smaller than the sampling interval (14ms), a substantial instantaneous response is present in the signals and a high correlation is expected, as observed. (See Appendix 2 for a detailed discussion of this effect).

It can be concluded that the AR model explains the cause-and-effect relation between the local components of the detector signals correctly, even for the case that the physical model is in conflict with the structure imposed by the AR method.

6.3.Analysis of steam flow/vessel pressure/power relations.

6.3.1.General survey. Due to the large effect of pressure variations on the void content and thus the reactivity of a BWR, it is interesting to treat in more detail the relations between power, pressure and the (closely connected) steam flow variations. A diagram representing the physical relationship of the signals is given in Fig.5.9 (Chapter 5).

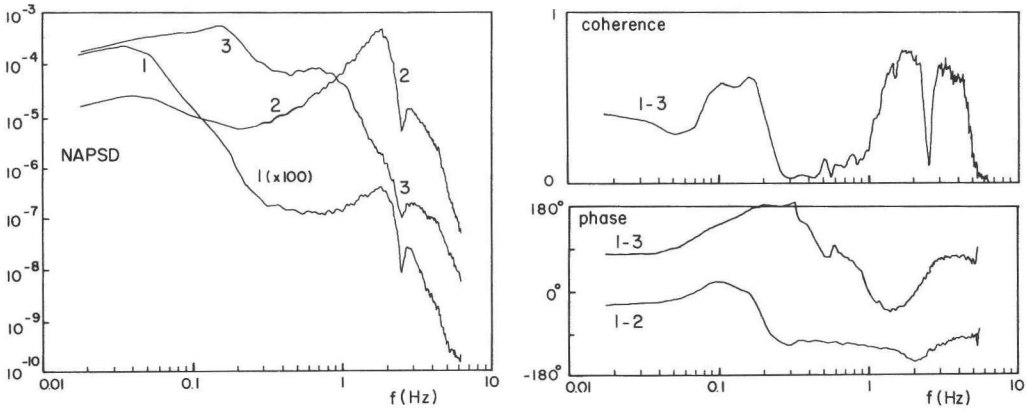

Fig.6.2
Spectra of vessel pressure (1), steam flow (2) and neutron flux N5 (3) with some coherence and phase relations shown.

In Fig.6.2 the spectra, phase and coherence of the signals are shown. The spectrum of reactor power (measured with ex-core neutron detector N5) decreases with frequency. Clear peaks are present in the flow noise spectrum at approximately 1.7Hz and 3.5Hz; these can be observed in the other spectra too. The pressure noise decreases strongly with frequency until the 1.7Hz peak becomes important.
The coherence is fairly high at low frequencies and is nearly absent at 0.3Hz. At higher frequencies, two coherent lobes are present at the same frequencies as the peaks in the spectra. This clearly indicates the same origin of these noise components.

6.3.2.Three-variable AR analyses.
Analysis conditions. To obtain an insight into the main noise sources, the spectra (and phases and coherences) alone are not sufficient. An AR model was fitted to obtain more information. Three analyses were performed of the available data, for three different frequency regions: 1: 0-0.5Hz; 2: 0-1.0Hz; 3: 0-6.5Hz. This was motivated by the following argument. Large sampling frequencies are required to obtain a low correlation between the identified noise sources. The required sampling frequency appears furthermore to increase with signal bandwidth for the present signals. To obtain sufficient resolution in

the low frequency region, the 0-6.5Hz analysis requires unmanageable large model orders (several thousands). For the cases 1 and 2, lower sampling rates could be applied so these cases are used for the low-frequency analyses of the system.
The used signals were steam flow 1FT25 (signal 1), vessel pressure 1PT08 (signal 2) and neutron flux (signal 3). For cases 1 and 2, the incore detector HT at core position D4 was used. This detector was considered to have the largest field-of-view in the low frequency region. This signal is contaminated with local noise above 1Hz, so for case 3 the excore detector N5 was used instead. The signals were measured under the reduced power conditions of EXP2 (see Chapter 5 and Appendix 1). Table 6.2 gives the analysis conditions and the resulting noise source correlations, as function of the sampling interval; the smallest interval mentioned was the one used for the analysis in each case. The remaining correlation was considered to be acceptably small. The resulting NCR's for the three analyses are shown as the solid curves in Fig.6.3a-c.

Band-width (Hz)	Sampling interval (ms)	model order	ρ_{12}	ρ_{13}	ρ_{23}
0.5	80	150	-0.042	-0.030	-0.004
0.5	40	300	-0.021	-0.019	-0.002
1.0	80	75	-0.117	-0.095	-0.012
1.0	40	150	-0.053	-0.049	0.001
1.0	20	300	-0.024	-0.024	-0.001
6.5	20	50	-0.060	-0.12	0.004
6.5	10	50	-0.030	-0.06	0.005
6.5	5	50	-0.017	-0.031	0.009
6.5	5	500	-0.017	-0.030	0.005

Table 6.2. Measurement and analysis conditions for steam flow/pressure/power relations for three bandwidths.

Discussion of the NCR's. From Fig.6.3 it is obvious that the steam flow noise source is nearly completely intrinsic, i.e. not caused by fluctuations in pressure or power. Only at very low frequencies below 0.3Hz, a part is caused by power noise. For the neutron flux, the same holds at low frequencies. Only below 0.1 Hz some influence of the pressure noise is visible. At higher frequencies however (Fig.6.3c), it appears that steam flow fluctuations give a large contibution, up to 50%, in the frequency regions corresponding with the peaks in the steam flow spectrum and coherence lobes.
The pressure fluctuations are also mainly caused by steam flow noise below 5Hz.

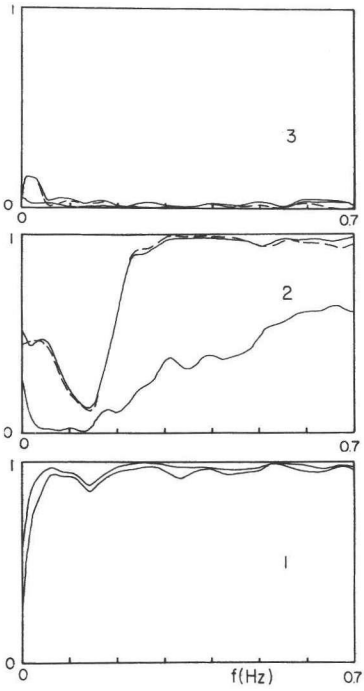

Fig.6.3a

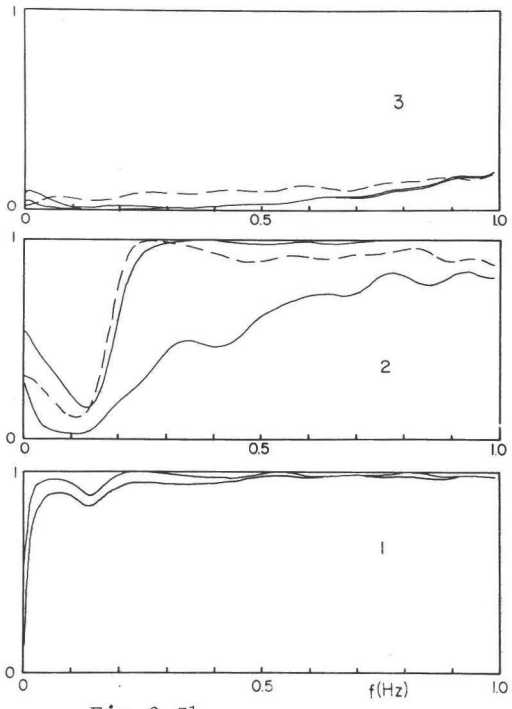

Fig.6.3b

Fig.6.3

Noise contribution ratios of steam flow (1), vessel pressure (2) and neutron flux (3) for three bandwidths:

a:0-0.5Hz (plotted to 0.7Hz)
b:0-1.0Hz
c:0-6.5Hz (plotted to 7.0Hz)

solid curves: complete identification
dashed curves: partial (2-3) identification.

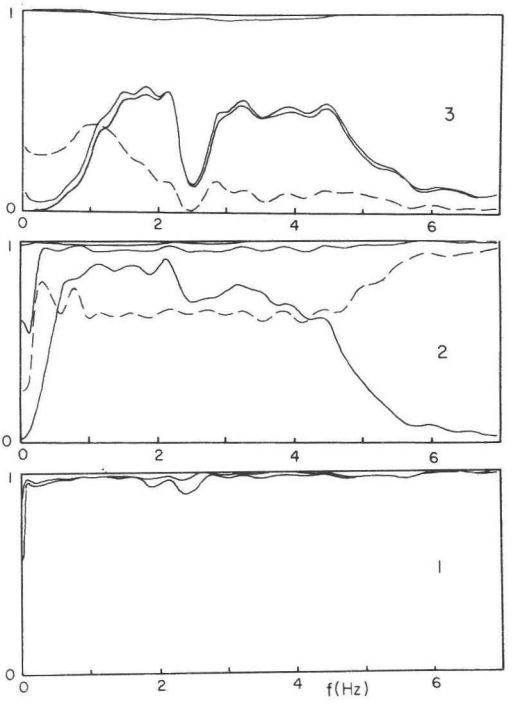

Fig.6.3c

Under 0.2Hz, the most important contributor is the power noise. Furthermore, some intrinsic pressure noise appears to exist, from 10% at 1-2Hz to 100% at 7Hz.

The physical processes causing these intrinsic noise sources can be understood for a large part. The low-frequency contribution of the intrinsic power noise can be found in the power fluctuations caused by reactivity noise, of which the boiling process is the dominant cause. Its contribution to the other signals is limited to low frequencies, due to the low pass filtering character of fuel heat capacity, vessel steam volume and pressure control system.

The intrinsic steam flow fluctuations are caused by two mechanisms. In the very low frequency region the pressure control system causes noise, as will be shown in Sect.6.4. At higher frequencies, autonomous flow fluctuations are caused by standing waves (acoustical oscillations) in the main steam line. Such low frequency oscillations are known to exist in large piping systems(6,7). A detailed analysis by van der Veer(8), based on the theoretical models of Ref.7, identifies several different oscillation modes with fundamental mode frequencies of 1.7, 1.8, 2.9, 3.5 and 5.2Hz. Many of these can clearly be observed in the NCR's and signal spectra.

For the intrinsic pressure noise, the situation is less clear. Pressure fluctuations will be caused by variations in either vessel steam volume or steam mass. Variations in these quantities, not being caused by steam flow and reactor power variations, seem impossible. Mass changes are either due to evaporation (power) or removal (steam flow) and thus modelled in these signals. Fluctuations in volume (except for evaporation) are not probable. Instrumentation noise was a second cause considered; it could be proven to be unimportant for frequencies up to 5Hz, by correlation of 1PT08 with a second, independent, pressure signal.

In the low frequency region, mainly below 0.5Hz, pressure fluctuations may be caused by power variations in fuel bundles outside the limited detector field--of-view, treated in Chapter 5. A second AR analysis was performed in the 0-0.5Hz region with three more neutron signals: incore HT and excores N5/N6/N7 which were considered to give, together, a sufficient picture of power fluctuations in the whole core. There was a small effect of this extension (the NCR of neutron noise to pressure signal increased by 0.1 below 0.2HZ) but it was not sufficient to remove all of the intrinsic pressure noise.

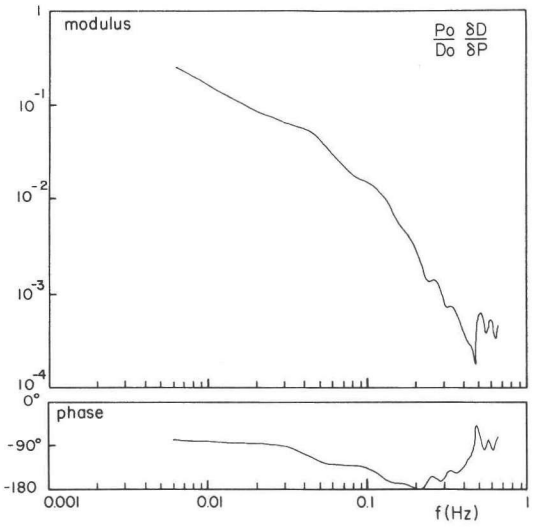

Fig.6.4a
Transfer function between power and vessel pressure from 0-0.5Hz analysis.

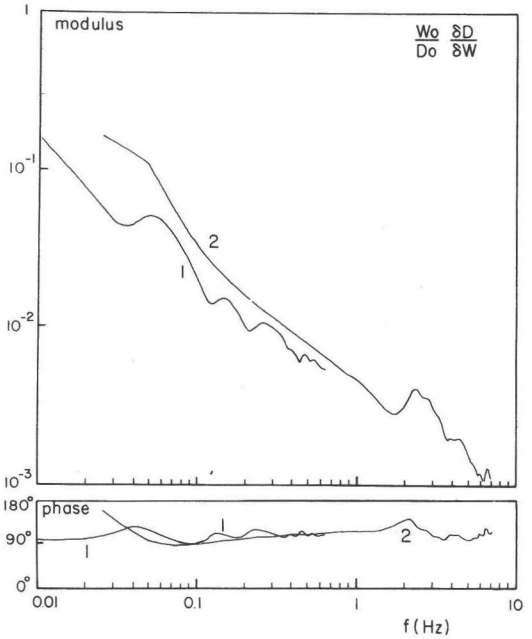

Fig.6.4b
Transfer function between steam flow and vessel pressure for 0-0.5Hz (1) and 0-6.5Hz analyses.

Discussion of the transfer functions. From the NCR's, it follows that transfer functions may be obtained from power to pressure and steam flow to pressure. Fig.6.4a shows the transfer function from power to pressure, which can be measured up to approximately 0.3Hz according to the NCR. At very low frequencies an 1/f slope with -90° phase difference is present, due to the integrating behaviour of the vessel volume for the produced steam. With increasing frequency, phase shift tends to -180° and the slope to $1/f^2$, due to the low pass filtering by fuel heat capacity. From the curve, an approximate effective fuel time constant of 1.6s can be estimated (break frequency of 0.1Hz), to be compared with a value 3.3s obtained in Appendix 3. The precision of the present estimate is however very limited; longer measuring times would be necessary to obtain a better accuracy.

Fig.6.4b represents the transfer function from steam flow to pressure for the analyses of 0-0.5Hz and 0-6.5Hz. The expected relation can be simply derived:

$$\frac{d}{dt}\,\delta M_s = V_{so}\frac{d}{dt}\delta\sigma_s = V_{so}\sigma_D\frac{d}{dt}\delta D = -\delta W_s \qquad (1)$$

which yields in frequency domain the (normalised) transfer function H_{DW}

$$H_{DW}(f) = \frac{W_{so}}{D_o}\,\frac{\delta D}{\delta W_s} = \frac{W_{so}}{2\pi V_{so}\sigma_D D_o}\cdot\frac{j}{f} \qquad (2)$$

where D is pressure, W_s steam flow, σ_D steam density, σ_D its pressure derivative, V_{so} the vessel steam volume, f frequency and j the imaginary unit. The 1/f behaviour and $+90^o$ phase shift are apparent. The strange phenomenon appears that below 2Hz the transfer function is given by approx. 4 $10^{-3}/f$, while above 2.5Hz 8 $10^{-3}/f$ holds. The effective volume estimated above 2.5Hz is $30m^3$ which is reasonable compared with $22.4m^3$ obtained in Appendix 3 from the vessel dimensions. At lower frequencies, apparently a larger effective volume of $60m^3$ is found. An explanation for this effect may be the fact that saturated steam is not an ideal gas: with steam mass content variations, evaporation or condensation will occur. The pressure variations are thus decreased and a larger effective volume is found. As these processes require some time they will affect mainly the low frequency region. More quantitative results would require a detailed analysis of the steam dynamics.
A correction for the value found above 2.5Hz should be applied due to the differences in transfer function of the steam flow and pressure sensor. Van der Veer(8) thus obtains an effective value of $27m^3$ instead of $30m^3$.

6.3.3. Partial identification. The expected model of the relation between steam flow, pressure and power, as given in Fig.5.9, indicates that a partial identification technique as discussed in Appendix 2, may give some more information on the transfer functions of pressure to power and pressure to steam flow. A second motivation for partial analyses is the requirement to remove pressure fluctuation effects from the power signal, necessary in Chapter 5. During these analyses some inconsistencies in the results appeared which will be mentioned here.
Partial identification is performed by considering only two signals from the three, e.g. power and pressure, while neglecting the third. Such a procedure is motivated by the lack of a direct transfer function between power and steam flow. For that case, the intrinsic steam flow noise source should be identified as part of the pressure noise source; the sum of the contributions of pressure and flow noise to power and pressure should remain unchanged. For the 2-3 combination, similar results are expected. If there is no physical pressure noise source, the partial analysis 1-3 should also remain unchanged. If some pressure noise is present, it will be distributed between the power and flow noise source.
This picture appears to be correct for the analysis in the band 0-0.5Hz, see Fig.6.3a. This is in contrast with the partial analysis pressure/power in the 0-6.5Hz band, which gives completely different results as compared with the trivariate analysis. Also case 2 (0-1.0Hz) already shows some discrepancies. The 1-2 and 1-3 partial analyses are correct.
The implication of this observation is that the partial analysis flux-pressure will not give the correct system model and the results can not be trusted to produce a correct elimination of pressure noise, as was pursued in Chapter 5.

Instead, a complete analysis including steam flow would be required. It is however probable that , due to the expected lack of the physical pressure noise source, the transfer function of pressure to power would even than be unmeasureable. Furthermore, from Table 6.2 it appears that under this condition substantially larger sampling rates would be required, thus larger model orders and more computer time.
The cause for the discrepancies is unclear. From the observations, it appears as if a direct transfer function is present between the flow signal and the power signal. How this would be physically achieved is not clear; one possibility would be an input contribution of power in the pressure controller but this is not present (unless parasitically). A further indication of such a direct relation between power and pressure is the remaining correlation between the noise sources 1-3 in the case 3 analysis which is a strange phenomenon. Transfer of information between the two via pressure would more likely give rise to increased correlation between 1-2 and 2-3 than between 1-3. More research is necessary to find the cause for this problem.

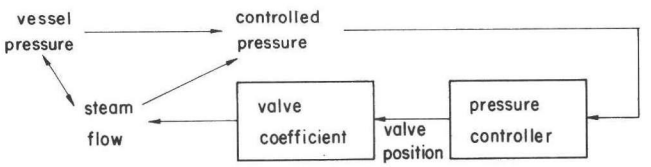

Fig.6.5
Signal relations for pressure control system analysis.

6.4.AR analysis of pressure controller.

A further picture of the noise sources in the reactor system and some important transfer functions can be obtained if the pressure control system is taken into the analysis (Fig.6.5). The vessel pressure is controlled by a control system for which the input signal is a pressure transducer on the main steam line near the turbine; the output signal is the position of two control valves that vary the steam flow from the vessel according to the pressure deviations. The input signal will be called the controlled pressure (to be distinguished from vessel pressure); as output signal the average of the two control valve positions is taken. Spectra are shown in Fig.6.6.
An AR analysis was performed in the region 0-0.5Hz of the same experiment as discussed in the previous paragraph, extended with controlled pressure and valve position signals. The resulting NCR's are given in Fig.6.7. It appears that the steam flow noise at low frequencies is mainly caused by noise in the control system. The origin of these noise sources may be instrumentation or detection noise for the controlled pressure signal and non-linearities in the

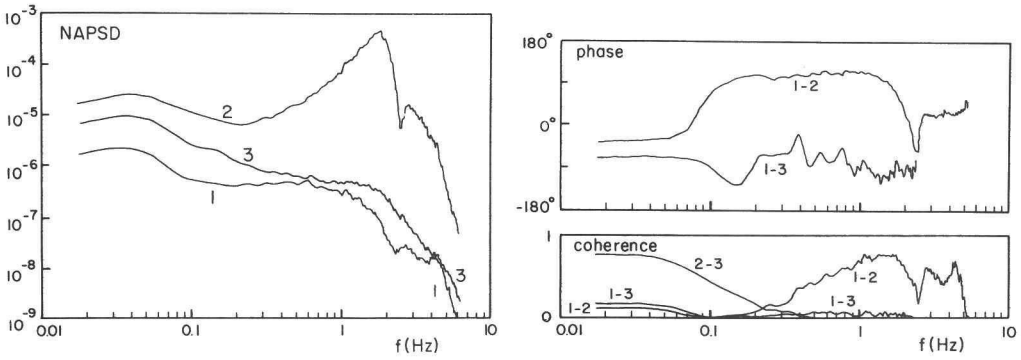

Fig.6.6
Spectra of controlled pressure (1), steam flow (2) and control valve position (3). Some phase and coherence relations are shown.

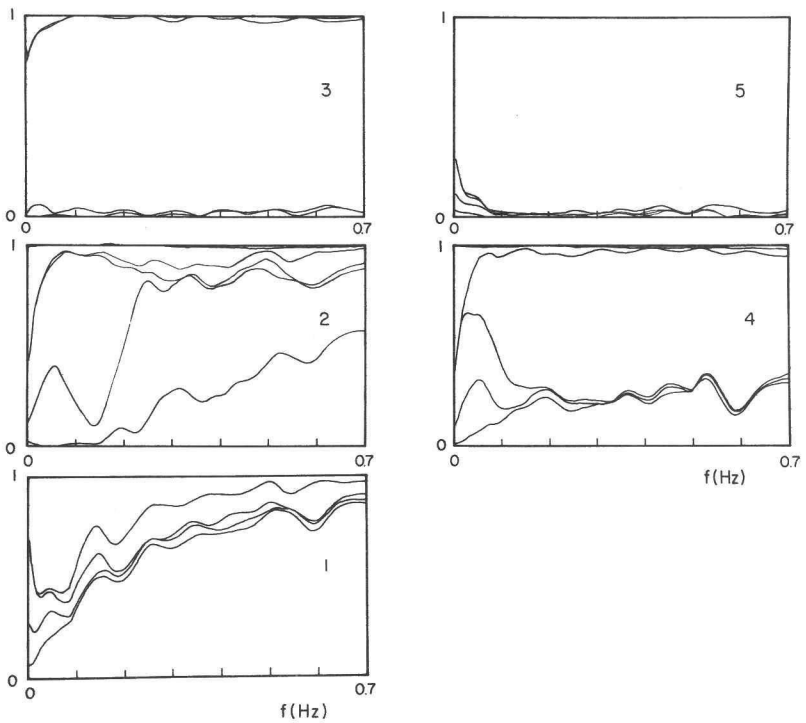

Fig.6.7
Noise contribution ratios of steam flow (1), vessel pressure (2), neutron flux (3), controlled pressure (4) and control valve position for 0-0.5Hz analysis.

control system plus instrumentation noise for the valve position signal. In the same way, the noise contribution of steam flow to pressure and power observed in Figs.6.3 stems from the controller. It is noteworthy that most of the noise in the valve position signal is intrinsic, which means that most of the pressure control action is autonomous and not caused as response to pressure deviations.

Partial analysis of controlled pressure with valve position may be expected to give the pressure controller behaviour. In the same way, partial analysis of the valve position-steam flow signals may give the valve coefficients (see Appendices 1 and 3). These points are motivated by the structure of the signal relations, shown in Fig.6.5: no crosslinks within the control path are present to disable a partial analysis. It appears that the NCR's found at the partial analyses are consistent with the complete system analysis, which justifies their results.

The transfer function from valve position to steam flow is not shown. A flat curve is obtained, with a statistical precision that decreases with frequency due to the decreasing contribution of valve position to flow. A value for the valve coefficient is obtained as 1.1±0.2.

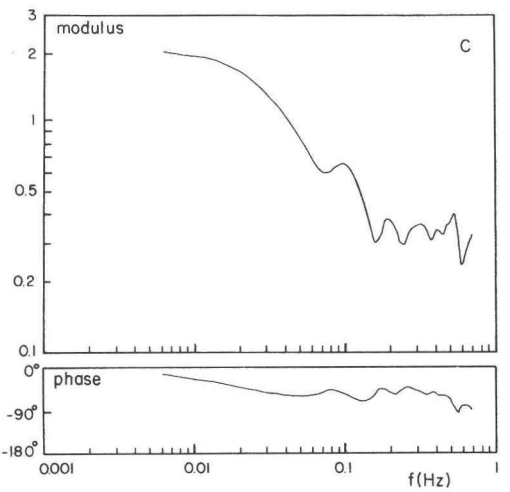

Fig.6.8
Pressure controller transfer function (controlled pressure to control valve position) at full power conditions.

The NCR's of all signals to valve position are too small to obtain a reasonable accurate estimate for the pressure controller transfer function at the conditions of EXP2 presently discussed. For the related noise measurements at full power (see also Appendix 1) it appeared possible to obtain an estimate, due to the different relative strengths of the applicable noise sources. Fig.6.8 gives the obtained controller transfer function (valve position variation to pressure variation ratio). Due to the nature of the NCR, only up to 0.2Hz some

precision is obtainable. The transfer function can be modelled as a first order filter with a gain of 2 and break freqency of 0.025Hz (time constant 6.4s). From the same experiment also the valve coefficient for this case was obtained; its value was 0.55±0.05. This value is lower than the one previously obtained due to the larger valve opening at the larger power, in combination with the very non-linear relation between flow and valve position discussed in Appendix 3.

6.References.

1. Fukunishi,K. Nucl.Sci.Eng.62,215-225,(1977).
2. Fukunishi,K. Nucl.Sci.Eng.67,296-308,(1978).
3. Fukunishi,K. J.Nucl.Sci.Techn.14,351-358,(1977).
4. Upadhyaya,B.R.,M.Kitamura and T.W.Kerlin. Ann.Nucl.Energy 7,1-11,(1980).
5. Kleiss,E.B.J. Report IRI-Int-131-82-03,(1982).
6. Christensen,H. Report KR-35,Vol3,ChapterVIII. Kjeller,Norway,(1962).
7. Selander,W.N and P.Y.Wong. Report AECL-6176,Chalk River,Canada,(1978).
8. Van der Veer,J.H.C. Progress in Nucl.Energy 9,607-618,(1982).

APPENDIX 1. THE CONTROL ROD EXPERIMENT.

A1.Abstract.

Two experiments were performed to measure the reactor transfer function (RTF). Reactivity variations were introduced by control rod movements: sequential insertions and withdrawals. The averaged response of several reactor signals (neutron flux, pressure, control valve position, steam flow) were obtained. The procedure to compute the RTF from these responses is discussed. Apart from the RTF, the void reactivity coefficient and pressure controller parameters could be estimated.

A1.1.Introduction.

In chapter 4 and 5 and Appendix 3 of the present thesis, the reactivity transfer function (RTF) of the Dodewaard reactor is obtained. The results are derived from (indirect) experiments via the space dependent noise characteristics of the neutron flux and from model calculations. Both methods are based on assumptions and approximations with a different degree of correctness. Although the results do agree, an independent determination of the RTF is welcome to validate the results. The method discussed in this appendix is a direct experimental determination of the RTF, based on controlled reactivity input and observed reactor response. The results are used as a check on the correctness of other methods in Chapter 5. The details of the experiment and some related results are discussed here.

Reactivity variations can be introduced in the core by means of the control variables for normal reactor operation. These are steam flow (pressure control system), feedwater flow (reactor water level controller) and control rod positions. The choice of the input actually used is rather straightforward. The feedwater control only affects the reactor power very slowly, with no direct coupling between flow or level and reactivity. For the steam flow, the introduced variations may be faster due to the relative fast response of the control valves. However, the reactivity is introduced by pressure buildup and is also

rather slow and indirect. Due to the desire to measure the RTF up to frequencies of 1 Hz or more, relatively fast reactivity introductions are necessary. Furthermore, steam and feedwater flow cannot be manipulated at will without modifications in reactor hardware.
The remaining input variable, control rod position, is well-suited for the present purpose. Reactivity is directly coupled to rod position and the reactivity worth of the rod may be quite large. Rod position variations may furthermore be introduced rather easily by operator manual action.
Some experimental problems arise. In the Dodewaard reactor rod position is not directly measurable, so only an estimate of the input signal can be obtained. The rod repositioning is a rather complex movement due to properties of the drive mechanism, with different shapes in the upward and downward directions. The time required for a complete step is several seconds which reduces the useful frequency content of the input. Finally, background noise is present, both as instrumental and as reactor noise. These points affect the accuracy but with the approaches discussed in this appendix useful results can be obtained.
The output signals from which the RTF is established are the signals of in- and ex-core neutron detectors. Due to the space dependence of the neutron flux variations, these responses are not completely equal; besides an estimate of the RTF, also a further picture of the power feedback effects is obtained in Chapter 5. Apart from power variations, the reactivity input generates variations in other variables as pressure and steam flow. The measured responses of these variables may be used to estimate other parameters of importance for reactor operation. Details will be discussed in the following sections.

A1.2. The input signal.

An important aspect of the experiment is the design of a suited input sequence of control rod movements. As the speed of the rods is limited, the frequency content of the input signal is concentrated at low frequencies. The accuracy of the obtained response and RTF is limited, being determined by the input signal (i.e. its spectrum), the noise spectrum and the time duration of the experiment. An optimisation can be obtained by choosing a suited input signal, within the limits set by reactor hardware and experimental boundary conditions. These are:

- small (local) power changes to preserve fuel integrity (reduction of thermal stress in the cladding),
- a simple scheme of rod movements as these have to be induced manually by the operator,
- a minimal waiting time between succesive steps of approximately one minute, also to reduce the chance of fuel failures.

The optimisation purpose can be considered as the maximisation of the high-frequency content of the input signal. This signal is shown schematically

in Fig.A1.1. The rod movement sequence can be regarded as the convolution of the elementary rod step z(t) and the impulse sequence p(t). Alternatively the convolution of rod velocity v(t) and the step function s(t) can be considered, which will be done here.

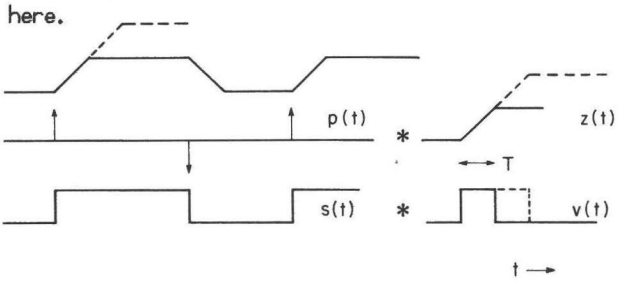

Fig.A1.1 Schematic control rod step, for two step durations, considered as convolution of p(t) and z(t) or s(t) and v(t).

The elementary step is determined by the control rod drive mechanism. A rod can be inserted or withdrawn from the core only over fixed distances given by discrete notch settings. The magnitude of the step (actually a ramp) is given by the number of notches involved in the step; the rod velocity is (approximately) constant. In Fig.A1.1 a step sequence with single and with double amplitude is shown. The spectrum of the input signal is given by the product of the spectrum of the velocity v(t) and that of the step sequence s(t), which can be discussed independently.

A simple calculation shows the spectrum S_{vv} of v(t) to be

$$S_{vv}(f) = T^2 \left[\frac{\sin \pi fT}{\pi fT}\right]^2 \qquad (1)$$

with T the step duration. For different values of T, S_{vv} is shown in Fig.A1.2. It will be clear that, although the total energy content increases with T, the smaller steps are advantageous at higher frequencies. For the present experiment steps of only one notch were preferred.

As far as the step function s(t) is considered, much freedom exists in the specific choice of the sequence, but within the limitation of a minimum step interval of one minute. The best accuracy is obtained with the maximum number of steps within the available time

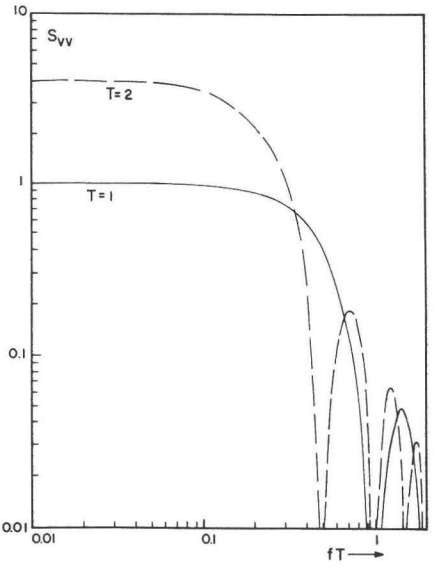

Fig.A1.2 Spectrum of v(t) for two step durations.

(as long as the inverse of the minimum analysed frequency is smaller than the step interval). This leads to a step sequence with a square wave shape, which is furthermore the most easy to be performed. A pseudo-random input sequence, that was also considered, would perturb both reactor and operator. It is also less efficient; due to the operational restrictions, fewer steps are made in the available time.

A second consideration is that the step response determination suffices, as the response to any random series of steps can be synthesised from the single step response. With several input steps available, the step responses can be averaged to increase the precision of the estimate.

Concluding, the input signal best suited within the experimental limits is a simple, regular sequence of single rod steps, alternately up and down, over one notch distance. The responses to each single step can be averaged to improve precision; then the step/impulse response and transfer function can be calculated. Details are given in A1.4.

Except for the choice of the rod step sequence, also the choice of the specific rod and its insertion depth (around which the 'oscillation' is performed) is of importance. It will be clear that the rod with the largest step reactivity worth gives the largest response and the most accurate results. The rod actually used is one of the central rods, the precise one determined by the rod pattern at the moment of the experiment (see A1.3).

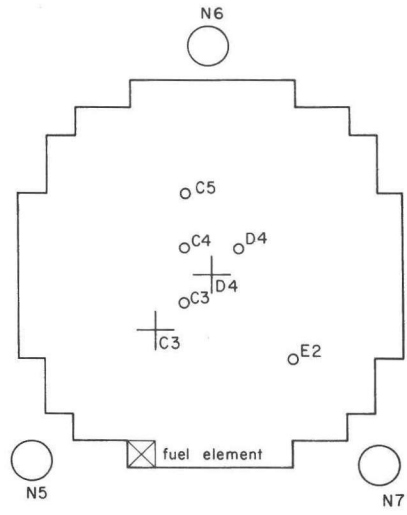

Fig. A1.3
Core top view with excore and incore detector positions and control rods used in the two experiments.

A1.3. Execution of the experiments.

Two separate control rod experiments were performed, on March 16,1981 (CRE1) and on January 6,1982 (CRE2), both at the very end of the fuel cycle just before the refuelling stop. The conditions were in general similar but some differences did exist: power level and the rod used. The reactor power level was decreased during the experiment, to reduce the absolute magnitude of the

	CRE1	CRE2
date	16/3/81	6/1/82
power(MW)	135	142
Rod positions		
(C3,C5,D3,D5)	4x15	4x19
(D4)	23	8
remaining	23	23
Selected Rod steps	C3,14/15	D4,8/9
Number of steps	50	104
Available signals		
incore AT	C4,60 cm	C5,108cm
incore HT	C3,60 cm	D4,108cm
incore ND1	E2,120cm	E2,120cm
incore ND2	-	E2, 60cm
excore N5/6/7	+	+
reactor pressure 1PT08	+	+
controlled pressure CP	-	+
steam flow 1FT25	+	+
valve position CVL/CVR	-/+	+/+
rod position relay CR	+	+
Signal filtering		
all	1.75Hz	
1FT25		1.0Hz
CP		15Hz
rest		-

Table A1.1. Experimental conditions at the two control rod experiments CRE1 and CRE2.

power step and thus the chance on fuel failure due to thermal stress. As the power level was reduced, only a limited time was available for the experiments due to economic reasons.
A number of rod steps (up and down counted separately) with an interval of approximalety one minute were executed and the response of several variables recorded: incore and excore neutron detectors, vessel pressure, controlled pressure, steam flow and valve positions. The control rod position is not directly measurable, only the presence at a specific notch position is detectable via relays; in this way the starting instant of the movement was observable. The precise rod movement can be reconstructed from the incore detector signals (see later this section). The choice of the rod was determined by the rod pattern at the end of the cycle; the rods in use for the full power control were inserted to reduce power and one was oscillated. Incore detectors were inserted at several radial positions to the same axial position as the rod tip. Figure A1.3 shows a top view of the core with rods and detectors indicated. Table A1.1 gives details on the conditions. Rod positions are indicated by notch positions: 00 is fully inserted and 23 is completely withdrawn. Position 15 and 8 are 57cm, resp. 112 cm from fuel bottom; the fuel length is 179 cm. The incore detector heights aren given in cm from fuel bottom.
After the response measurements, flux profiles were measured as input for the program TIPPEL. This program is the operator's program to determine flux-, power- and burnup-distributions of the core (5). The outputted data is used in the calculations of A1.4 and A1.5.

Calculation of the average responses. The recorded signals were sampled, after filtering under different conditions, and fed into a computer that determined the average of the response functions. From the rod relay signal, a pre-trigger signal was generated by a reverse playback/recording procedure. Using this signal for the start of an averaging cycle, the initial response was completely observable. The averaged responses were separately obtained for the insertion and withdrawal of the rod. 256 samples were taken from each response, with a sampling interval of 0.2s. The variations in the physical variables were normalised to their steady-state values so that relative responses are obtained. Results are given in Figs.A1.4-7 for the two experiments.
In the results of CRE2, the response of the steam flow signal (1FT25) is determined without and with filtering. This signal contains oscillations at 1.7 and 3Hz (Chapter 6), so the filtering clarifies the response signal. For the controlled pressure signal filtering was necessary due to a large component of approx.27Hz. For the other signals no filtering was necessary; the strong decrease of their spectrum with increasing frequency causes a neglectable aliasing under 1 Hz.

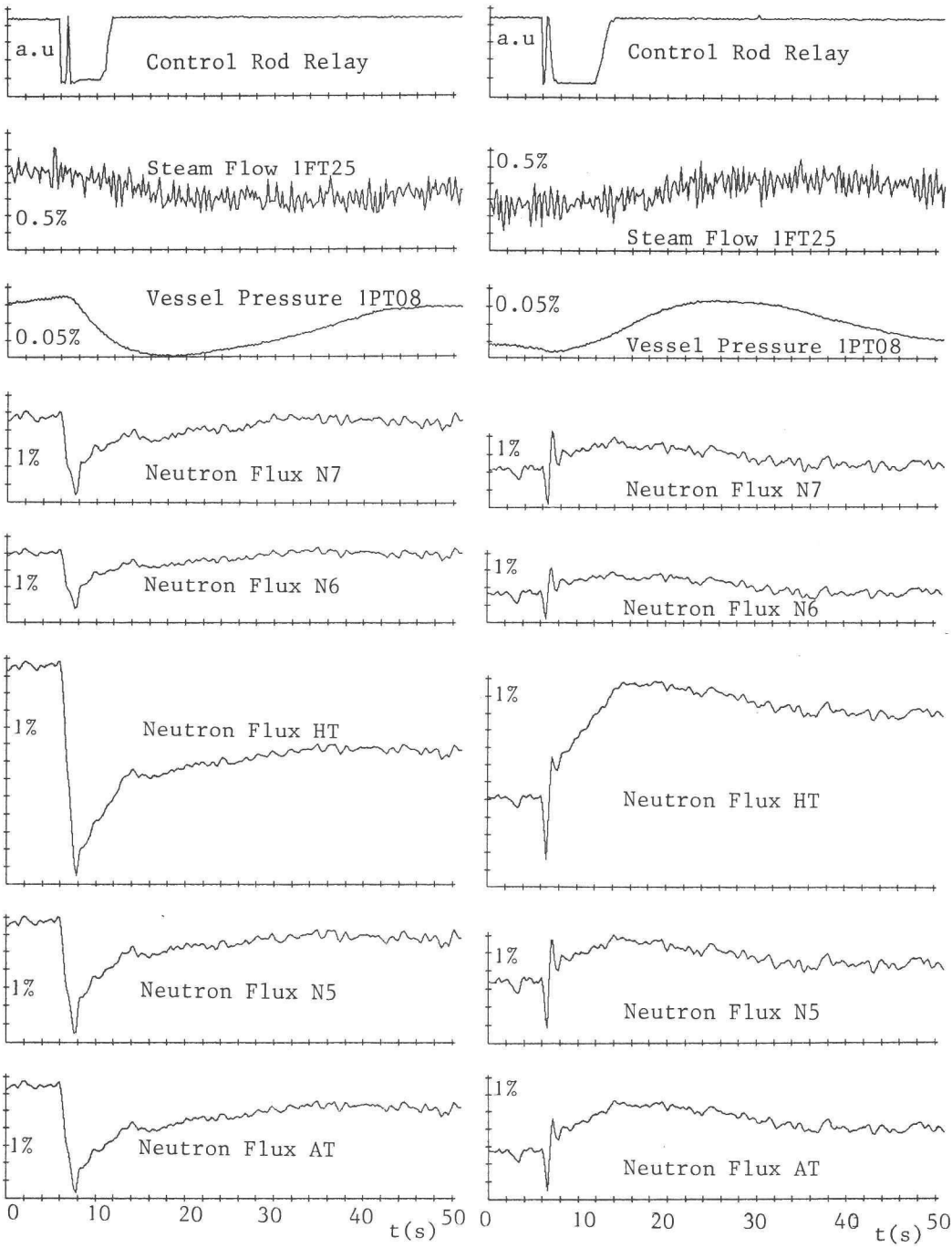

Fig.A1.4

Fig.A1.5

Normalised averaged responses of several signals at CRE1.
Left: rod insertion. Right: rod withdrawal.
Vertical scale division values are shown.

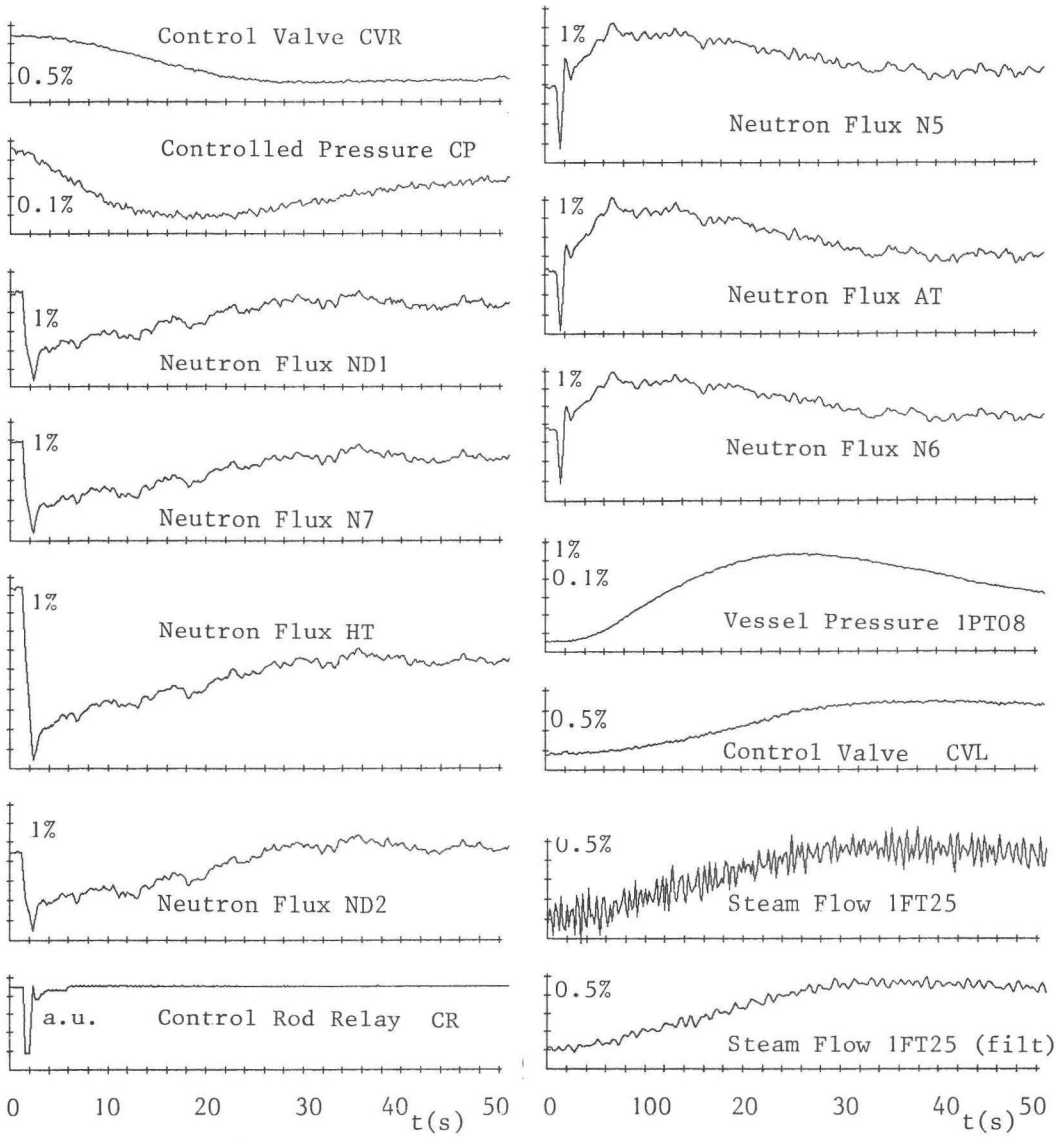

Fig.A1.6
Normalised averaged responses of signals at CRE2 at rod insertion.

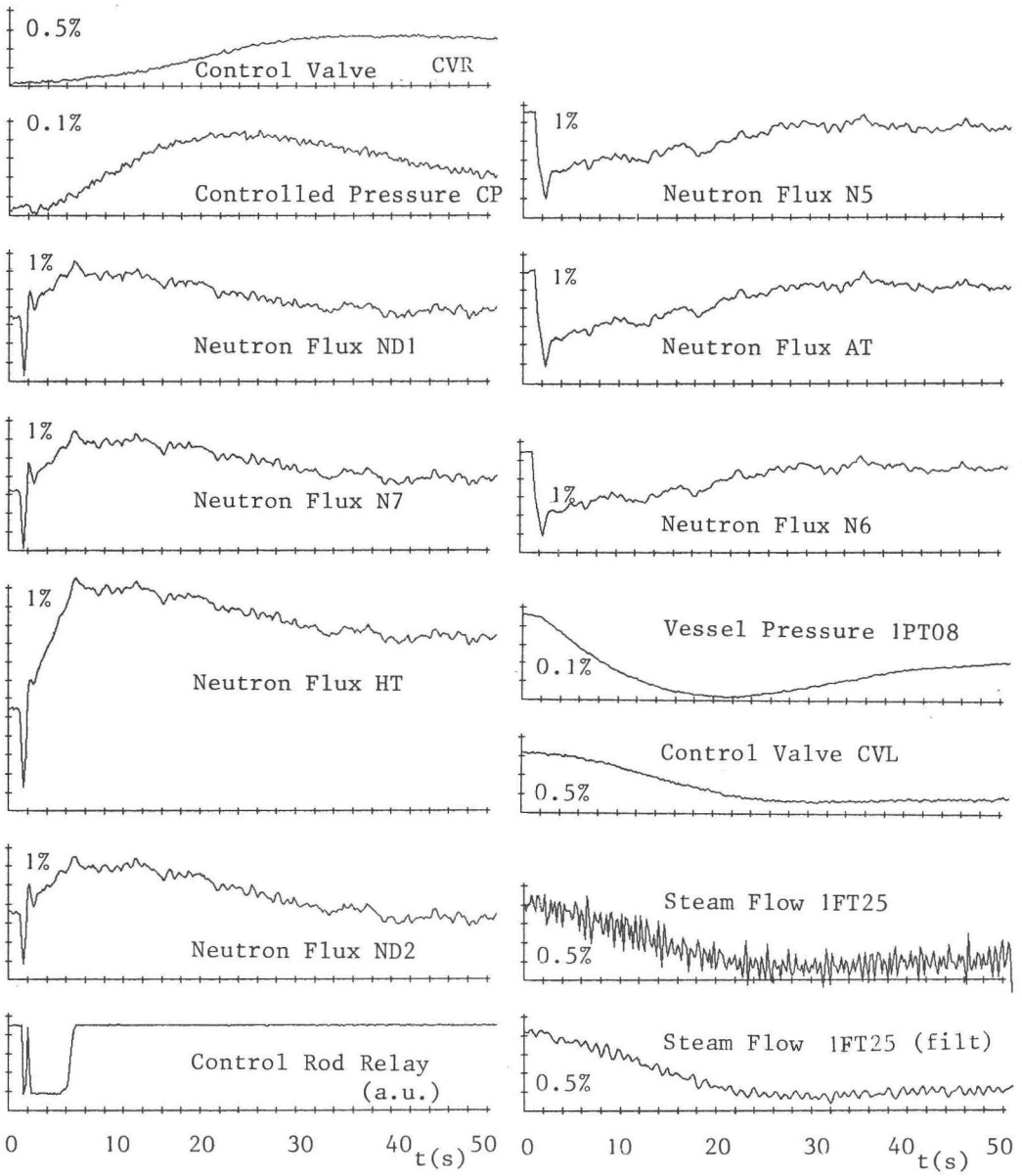

Fig.A1.7
Normalised averaged responses of signals at CRE2 at rod withdrawal.

There is a clear difference in the responses to rod insertion and withdrawal. This is due to the specific character of the rod movement. The insertions are rather fast, to a position above the final, after which the rod slowly settles down to its final position. At withdrawal, the rod is first lifted and than slowly sinks down do its new position (see the similarity of the CR signals in Fig.A1.4-7). For both experiments, a large overshoot compared with the steady-state change occurs in the neutron signals. This is due to the shapes of the rod movement and of the RTF. At CRE1, the responses are generally smaller than at CRE2 due to a smaller reactivity effect of the rod step. At CRE1 a substantial difference is seen in the responses of excore detecors N5/6/7 due to the excentric rod position (Fig.A1.3).

The response of the incore detector HT (closest to the rod) is larger than that of the other neutron detectors. This is due to the substantial local component in the response (flux depression associated with the rod movement). It is possible to use this effect to reconstruct the precise shape of the rod movement. If it is assumed that at the other incore detector positions (as AT) the flux depression is negligible, and that the reactivity-induced (global) response of the incore detectors is equal, the difference HT-AT is the pure local response of the detector. Assuming furthermore that the flux depression at HT is proportional to the insertion depth of the rod and its reactivity value, the reactivity input signal shape is thus available. Figure A1.8 shows the signal difference of HT and AT; note that a rod insertion means a flux decrease. It appears that the background noise is reduced, because this is correlated in the two detector signals (reactor power fluctuations). A rather good estimate remains.

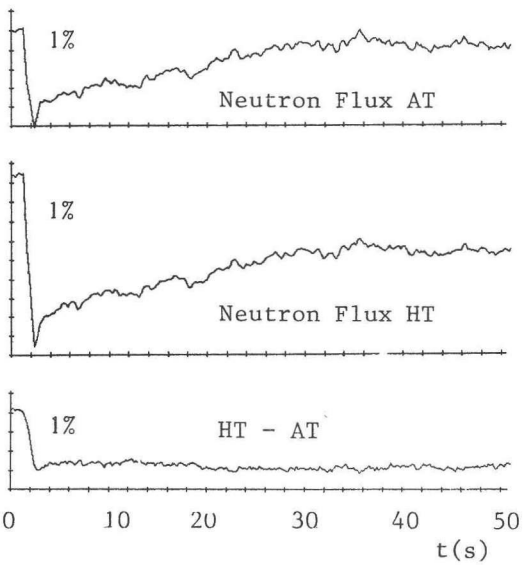

Fig.A1.8
Average response of HT and AT, the difference is used for the estimation of the control rod movement. Note that the rod insertion means a flux decrease.

A1.4.Estimation of the reactivity transfer function..

From the estimated reactivity input spectrum and the measured neutron flux response, the transfer function between reactivity and neutron flux (RTF) can be obtained. Also an estimate of the accuracy is possible by considering the background noise.

The RTF, here denoted by H(f), is in principle obtained easily by the division of the Fourier transforms I(f) and R(f) of the input and response signals i(t) and r(t):

$$H(f) = R(f)/I(f) \qquad (2)$$

Some complications arise due to the presence of background noise and the finite duration of the measured response signals, which will be discussed here. Due to the background noise, not the response function r(t) but its estimate $\hat{r}(t)$ is obtained. As a result also for R and H estimates are obtained: $\hat{R}$ and $\hat{H}$. Apart from that, spectral leakage effects occur due to the finite observation time (1). These leakage effects are specially important in the present case, as the spectra of input and of response strongly decrease with frequency. To reduce this effect, the signals $\hat{r}(t)$ and i(t) were pre-whitened, before Fourier transformation, by a numerical differentiation. In this way the effect of leakage is reduced. For the differentiated signal I'

$$I'(f) = \int_{T_1}^{T_2} e^{-2\pi jft} \frac{d}{dt} i(t)dt = \frac{1}{\Delta}\sum_k e^{-2\pi jfk\Delta}(i(k\Delta+\Delta)-i(k\Delta)) \qquad (3)$$

and a similar expression for the response $\hat{R}'(f)$. It will be assumed that in this way the bias on the estimate $\hat{H}$ due to spectral leakage is sufficiently reduced. The accents will be dropped in the following.

The observed response signal $\hat{r}(t)$ is contaminated with background (reactor) noise n(t):

$$\hat{r}(t) = r(t) + n(t) \qquad (4)$$

and for its Fourier transform

$$\hat{R}(f) = R(f) + N(f) \qquad (5)$$

As the noise on AT and HT is very strongly correlated, the noise on the input signal i(t) = HT(t)-AT(t) can be considered small with respect to the other errors present, and will be neglected. For the estimate $\hat{H}$ and its error δ it is found

$$\hat{H}(f) = \hat{R}(f)/I(f) = (R(f)+N(f))/I(f) = H(f)+N(f)/I(f) = H(f)+\delta(f) \qquad (6)$$

For the noise N(f), the expectation value is zero as no systematic deviations (dc signal) are assumed to be present. H, $\hat{H}$ and the error δ are shown schematically in Fig.A1.9 in a Nyquist diagram.

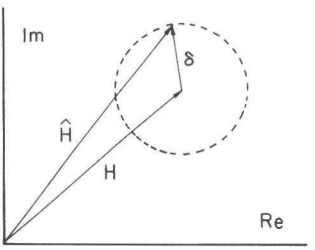

Fig.A1.9
Nyquist diagram of H, $\hat{H}$ and the error δ.

If the error δ is uncorrelated with H (or N is uncorrelated with R) and δ is furthermore gaussian, the probability density function of the error is a two-dimensional gaussian bell centred around H. For the estimate $\hat{H}$ holds:

$$\langle\hat{H}\rangle = \langle H+\delta\rangle = H+\langle\delta\rangle = H \qquad (7)$$

so the estimate seems to be unbiased. In practice however, not $\hat{H}$ but the estimate of the modulus $|\hat{H}|$ and of the phase $\hat{\varphi}$ are of importance. The statistics for these estimates are given without derivation, as

$$\langle|\hat{H}|^2\rangle = \langle(H+\delta)(H^*+\delta^*)\rangle = |H|^2 + \sigma^2(\delta) \qquad (8a)$$

$$\mathrm{var}(|H|^2) \approx \sigma^2(\delta)/2 \qquad (8b)$$

$$\langle\hat{\varphi}\rangle = \varphi = \mathrm{Re}(\hat{H})/\mathrm{Im}(\hat{H}) \qquad (8c)$$

$$\mathrm{var}(\hat{\varphi}) \approx \sigma^2(\delta)/2|H|^2 \qquad (8d)$$

where

$$\sigma^2(\delta) = \langle\delta\delta^*\rangle = \sigma^2(N)/|I|^2 \qquad (9)$$

and δ^* denotes the complex conjugate of δ, etc. It appears that the estimate of the modulus is biased and that the phase is obtained correctly. Once the properties of $\sigma^2(N)$, the error variance of the output signal, are known, a corrected (unbiased) estimate $\hat{H}'$ can be obtained:

$$|\hat{H}'|^2 = |\hat{H}|^2 - \sigma^2(N) \qquad (10a)$$

$$\mathrm{var}(|\hat{H}'|) \approx \tfrac{1}{2}\mathrm{var}(|\hat{H}'|^2)/|\hat{H}'| \qquad (10b)$$

The remaining problem is the determination of $\sigma^2(N)$:

$$\sigma^2(N) = \langle N(f)N^*(f)\rangle \tag{11}$$

with N(f) the Fourier transform of the differentiated noise signal n'(t):

$$N(f) = \int_0^T n'(t)e^{-2\pi jft}dt \tag{12}$$

The integration starts at zero because the input signal and the response are zero before that time; T is the observation time. Under the assumption that the autocorrelation function of n(t) is small after a lag T, it can be derived

$$\sigma^2(N) = 2\sigma_n^2/N_{avg} + 2\pi^2f^2TS_{nn}(f)/N_{avg} \tag{13}$$

where N_{avg} is the number of averages, $S_{nn}(f)$ the spectral density of the noise and σ_n^2 its variance. The properties of the noise are easily obtained by an analysis of the reactor noise measured after the response measurements. Eq.(13) can be interpreted rather straightforward. The error is dependent on noise spectrum S_{nn} as expected; the dependence on f^2 is due to the differentiation of the input signal or, alternatively, by the 1/f frequency content of the input step function. The observation time T is involved due to the fact that after a certain time no further information on the precise response is present in the signal and only noise is observed. This means that for an accurate result, the observation time T has to be chosen as small as possible. On the other hand, the mininimum of T is determined by the minimum frequency resolution required and the permissible bias due to the limited observation time as discussed earlier. From the Figs A1.4-7 it appears that the response is nearly finished after 10 seconds, except for a very low frequency component due to the pressure. The responses have been calculated with T=10s thus with a frequency resolution of 0.1 Hz.

An increase of precision is possible by the combination of the RTF's that were determined independently from the insertion and withdrawal measurements. From the two an estimate $\hat{H}_i$ with an error estimate σ_i (i=1,2) is obtained which can be combined using the inverse variances as weight factor w_i:

$$|\hat{H}| = (w_1|\hat{H}_1|+w_2|\hat{H}_2|)/(w_1+w_2) \tag{14a}$$

$$\sigma^2(\hat{H}) = 1/(w_1+w_2) \tag{14b}$$

Fig.A1.10 shows a result for CRE2, based on the response of N5. The error intervals represent one standard deviation. As can be seen, precision decreases with frequency. Further details of the results, including a comparison with the results from noise measurements and model calculations, are given in Chapter 5.

As the used signals (flux variations) were normalised to their steady-state

values, the units of the obtained RTF are relative: % output per % input. As a RTF should be based on reactivity input, the reactivity value of the input signal, thus of the rod step, is necessary. This is calculated in the next section; the result is used in Figure A1.10.

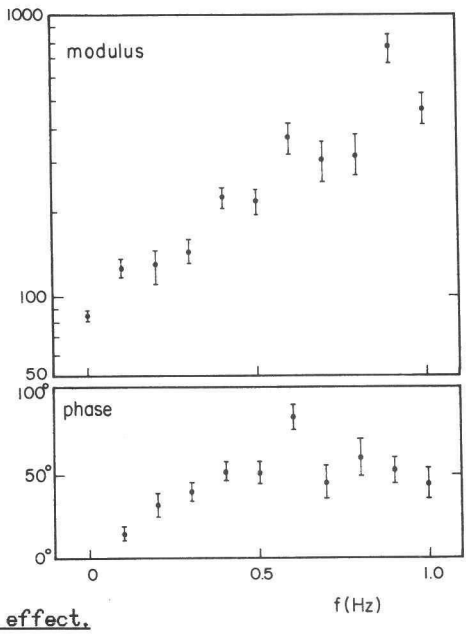

Fig.A1.10
Reactor Transfer Function estimated from the response of N5 at CRE2.

A1.5.Calculation of the rod step reactivity effect.

In this section the reactivity effect of the rod step is calculated. The effect is strongly dependent on rod position, rod pattern, burnup and power conditions and has to be estimated for every case separately. Here a simple approach is followed, based on the perturbation of the neutron balance by the change in neutron absorptions in the rod.

Consider a (one-dimensional) multiplying medium in which an unperturbed neutron flux ϕ_0 is present. The insertion of a flat control blade causes a flux depression due to the strong neutron absorption in the (black) surface. If a constant thermal neutron source due to moderation is present, the perturbed flux can be derived as (blade at x=0):

$$\phi(x) = \phi_0\left(1 - \frac{L}{2D+L} e^{-|x|/L}\right) \qquad (15)$$

where D and L are the thermal neutron diffusion coefficient and length. The absorption rate density J_{abs} in the blade appears to be

$$J_{abs} = \phi_0 \frac{D}{2D+L} \qquad (16)$$

Due to the flux depression, the amount of neutrons absorbed in the medium (A_{med}) is decreased:

$$\delta A_{med} = -\phi_0 \frac{D}{2D+L} = -J_{abs} \qquad (17)$$

which causes a decrease in the neutron production by fissions

$$\delta P_{med} = k_{inf} \delta A_{med} \qquad (18)$$

with k_{inf} the infinite multiplication factor. In total, the net number of neutrons effectively absorbed due to rod insertion is

$$\delta A = (J_{abs} + \delta A_{med} - \delta P_{med}) S_{eff} = \phi_0 k_{inf} \frac{D}{2D+L} S_{eff} \qquad (19)$$

Here S_{eff} is the effective absorbing surface of the control rod. The reactivity effect is obtained by comparison with the total number of neutrons absorbed or removed from the reactor:

$$\delta k = -\delta A / A_{tot} \qquad (20)$$

Because the reactor is critical, A_{tot} is equal to the total number of neutrons produced. This is the number of neutrons n yielded per fission times the total number of fissions, obtained by the reactor thermal power P_0 and the energy release per fission μ:

$$A_{tot} = P_{tot} = \frac{n}{\mu} P_0 \qquad (21)$$

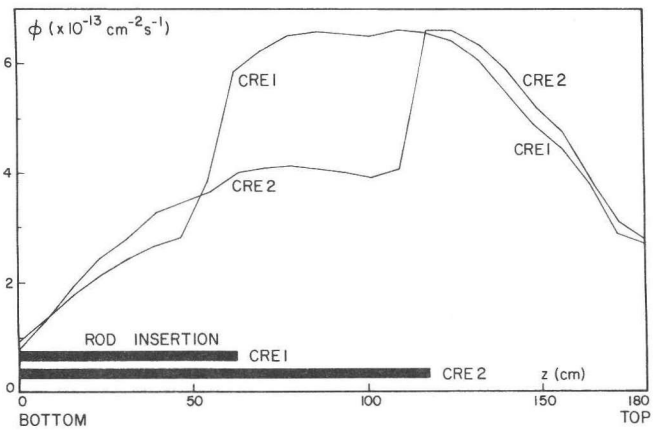

Fig.A1.11 Average axial neutron flux profiles at CRE1 and CRE2.

The parameters to be obtained for a specific experiment are thus D, L, S_{eff} and ϕ_0 at power P_0. The unperturbed flux ϕ_0 can be estimated from the power distribution obtained from flux profile measurements. Fig.A1.11 shows the axial profiles of the average flux in the bundles surrounding the control rod. ϕ_0 can easily be estimated from the region just above the rod tip. L and D are available from cross section calculations(4).

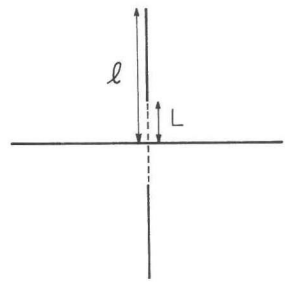

Fig.A1.12
Geometry for the estimation of control rod reactivity worth. Blade length ℓ and depressed flux length L are indicated.

The final quantity to be obtained is the effective rod surface S_{eff}. The rods are normal BWR crucifix-shaped blades. Due to the flux depression and the shadow effect of the perpendicular blades, not the whole rod surface can be accounted for. Considering the rod as composed of a whole blade and two side blades (Fig.A1.12), the effective length ℓ of the two side blades is reduced by L due to the flux depression caused by the first blade. For the effective rod surface S_{eff} it is then obtained

$$S_{eff} = 8d(\ell - L/2) \qquad (22)$$

d is the step size of the rod tip; the two surfaces of each blade are accounted for.
For CRE2, the following data were applicable: L=3.0cm, D=0.45cm, μ=195MeV=31pJ, P_0=142MW, ϕ_0=6.5 $10^{13}cm^{-2}s^{-1}$, k_{inf}=1.03, n=2.5, d=7.9cm and ℓ=8.25cm. The reactivity value of the rod step then appears to be -29 pcm. Furthermore a reactivity effect of approximately -1pcm is introduced by the removal of moderator at rod insertion, so that a total reactivity value of the rod step is obtained as δk=-30pcm. For CRE1, a value of -25pcm is obtained in this way.

A1.6.Estimation of the void reactivity coefficient.

The results of the CRE can be used to estimate the void reactivity coefficient ρ_α of the reactor. If temperature effects are neglected, the negative reactivity introduced by rod insertion will be balanced by the positive reactivity effect of void decrease due to the reduced power:

$$\delta\rho_{cr} + \rho_\alpha \delta\alpha = 0 \qquad (23)$$

As the control rod reactivity worth $\delta\rho_{cr}$ is obtained in the previous section, the estimation of the void fraction variation $\delta\alpha$ remains. This can e.g. be done with the use of the reactor model derived in Appendix 3. From

Eqs.(A3.7)-(A3.15) it can be derived that, at constant pressure, the void fraction is proportional to power:

$$\delta\alpha/\alpha_0 = \delta P/P_0 \qquad (24)$$

This will be commented later. The power variations due to the rod insertion are rather easily obtained. Two different estimates are possible.
The first is the power change due to the total rod insertion before the execution of the CRE (for CRE2 : rod D4 23→08 with an associated power decrease of 164MW→142MW). The reactivity worth of the rod insertion can be estimated as in the previous section and amounts -400 pcm. Assuming an average void fraction of 35% at full power, a reactivity coefficient is obtained of -0.085. The precision of this estimate is mainly limited by the accuracy of the rod reactivity value, and the assumptions on which Eq.(24) is based, for the calculation of $\delta\alpha$ for the large power variation of 22MW.
A second estimate is based on the averaged responses of the power (neutron flux). From Figs.A1.6-7 the steady-state power step is estimated as 0.8%, with an associated $\delta\alpha$ of -0.0024. The rod reactivity of -30pcm yields a reactivity coefficient ρ_α=-0.12. The main inaccuracies in this estimate lie in the steady-state power change, which is not precisely estimated as the pressure response does not reach its steady-state value. Furthermore, the total power variation will be larger than indicated by the ex-core detectors due to the in-core power feedback effects discussed in Chapter 5.
Some general comments to the present analysis have to be added. First, the reactivity worth of the rod has been calculated with a very simple model, based on diffusion theory in the vicinity of a black absorber and with no accounting for the differences in neutron importance in the different core regions. This limits the precision of the reactivity estimate. Furthermore, the proportionality between power and void fraction is not strictly correct. A more detailed analysis of the thermohydraulics(2,3) shows that a better approximation of the void fraction variations with power (under the operating conditions) is given by $\delta\alpha/\alpha_0=0.6\delta P/P_0$ so that $\delta\alpha$ is overestimated. The effects discussed here will partially cancel each other, which improves the estimate. This is illustrated by the fact that ρ_α, based on cross section calculations is -0.093 (Appendix 3), which is in good agreement.

A1.7.Pressure controller parameters.

Besides power variations, the control rod step also causes changes in reactor pressure (D) and pressure control variables (Controlled pressure CP, valve position x and steam flow W_s). For a description of the pressure controller see Appendix 3. From Figs.A1.6-7 the steady-state response of the signals can be obtained for CRE2. The variations of pressure and valve position are cor-

rectly measured; for the steam flow measurement a correction has to be applied. The steam mass flow W_s is measured as a pressure drop over a venturi restriction in the main steam line. For the flow signal s holds

$$s = \frac{C}{\rho_s} W_s^2 \tag{25}$$

and for the normalised fluctuations

$$\frac{\delta s}{2s_0} = \frac{\delta W_s}{W_{s0}} - \frac{\delta \sigma_s}{2\sigma_{s0}} = \frac{\delta W_s}{W_{s0}} - \frac{\delta D}{2D_0} \tag{26}$$

which enables the elimination of pressure-induced signal variations. Table A1.2 gives measured values at t=35s from which several controller parameters can be estimated.

Reactor pressure 1PT08	0.35%
Valve position (CVL/R)	1.25%
Steam flow signal1FT25	1.75%
Steam flow	1.6 %
Valve Coefficient K_c	1.0

Table A1.2
Pressure control variable variations at CRE2.

Valve coefficient. Due to the non-linear dependence of the steam flow of the valve opening, the valve coefficient K_c is dependent on the operating conditions of the reactor. K_c is defined as the relative variation in steam flow due to the variation in valve opening. It can be obtained rather easily from the measured values in table A1.1. The steam flow variation is 1.6% at a valve opening variation of 1.25%. Considering a flow variation of 0.35% due to natural control (see App.3) a valve coefficient of 1.0 is obtained for the reactor conditions at CRE2.

Controller transfer function. From the response functions it can be seen that the valve position response and the controlled pressure response do not have the same shape; this is due to the filtering of the pressure signal to reduce the high frequency content in the controller signals. The filter transfer function $H_f(s)$ has the form (Appendix 3)

$$H_f(s) = CP_0 \frac{\delta x}{\delta CP} = A(1+s\tau_{c1})/(1+s\tau_{c2}) \tag{27}$$

This function can be fitted to the observed responses to find the parameters in the present experiment. Some trials showed that the time constant τ_{c1} is so

small, in combination with the low frequency content of the CP signal, that it could not be estimated with any reasonable accuracy from the available data. Instead, a transfer function

$$H_f(s) = \frac{A}{1+s\tau_c} \tag{28}$$

was fitted.The actual fit was performed in time domain, of the time-domain equivalent of Eq.(28):

$$\delta x + \tau_c \frac{d}{dt}\delta x = A\frac{\delta CP}{CP_0} \tag{29}$$

A least squares fit of this equation to the measured response functions was performed. As the input signal CP was noisy, both in- and output signals were smoothed by a moving-average procedure. The parameter estimates appeared to be dependent of the smoothing length T_s which was varied. Results are given in table A1.3 for the estimates from the separate insertion and withdrawal responses. The overall estimates for the controller parameters are: A=4.5±1 and τ_c=13±3s.

T_s(s)	Rod in		Rod out	
	A	τ_c(s)	A	τ_c(s)
0.6	4.2	7.4	3.5	4.4
1.0	4.4	9.9	4.0	9.5
2.2	4.9	13.9	4.5	14.0
4.2	5.0	15.2	4.6	15.6

Table A1.3 Pressure controller parameters fitted from the averaged responses at CRE2.

A1.References.

1. Bendat,J.S. and A.G.Piersol. Random Data, Wiley-Interscience, New York (1971).
2. Kleiss,E.B.J. Unpublished results (1983).
3. Thermohydraulics design report. J.Hoekstra, private communication.
4. Oosterkamp,W.J. Private communication (1982).
5. Hoekstra,J. Private communication (1982).

APPENDIX 2. THE AUTOREGRESSIVE MODELLING OF NOISE SIGNALS.

A2.Abstract.

This appendix deals with the application of the multivariate autoregressive modelling to the output signals of a noisy system. A description is given of the method to obtain the noise sources and open- and closed-loop transfer functions within the system. The conditions are discussed under which the identified system yields meaningful results.

The first main conclusion is that the frequency at which the signals are sampled must be sufficiently high, generally larger than given by the Nyquist criterion. Only under this condition the noise contribution ratios and the transfer functions can be estimated correctly. The second main conclusion is that the transfer function can only be estimated correctly if all signals have sufficient interaction and contain sufficient intrinsic noise. This can be checked using the identified NCR's. If for certain frequencies the noise source lacks, only part of the transfer functions can be obtained.

Under these conditions the AR modelling is rather well applicable and gives useful results. This is demonstrated by several examples of analyses of known networks. The results agree with theory.

A2.1 Introduction.

In this appendix we shall deal with the problem to obtain information on a system from the (noise) signals being output of that system. This means that we try to develop a method to determine the driving sources of the observed noise and the transfer functions via which the signals interact. This is a general problem of system identification, for which several tools have been developed in the last decades. In this introduction we shall discuss the main lines and ideas of our interpretation of the use of the (multivariate) autoregressive model for the description of the reactor system and the analyses of its dynamic behaviour from the measured noise signals[1].

1) Most ideas that have condensed into the present text will not explicitly be referred to. They have been taken mainly from Refs. 1-6,11,12 where an abundance of information is present on the different topics.

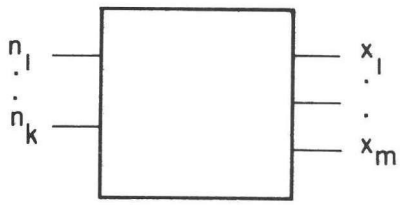

Fig.A2.1
General system with multiple noise inputs and multiple outputs.

Consider a black-box representation of a very general (but linear, time-invariant) system shown in Fig.A2.1. The system output variables $\{x_1, \ldots, x_m\}$ are measured as a function of time. The signals fluctuate due to the noise sources $\{n_1, \ldots, n_k\}$; These may be either inherent fluctuations in the physical process, or externally applied perturbations. If all noise sources were observable the system could easily be described by their characteristics (spectra, amplitude probability density functions, etc.) and by the transfer functions that can be measured between the noise inputs and outputs by standard correlation techniques.

In practice, when a noise experiment is performed on a reactor (or any other) system this ideal situation is seldom present. Some of the noise sources may be unobservable, as there is no way of direct measurement (such as reactivity for a nuclear reactor), or no signal is available. Also the situation occurs that an observed signal directly includes one noise source, but is also influenced by the other output signals so that a closed-loop situation exists. In such cases there is no simple way of input-output analysis and other methods have to be developed. One such approach is described in the following.

The first step taken is to assign more detail to the black-box of Fig.A2.1. In Fig.A2.2 a structure is assigned to the system in which every output x_i is driven by its own intrinsic noise n_i and by fluctuations in the other variables $\{x_j\}$ via open-loop transfer functions H_{ij}.

It is even possible, without loss of generality, to assume the physical noise sources n_i to be caused by hypothetical white noise sources w_i via a shaping filter H_{ii}.The character of this shaping filter is of course determined by the physical properties of the process. (A vibrating control rod has certainly no white spectrum but can be modelled so with a peaked shaping filter). The problem of system identification now comes down to the determination of the shaping filters, the open-loop transfer functions and the (cross-)spectra of the noise sources. Note that for variables fluctuating due to the same physical noise source (such as reactivity for neutron detectors, vessel pressure for independent pressure sensors), this proposed model is valid if we only allow for correlated (but still white) noise sources w_i.

Considering the proposed model, the problem is to find ways to determine from the observed outputs $\{x_i\}$ the unknowns H_{ij} and $|H_{ii}|$ (the phase behaviour of H_{ii} does not influence the system). These can be found but not in a very

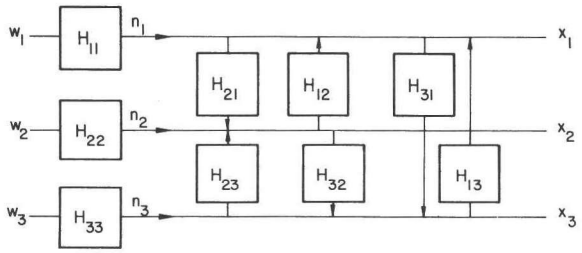

Fig.A2.2
General system with shaping filters for the noise inputs and transfer functions between the variables.

straightforward way, as can be seen as follows. The basic data from which to determine the unknowns are the (cross)spectra of the outputs or related quantities as correlation functions. For a m-dimensional system (m observed outputs) the number of knowns (real quantities) is then m^2: $m(m-1)/2$ cross spectra (modulus and phase) and m autospectra. The unknows that have to be determined are the moduli and phases of the H_{ij} ($2m(m-1)$) plus the m moduli of H_{ii}. The spectra of w_i can be given any value by adjusting H_{ii}. It is easily seen that we have too many unknowns to uniquely identify the system. The conclusion is that the number of unknows has to be decreased in some way; we cannot obtain more knowns from the observed signals for a given case. The reduction can be achieved in two ways.

The first way is to use more a-priori information of the system structure, such as knowledge on some transfer functions . This is e.g. done when identifying a system under closed-loop control when the controller behaviour is known. Another example is given in Ref.7.

A different but very fruitful approach, which is applicable without any loss of generality is the use of the causality property of physical systems. It will be clear that any physically realizable system will not respond to an input signal before that signal is applied. True predictors do not exist. We will call this the causality property and it appears to have important implications on the transfer function of the system (8): its real and imaginary part, or its phase and modulus, become related and cannot be chosen independently. In time domain it means that the cross-correlation function between two signals x_1 and x_2 is determined by the impulse response h_{12} of x_1 to x_2 on its left half (negative lag) and by h_{21} on it's right half (positive lag). This fact can thus be used to reduce the number of unknowns to exactly m^2 and then the identification is, in principle, possible.

The next problem is to find an efficient way to implement the causality property into the fitting procedure. First of all, it can be seen that it is more easy to perform the fitting in time domain, rather than in frequency domain. In frequency domain the relations between the modulus and phase are quite difficultly manageable integrals, while in time domain simply a response has to be zero before time zero. Of course, the results from the time domain fit can be used to obtain frequency domain quantities as transfer functions and spectra and this will generally be preferred for sake of clarity.
In the next section we will discuss the time domain modelling of the system and the merits of the autoregressive model chosen to perform this task. In the later sections some problems and limitations, both practical and theoretical, will be dicussed and then a section is presented in which a demonstration of the fitting on simple networks is performed.

A2.2. Time series modelling.

A2.2.1. Discrete time, parametric models. In this section several available methods to model the dynamic behaviour of a signal will be discussed. This signal is observed in time and the succesive values form a time series. For this time series a model is developed that describes, as close as possible, the characteristics (spectrum, correlation function) of the time series. Many different models are possible and which one is best suited depends on the specific application. There is a choice between continuous-time and discrete-time, parametric and non-parametric models with a large amount of subclasses. Starting with a discussion of univariate time series, a sensible model is found which can later be extended to the multivariate case.
The observed signals from which information on the system is to be extracted, are generally continuous functions of time. Most data processing methods, using digital computers, require discrete time data. Sampling the signal $x(t)$ with a sampling interval Δ at time instants $n.\Delta$ gives the discrete time series x_n. The Nyquist criterion shows that all information on $x(t)$ is preserved in x_n if the Δ is chosen sufficiently small. It will be clear that the models to be applied under these conditions are discrete-time models (to be distinguished from continuous-time models as differential equations).
When a model has to be established for a filter that generates the observed time series from white noise, or for a filter where output as well as input are measured, two different approaches are possible. The first obtains the filter impulse response by the deconvolution of input and output correlation functions or cross-correlation functions. In frequency domain the transfer function is obtained from the ratio of the spectra of output- and input-signals. The result is an impulse response function or transfer function that is obtained on a point-by-point basis. For every frequency or every time point a value is

found, independent of the values found for other points. The number of points is limited by observation length of the signal (spectral resolution) and sampling time (bandwidth), but in principle an infinite number of points is necessary to give a complete description of the filter. This approach is called non-parametric.

A different approach, called the parametric one, is based on the fact that the behaviour of the system is governed by a differential equation with, for practical cases, a limited order and number of coefficients. For discrete-time a difference equation is applicable. If we can estimate the parameters of the differential or difference equation from the observed time series, we obtain an accurate model with only a limited number of parameters.

Both approaches have advantages and disadvantages. The nonparametric models are relatively easy determined as discussed before. The disadvantage is the involvement of many independent points.

For the parametric models the model parameters are often closely related to the physical parameters in the system (such as time constants). A second advantage is that a limited number of parameters has to be estimated from many datapoints, so the statistical precision may be better. The mathematical operations necessary for a model fit are however more complex; often least-squares fits have to be performed. With modern computers and the availability of efficient algorithms the weight of this argument is reduced and the parametric models have become quite popular in time series analysis.

The relation between the two methods may be clarified by the following example. Suppose measurements have been performed on a system composed of a simple lag (first order low-pass filter). The non-parametric representation of the impulse response would be the set $\{h_0,h_1,\ldots,h_k,\ldots\}$ where h_k is the impulse response at time $k.\Delta$; in frequency domain it would be given by the set $\{H(0),H(f_1),H(f_2),\ldots\}$ with $H(f_k)$ being the transfer function at frequency f_k. The parametric model is the set $\{A,\tau\}$ from the differential equation

$$x(t) + \tau \frac{d}{dt} x(t) = A\, n(t) \qquad (1)$$

Of course the relation holds

$$h_k = \frac{A}{\tau} \exp(-k\Delta/\tau) \qquad (2)$$

and

$$H(f) = A/(1+2\pi j f\tau) \qquad (3)$$

A2.2.2 AR/MA models. Once it is decided to use a discrete-time, parametric model several possibilities arise. Three specific types of models have been developed that have proven to be very fruitful: the autoregressive (AR) models, the moving-average (MA) models and the mixed-mode ARMA models.

In the autoregressive model, the output x_t is given as a linear combination of its previous values and the input noise n_t:

$$x_t = \sum_{i=1}^{p} a_i x_{t-i} + n_t \qquad (4)$$

In the moving-average model the output is considered as a linear combination of previous values of the input signal:

$$x_t = \sum_{i=0}^{q} b_i n_{t-i} \qquad (5)$$

A third possibility is the mixed-mode ARMA process:

$$x_t = \sum_{i=1}^{p} a_i x_{t-i} + \sum_{i=0}^{q} b_i n_{t-i} \qquad (6)$$

In these relations a_i and b_i are the model parameters and p and q the model order, resp. It can be shown that if p or q is chosen sufficiently large, the time series can be modelled with a white noise source n_t. This can be interpreted as using all degrees of freedom allowed by the model order to build a shaping filter that generates the output spectrum from a white noise sequence. The AR model can be considered as a predicting filter; n_t is then to be considered as the difference between the observed and the predicted value of x_t:

$$n_t = x_t - \sum_{i=1}^{p} a_i x_{t-i} \qquad (7)$$

This point of view is used in the discussion of optimum model order in Sect.A2.3.

It is interesting to go deeper into the nature of the relations and differences of the three process types. One difference is clear when it is considered how information propagates in the model, or in other words, in which measure an amount of noise n_t is still present in x_{t+k}. It will be clear that in the MA process all contribution is lost after a delay q; the autocorrelation function of the MA process is zero after lag q. For the AR process, the information on n_t is transferred in every time step so never completely lost although it fades away in a stable system. The autocorrelation function will be asymptotically zero. Although this property accentuates the difference, the processes are related. Applying a z-transform to Eqs. (4) and (5), we obtain:

$$X(z) = \frac{1}{1+\Sigma_i a_i z^i} N(z) \qquad (8)$$

and

$$X(z) = (b_0+\Sigma_i b_i z^i)\, N(z) \qquad (9)$$

Relations (8) and (9) can be transformed into each other by a Taylor series expansion. This implies that the MA process can be replaced by an AR model of infinite order, or at least approximated by a finite order AR model; the reverse holds for an AR model. The conclusion is that a large freedom exists in choosing a model structure for a specific identification task. One should bear in mind, however, that not all models have the same efficiency in the sense of the minimum number of parameters required. From this point of view it may be clear that the mixed-mode ARMA model is generally the most advantageous. But there are important differences in the ease of the model estimation for the different models from the observed time series. Define the correlation function of the signal x as:

$$\phi_k = < x_t x_{t+k} > \qquad (10)$$

For the correlation function of the AR series the Yule-Walker equation holds:

$$\phi_k = \Sigma_{i=1}^{p} a_i \phi_{k-i} \qquad (k>0) \qquad (11a)$$

$$\phi_k = \Sigma_{i=1}^{p} a_i \phi_{k-i} + \sigma^2 \qquad (k=0) \qquad (11b)$$

where σ^2 is the variance of the noise source n_t. Apparently an autoregression scheme holds for the correlation function, too. It may be noted that this relation holds thanks to the causality of the AR series (4).
Starting with the estimation of the correlation function ϕ_k from the observed signal, the estimates for $\{a_i, i=1,..,p\}$ and σ^2 can be obtained by solving the linear Yule-Walker equation straightforwardly. Efficient recursive algorithms (estimation of the model for successively increasing model orders) have been developed (9). For the MA and ARMA models, the correlation functions obey less simple relations than Eq.(11) and generally non-linear equations have to be solved for the determination of the model parameters(1,2). This is the reason that AR models are often preferred although ARMA or MA models might be more efficient. This last point is enhanced by the fact that a continuous-time system, governed by a differential equation:

$$\Sigma_{i=1}^{p} c_i \left(\frac{d}{dt}\right)^i x(t) + c_0 x(t) = n(t) \qquad (12a)$$

yields, after sampling, a discrete ARMA difference equation:

$$x_t + \Sigma_{i=1}^{p} a_i x_{t-i} = \Sigma_{i=0}^{p-1} b_i n_{t-i} \qquad (12b)$$

Due to the simplicity of the AR process and the fact that it can describe the system sufficiently close, the inefficiency is accepted and all following work will be based on autoregressive models.

A2.2.3. The multivariate AR model. In the case that more than one signal is observed the theory has to be extended to derive the multivariate equivalents of the relations obtained in the previous section. Referring back to the system structure of Fig.A2.2, we can propose a multivariate autoregressive (MAR) model to fit the time series $\underline{x}_t$, where $\underline{x}_t$ is a m-dimensional vector of the observed variables $x_l(t')$ at $t'=t\Delta$; $l=1,\ldots,m$. The model is:

$$\underline{x}_t = \Sigma_{i=1}^{p} A_i \underline{x}_{t-i} + \underline{n}_t \qquad (13)$$

Here $\underline{n}_t$ is a m-dimensional noise source vector and A_i are matrices that model the relations between the signals x_l. Sometimes $\underline{n}_t$ is called the residual noise source, and its components n_l form the intrinsic noise sources in the signals x_l. If the model order p is sufficiently large, the residual noise is white with a noise source covariance matrix Σ:

$$\Sigma = \langle \underline{n}_t \underline{n}_t^T \rangle \qquad (14)$$

where $\underline{n}^T$ denotes the transpose of $\underline{n}$. From the signal $\underline{x}_t$ the covariance function C can be estimated:

$$C_k = \langle \underline{x}_t \underline{x}_{t+k}^T \rangle = C_{-k}^T \qquad (15)$$

These covariance matrices obey the multivariate Yule-Walker equation:

$$C_k^T = \Sigma_{i=1}^{p} A_i C_{k-i}^T + \Sigma \delta_{k,0} \qquad (16)$$

which enables the calculation of the model parameters from the estimated covariances. This is the solution to the problem of Sect.A2.1 of finding the system structure from the observed signals. It was enabled by using the causality of the system implicitly in the AR model: the A_i are zero for $i \leq 0$ which leads to the Yule-Walker equation. Also for the solution in the multivariate case recursive algorithms were constructed (10,11) as an extension of the Durbin procedure (9). After the establishment of the MAR model the interaction of the signals is completely known via the set $\{A_i\}$ and the noise source properties given by Σ. At this point we can obtain frequency-domain quantities generally used for system description: spectra, transfer functions, etc. After Fourier transformation of Eq.(13) we obtain:

$$\underline{X}(f) - \Sigma_{i=1}^{P} A_i \underline{X}(f)\exp(-j2\pi f i\Delta) = \underline{N}(f) \qquad (17)$$

The imaginary unit is denoted by j. If the system transfer matrix G(f) is defined as the matrix of transfer functions G_{ij} between the noise source $N_j(f)$ and the signal $X_i(f)$:

$$\underline{X}(f) = G(f)\underline{N}(f) \qquad (18)$$

then it can be seen that

$$G(f) = \left[I - \Sigma_{i=1}^{P} A_i \exp(-j2\pi f i\Delta) \right]^{-1} \qquad (19)$$

where I denotes the unity matrix. The spectral matrix $S_{xx}(f)$ of the signals can be easily derived:

$$S_{xx}(f) = < \underline{X}^{*}(f)\underline{X}^{T}(f) > = G^{*}(f)\Sigma G^{T}(f) \qquad (20)$$

where $\underline{X}^{*}$ is the complex conjugate of $\underline{X}$. The ii component of S_{xx} is the autospectrum of signal x_i; the ij component is the cross-spectrum of x_i and x_j. If the physical noise sources in the system are uncorrelated (and if analysis conditions are correct, see Sect.A2.3) then the identified noise covariance matrix is diagonal: $\Sigma=\mathrm{diag}(\Sigma_{11},\ldots,\Sigma_{mm})$ where Σ_{ii} represents the intrinsic noise variance in signal x_i. For the autospectrum of x_i then holds

$$S_{ii}(f)=\Sigma_{j=1}^{m} G_{ij}^{*} G_{ij} \Sigma_{jj} \qquad (21)$$

Each term in the sum on the R.H.S. of Eq.(21) is the contribution to the spectrum of the signal by each noise source n_j. The Noise Contribution Ratio (NCR_{ij}) of x_j to x_i is defined as its relative contribution:

$$NCR_{ij}(f) = G_{ij}^{*}(f) G_{ij}(f) \Sigma_{jj} \; / \; S_{ii}(f) \qquad (22)$$

The NCR will appear to be an important function; in some way it can be considered as a multivariate equivalent of the coherence function, which is the relative power in the output of a system due to the input.
Finally, the open-loop transfer functions $H_{ij}(f)$ between the signals can be found together with the shaping filters $H_{ii}(f)$. Rewrite Eq.(17) as

$$\underline{X}(f) = H_a(f)\underline{X}(f) + H_b(f)\underline{N}(f) \qquad (23)$$

where the diagonal elements of H_a and the non-diagonal elements of H_b are zero; then

$$\underline{N}(f) = H_b^{-1}(f)(I-H_a(f))\underline{X}(f) = G^{-1}(f)\underline{X}(f) \qquad (24)$$

From this equation the H_{ij} can be obtained:

$$H_{ii}(f) = 1 \;/\; G_{ii}^{-1}(f) \qquad (25a)$$

$$H_{ij}(f) = -G_{ij}^{-1} \;/\; G_{ii}^{-1} \qquad (25b)$$

Here $G_{ij}^{-1}(f)$ follows from Eq.(19). At this point we have established the theory for determining system characteristics and noise sources from the observed data. This procedure can be implemented in a computer program and easily applied to measurements. In practice, however, some problems arise that influence the correctness and precision of the identified system structure. These will be discussed in the next section.

A2.3. Practical aspects of MAR modelling.

A2.3.1. Model order selection. In the previous sections it was assumed that the model order p of the fitted AR model was known. When in practice empirical data are analysed, the model order is not known in advance and has to be estimated together with the other parameters. Referring back to Eq.(7), the AR model can be regarded as a predicting filter with the noise n_t as the difference between predicted and observed output. That model order is optimal that predicts the signal x_t in the best way; in this case the residual noise sequence n_t is white (all predictability is removed) and has a minimum variance σ^2. In practice the scheme is followed in which a number of succesively increasing model orders is tried. This fact emphesizes the use of recursive algorithms. The whiteness criterion can be applied to the residual sequence that can be calculated from the original data after the model has been established. A more simple method is the comparison of the spectra obtained by Eq.(20) and those obtained with standard FFT methods. If the model order suffices, these are equivalent within statistical accuracy (13). For a multivariate model all auto- and cross-spectra have to be taken into account. The minimum variance criterion is then more easily incorporated. Instead of minimum σ^2 a minimum of $\det(\Sigma)$ is obtained.
For practical cases, we have only a limited amount of samples available which implies that the calculated spectra and correlation functions are afflicted with statistical fluctuations. The differences between observed and modelled correlation functions are then not significant in a statistical sense. Increasing the model order is in fact the further fitting of random deviations. For an optimal choice of the model order we need a criterion that balances the reduction in the residual variance with an increase of a penalty function based

on the number of fitted model parameters. Such criterion has been established by Akaike (14,15) based on information theory. For Gaussian signals the optimal model order is given by the minimum of the information criterion AIC:

$$AIC(p) = N \ln|\Sigma| + 2m^2p \qquad (26)$$

where $|\Sigma|$ is the determinant of the noise covariance matrix, m the number of signals and p the model order. The last term in Eq.(26) represents the loss function equal to twice the number of parameters fitted from the N available data points. The AIC has been used extensively for identification problems using inherent noise (3,11-13).

Some comments have to be made on the use of the AIC in the present work. The AIC gives an optimal model order in a global sense: based on all data and correlation function points. For purposes where we are mainly interested in frequency domain properties it may occur that the resemblance of the AR-based spectra for a given order and the FFT-based ones is only good in a certain frequency region, while deviations exist in a different (most often lower) region. This is due to the fact that an accurate fit of the low frequencies has to extend over a larger part of the correlation function than for the higher frequencies. If we are mainly interested in the higher frequency part, the AIC might give rise to unnessary large model orders. (For some experiments even a satisfactory low frequency fit was obtained with under-optimal orders). These points are mainly of importance in cases where very large model orders are necessary, as the amount of computer time is proportional to the square of the order. We encountered the need for large orders rather often during our research. This may have two causes.

The first is that the sampling frequency has to be chosen much higher than would be expected on basis of the Nyquist criterion. This point is commented in the next section. Its consequence is that the fit (which has to extend over a fixed correlation lag for an acceptable low frequency fit) involves more correlation function estimates thus a larger order.

The second point is that we often had fairly long signal records available, implying an accurate spectrum and correlation function estimate. This tends to increase optimum model order (16); in most literature the AR fit was based on moderate amounts of data (a few thousand samples). This tendency can be understood by the fact that in general the physical process is not an AR process but is forced into such a model, motivated by Sect.A2.2. Accurate measurement of the system means the need to model more closely by AR, thus the need for higher model orders. In practice a good-at-eye criterium was used for the selection of the model order at which the recursion was stopped; quite subjective but generally satisfactory.

A2.3.2. The effect of sampling frequency . In the course of our research it appeared to be very important to use sufficiently high sampling frequencies of the data in order to obtain correct results from the model (NCR's, transfer functions). In the this section the reasons will be discussed.

It is well-known that the sampling frequency must be chosen at least twice the maximum frequency occurring in the signal to avoid aliasing, according to the Nyquist-criterion. If this condition is not fulfilled, large deformations of the measured spectra will occur and an incorrect system will be identified. In practice the signals will be low-pass filtered to satisfy this condition. But even then problems may arise which can only be solved by a further increase of the sampling rate. These are connected with the fact that a continuous-time system is modelled with a discrete-time process.

Consider a multivariate system as given in Fig.A2.2, with uncorrelated noise sources. The outputs are measured and an AR model is fitted to this data. One of the results is the noise covariance matrix Σ. It would be expected that in the case of uncorrelated noise sources, also no correlations are found in the identified noise sources, i.e. that the Σ matrix is of diagonal form. (Off-diagonal elements of Σ represent correlations in the noise sources). However, in practice we have observed that very often the identified noise sources were strongly covariant, although this was certainly not true for the physical noise sources. This observation is based both on reactor signal analyses, as well as simulation experiments. As to our knowledge, it has not been treated extensively in literature and no explanation could be found.

The effect of the non-diagonal character of the noise matrix is important. In that case the NCR's cannot be estimated and the identified transfer functions between the signals are erroneous. It was an important question to settle before being able to continue a succesful AR modelling of the reactor noise. The cause of the problem has been traced down to the fact that in the real system, due to its continuous time character, apparent instantaneous transmission of information between the signals is possible. The AR model does not allow for such transfer as will be clarified.

Consider the MAR model defined by Eq.(13):

$$\underline{x}_t = \Sigma_{i=1}^{p} A_i \underline{x}_{t-i} + \underline{n}_t \qquad (27)$$

It will be clear that the effects of variations in one signal x_i at time t cannot be transferred to the other signals before time $t+\Delta$. The model does not allow for immediate response of x_j to x_i, or at least for response within the time interval Δ. Note that this effect is independent of the frequency content of the fluctuation, which may be sufficiently limited. For physical systems there can easily be some response within this time. Figure A2.3 may illustrate this point for a signal x_2 responding by a simple lag on a step input of x_1.

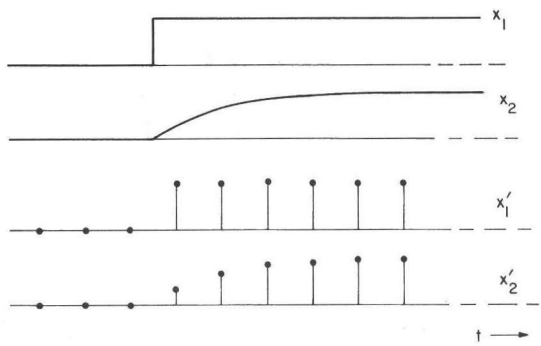

Fig.A2.3
Effect of sampling: x_1' and x_2' are the sampled versions of the input step x_1 and the response x_2. x_2' exhibits an instantaneous response to x_1' which is not accountable for in the autoregressive model.

If the sampling instants are not synchronous with the input variations, a variation in the sampled version of x_1 and x_2 will occur simultaneously. It will be clear that such variation cannot be modelled as $x_2(t)=\Sigma_i A_i x_1(t-i\Delta)$ if i is always greater than 0; the variation will automatically be interpreted as a fluctuation in the x_2 intrinsic noise source, while in fact only the noise source of x_1 fluctuated. In this way it will be clear that a correlation in the modelled noise matrix is obtained.
The foregoing argument can be put in a better mathematical formulation. It will be clear that an inclusion of the i=0 term in Eq.(27) might improve the model to allow for instantaneous response:

$$\underline{x}_t = \Sigma_{i=0}^{p} A_i \underline{x}_{t-i} + \underline{n}_t \qquad (28)$$

The noise soure $\underline{n}_t$ is a white noise sequence with diagonal covariance Σ. Note that (28) is not a conventional AR model due to the presence of the A_0 term. It can be organised to standard form by removing the A_0 term from the summation:

$$(I-A_0)\underline{x}_t = \Sigma_{i=1}^{p} A_i \underline{x}_{t-i} + \underline{n}_t$$

or

$$\underline{x}_t = \Sigma_{i=1}^{p} (I-A_0)^{-1} A_i \underline{x}_{t-i} + (I-A_0)^{-1} \underline{n}_t$$

$$= \Sigma_{i=1}^{p} B_i \underline{x}_{t-i} + \underline{z}_t \qquad (29)$$

This is a normal AR model with noise source $\underline{z}_t$ that can be identified by standard methods as described earlier. The procedure yields a covariance matrix Q of $\underline{z}_t$, that is related to Σ:

$$\langle \underline{z}_t \underline{z}_t^T \rangle = Q = (I-A_0)\Sigma(I-A_0)^T \qquad (30)$$

from which it is clear that Q is not diagonal. Also the transfer functions H_{ij} and G_{ij} will be affected by the immediate response. The transfer function matrix according to the correct model (including A_0) is G; denote the identified one by G'. For G' holds:

$$G' = G\,(I-A_0) \qquad (31)$$

At this point we have to comment the following. The non-diagonal character of the noise source has been mentioned in literature(11,12). Most authors just neglected this fact and used only the Σ_{ii} terms in their procedure, e.g. to compute the NCR's. It will be clear that this will lead to incorrect NCR estimates and to meaningless transfer functions. A solution was suggested by Kitamura(11) by applying a linear transformation on Q to diagonalise it by its eigenvectors. This is in fact a method to try to extract the A_0 from the fitted Σ; it leads however to incorrect results. At first it can be seen that the tranformation matrix is not unique (the m eigenvectors of Q can be arranged in m! ways each giving different results). Furthermore, none of the possible transformation matrices produced the correct results as was found out while testing this procedure on simulation experiments.
In fact any procedure that tries to find A_0 from the observed Q will be useless, as A_0 is not uniquely defined by Q. This can be seen with ease: Q, being a symmetrical covariance matrix, has m(m+1)/2 independent elements. The number of unknowns to be obtained is larger: m elements of Σ and m^2 of A_0. Unless there is some a-priory information on A_0 it cannot be obtained.
The problem discussed here is not completely new. From control theory it is known that identification problems occur on a closed-loop system if instantaneous response around the loop exists. Solutions are suggested(17,18) by the use of an instrumental variable method, where identification is performed using another input signal that is correlated with the input perturbations, but not with the feedback response. In this way it is possible to estimate the amount of instantaneous response and thus assign a value to A_0. It is clear that such a solution is not possible in our case because no signals are available that can act as instrumental variables since they are all within the closed loop.
The solution to the problem of correlation in the modelled noise sources lies in the increase of the sampling frequency. In this way the magnitude of the variation in one signal in one sampling interval Δ due to other signals can be decreased. This approach is based on the assumption that the transfer functions between the signals have a limited bandwidth, as is generally the case for physical systems. At present, regrettably, no criterion is known to predict the minimum required sampling frequency. It would be suitable to have a Nyquist-criterion-like formula to find the maximum sampling interval as a

function of e.g. the system time constants. It will be clear that it is a function of the derivatives of the response signals. These are determined by the time constants involved and the input signal spectra.
At present the experimental procedure is the testing of successive higher sampling frequencies until a satisfactory degree of diagonalisation is obtained for a specific identification task. This is tested by the obtained Σ and NCR's. The sampling rate cannot be increased without penalty: it requires larger model orders to obtain a sufficiently close fit of the spectra. Just as with the choice of the model order, an important subjective factor steals into the modelling due to a lack of satisfactory objective criteria.

A2.3.3.Accuracy and identifiabiliy. After the observed time series are fitted into an AR model, the problem arises what the accuracy is of the model. Rather than in the accuracy of the model parameters A_i we are interested in the accuracy of the spectra, NCR's and transfer functions. Related to this problem of accuracy is the problem of identifiability: under which conditions can the transfer functions be obtained from the available data. The relation lies in the fact that if a specific H is not identifiable, its precision (the inverse variance of its estimate) will tend to zero.
Accuracy is defined by two aspects: the bias and the variance of the estimate. For the bias of the estimates, we can assume that these will be neglectable, compared with the variance, if a sufficient model order is used. For the spectra this is readily understood. The spectra are obtained by a fit of the (unbiased) covariance function estimates. Bias in the spectra is caused by the finite width of the lag window that is applied to the covariance function. In our experiments the available lag was mostly sufficient. Furthermore, the AR modelled spectra are generally much less biased as they are calculated from a covariance function that is extrapolated by an AR series beyond the time window; this forms the relation between AR models and the so-called maximum entropy spectral analysis (3,19). It will be assumed that also for the NCR's and H's the bias is negligible.
The variance of the spectra is determined by the observation time T and the bandwidth B of the filtering procedure that is applied when estimating a point of the spectrum. For FT based spectra the bandwidth is approximately the inverse of the available time lag (dependent of the applied correlation function window); the well-known relation holds $var(S_{xx})/(S_{xx})^2=1/BT$. For the AR modelled spectra the bandwidth is the inverse of the time lag used for the fit (thus model order times sampling interval). For this case the relative variance of the spectral estimate is determined by p/N; p the model order and N the number of samples (21).
For the NCR's and H's much less is known. For multi-input systems with observable inputs relations have been established (2,6) for the precision of the estimates of the transfer functions. But for the closed-loop system with

unmeasurable inputs as in the present case no formulas are available; the precise identifiability conditions thus remain unclear. It is trivial that the precision improves with observation time and gets worse with increasing model order (more estimated parameters from the same amount of data).
Following Kitamura (20) the identifiability conditions can be obtained in a qualitative way. Consider the system in the structure of Eq.(18). The information of the noise sources n_j is transferred to the outputs x_i via G_{ij}. The G's directly determine the open-loop transfer functions H between the variables by Eqs.(25). It is clear that if one of the noise sources n_k is not present (the signal x_k has no intrinsic noise) no signal is transferred via G_{ik} and no information on G_{ik} can be obtained from the output signals. This implies that all H's that are computed using G_{ik} are undefined. It appears that in this case only the transfer functions from the other variables towards the variable with no intrinsic source can be found; the other are meaningless. Kitamura recommends an a-posteriori check on the identified H's by regarding the relative amount of intrinsic noise in each variable : $(\Sigma)_{ii}/\phi_{ii}(0)$. If for one of the signals this noise source is very small, only the transfer functions towards this signal can be obtained. If two or more of the noise sources lack none of the transfer functions can be obtained.
The above approach has to be generalised. It will be clear that if in one signal the intrinsic noise lacks completely, problems occur. But the argument is also applicable to every separate frequency. If due to the specific character of the shaping filter the intrinsic noise lacks in only a limited frequency region, only at those frequencies not all transfer functions can be found, while at other frequencies no problem exists. This is a principal limitation of system identification by the intrinsic noise of the process: the components that are not actuated by the noise cannot be obtained.

Partial identification. In practice the above stated problem can sometimes be overcome due to the specific structure of the system. This is the case in one of the analyses of the reactor signals (see Chapter 6). The structure is shown in Fig.A2.4a.
The main features are the absence of n_2 and of direct transfer between x_1 and x_3; all information is transferred via fluctuations in x_2. From the previous section it will be clear that a straightforward AR analysis will only yield the transfer functions H_{21} and H_{23}. However, if we leave x_3 out of the analysis, the structure of Fig.A2.4b remains. The noise source n_3 will be translated into an equivalent source n_2'. Due to the absence of direct response, H_{12} and H_{21} remain unchanged. These transfer functions can thus be obtained by the partial identification of the system. The same argument holds when x_1 is left out of the analysis and the conclusion is that with this method we obtain the complete system. This result will be used in Chap.6.

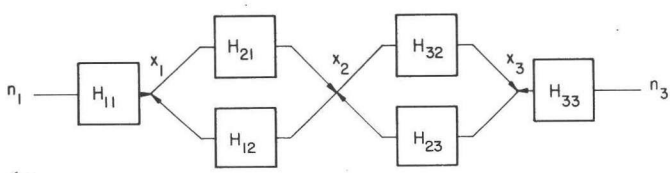

Fig.A2.4a
Three-variable system with no direct coupling of x_1 and x_3.

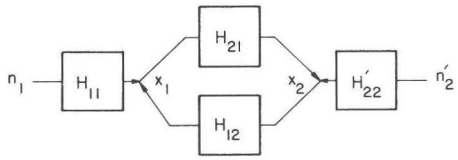

Fig.A2.4b
Equivalent of Fig.A2.4a for partial identification (x_1 - x_2).

Presence of measurement noise. For the MAR model of Eq.(13) it will be clear that all noise sources are in principle allowed to activate all outputs. This can be interpreted as the noise sources to be within the feedback loop. For the physical noise sources that drive the fluctuations in the physical quantities this is clearly correct. However, the signals obtained from tranducers measuring the physical quantities are often contaminated with measurement noise. This noise is located outside the feedback loop and cannot be modelled correctly by AR. If such noise is present, it will affect the modelled transfer functions and NCR's. With the aid of Fig.A2.2 we can envisage the following consequences of measurement noise on signal x_k:
-NCR_{kk} will increase due to the extra noise; NCR_{ki} will consequently decrease.
-NCR_{ik} will remain unchanged as only the physical noise n_k is of importance.
-The modulus of the transfer function H_{ik} will decrease: the input power increases but the output power remains equal. The phase will not be affected.
The precision of the estimates will generally decrease due to the extra amount of uncorrelated noise.

A2.4.Examples of AR modelling.

A2.4.1.Introduction. In order to illustrate the MAR modelling method and the points that have been discussed previously some examples are given. These may serve as a validation of the method and the computer programs that were written. The demonstrations are performed on electrical networks of known structure, driven by noise. An analog simulation was preferred to a digital one using computer-generated time series, as to approximate as closely as possible the realistic analysis conditions including data processing. Furthermore, analog simulation enabled easier testing of the effect of filtering and sampling rate.

Two demonstration networks were used. The first is a closed-loop two-variable network on which the effect of sampling interval, presence of noise sources and correctness of estimated NCR's and transfer functions was investigated. The second system is a three-variable network where the same features were analysed; furthermore the partial identification technique of A2.3.3 and the effect of signal bandwidth were studied.

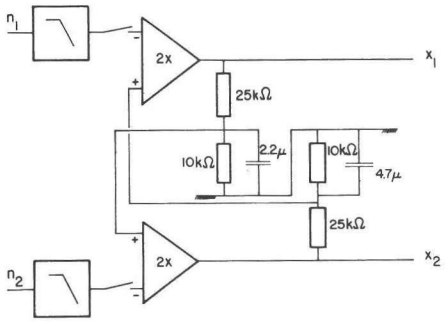

Fig.A2.5
Two-variable network used for demonstration of AR-analysis (exps. 1 - 3).

A2.4.2.Two-variable network. A schematic diagram of the system is given in Fig.A2.5. The two signals x_1 and x_2 are outputs of amplifiers while the signals are coupled via two simple low-pass filters. The system is actuated by two gaussian white noise generators with filtered outputs to obtain the desired bandwidth. The filters are 8-pole Butterworth low-pass filters with an adjustable break frequency, set at 10.0Hz for the present experiment. The noise sources can be switched off to study the consequence of their absence. For this system all parameters are known or can be measured, so a check on the results of the AR model is possible.

Three measurement series were performed on the output signals:

1. Both noise sources present, sampling interval Δ=2 ms, total number of samples N=1024000.
2. Only n_1 present, Δ=4 ms, N=102400.
3. Only n_2 present, Δ=4 ms, N=102400.

From the sampled outputs, spectra and correlation functions were calculated by a FFT-based algorithm. The covariance functions were input to the AR modelling program and NCR's, AR-spectra and H's computed. To study the effect of sampling interval, a special procedure was applied. From the sampled signals the covariance functions can be obtained at time instants $k\Delta$. From this estimates the values at $k(m\Delta)$ can be considered as the covariance funtions if the signals were sampled with $\Delta'=m\Delta$, as long as the larger sampling time Δ' still satisfies the Nyquist criterion to prevent aliasing. In this way we can investigate the effects of sampling rate on the modelled results with the advantage that the differences are only due to the sampling interval, not to statistics as the same data is used for all runs.

The first effect to be demonstrated is the influence of sampling rate on the

diagonalisation of the noise source covariance matrix Σ. A measure for the diagonalisation is the noise correlation coefficient

$$\rho_{12}=\Sigma_{12}/(\Sigma_{11}\Sigma_{22})^{\frac{1}{2}}. \qquad (32)$$

Δ (ms)	p	ρ_{12} at experiment 1	2	3
64	31	0.545		
16	60	0.315	0.884	0.808
8	60	0.139		
4	60	0.054		
4	100		0.147	0.097
2	25	0.020		
2	50	0.012		
2	100	0.010		
2	150	0.010		

Table A2.1 Noise source correlation coefficients as function of sampling time Δ' and model order p for experiments 1, 2 and 3.

Results are shown in table A2.1 . It appears that the effect of a too low sampling rate can be very large, particularly for the case that only one source is present (exp.2 and 3). It can be understood that for exp.2 the correlation is larger than for exp.3, as the time constant of the involved filter is smaller and thus the amount of instantaneous response.

The effect of the sampling interval on the NCR's is also large. Remember that the NCR_{ki} is the relative amount of power in the signal x_k due to the ii component of Σ only. If the diagonalisation is perfect, the sum of NCR's would be unity; if correlation remains the sum will deviate from unity. This is shown in Fig.A2.6 where the NCR's for case 1 are given with Δ'=32 ms and Δ'=2 ms. The deviations are apparent; it can be concluded that the diagonalistion is satisfactory at the smaller sampling interval. For the exps.2 and 3 results are not shown; the same conclusions hold and Δ=4ms appears reasonable. In Fig.A2.6 also the NCR's are drawn that were calculated using the spectra of exp 2 and 3; these give the contribution in every signal due to each source directly and can be combined to the expected NCR's. The AR modelled NCR's agree very good with the theoretical ones, deviations are due to the limited accuracy of the estimated spectra.

In Fig.A2.7 the gain and phase of the estimated transfer functions H_{12} and H_{21} are plotted, together with their true values. It can be concluded that for the

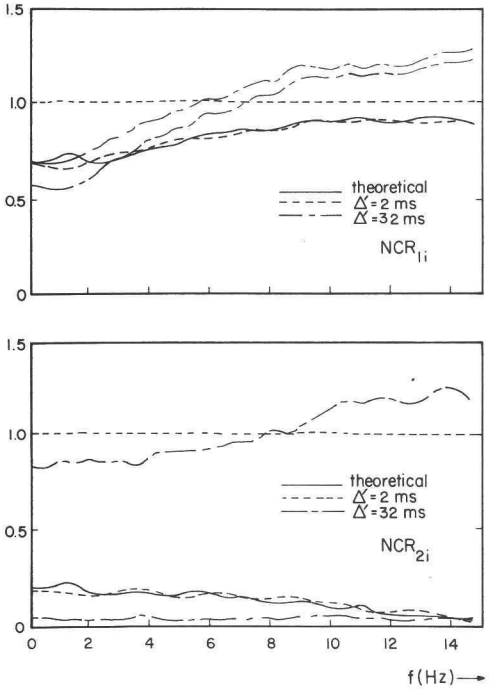

Fig.A2.6
Effect of sampling rate on the Noise contribution ratios (NCR's) of the two-variable system.

The NCR's are shown cumulatively: the distance between correspondig curves represents the fractional contribution of noise source i to signal j. (See also Fig.A2.9).

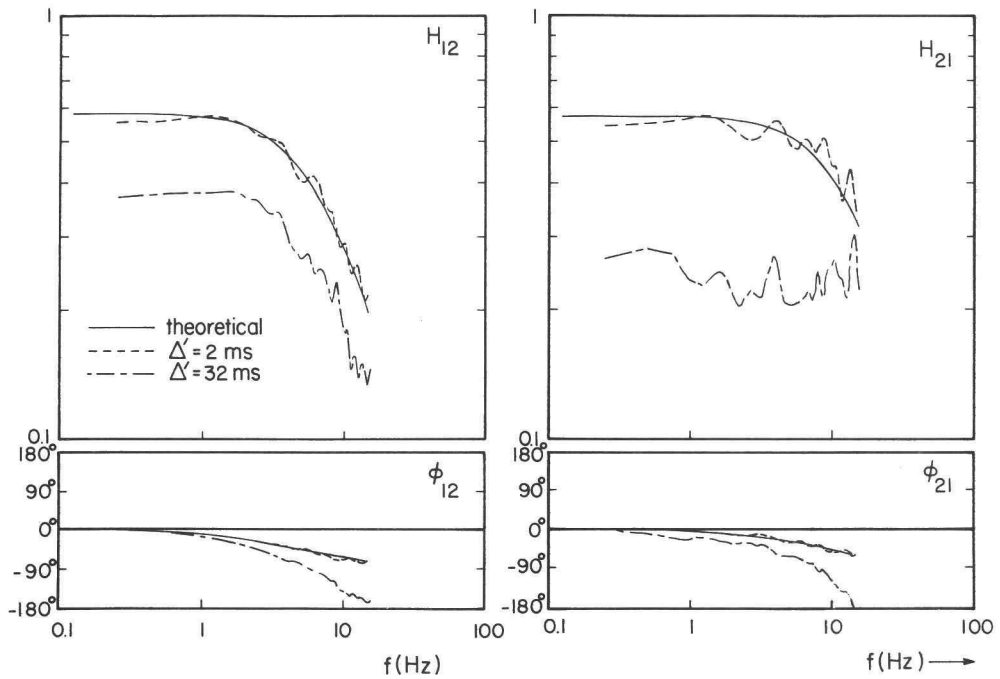

Fig.A2.7
Effect of sampling rate on the transfer functions between the signals obtained by autoregressive modelling.

case where the diagonalisation was acceptable also the H's are estimated correctly with (for this case) a reasonable accuracy as indicated by the oscillations around the true curves. For the analyses with Δ'=32 ms large deviations exist in the modelled transfer functions. For the cases 2 and 3 the identified H_{21} and H_{12}, respectivily, coincide with the theoretical curves, while complete erroneous reverse H's were found. Here, too, it appears that a larger sampling interval affects the correctness of the transfer functions.

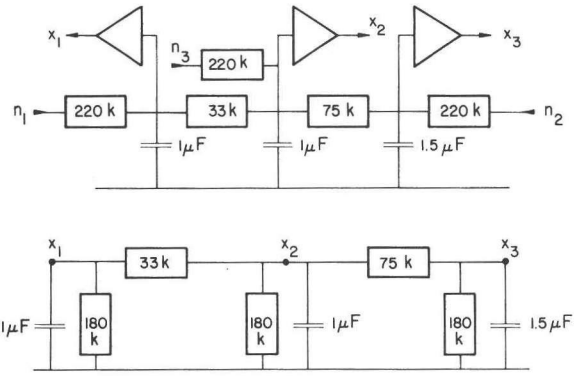

Fig.A2.8
a (top) : Three-variable network used for demonstration.
b (bottom) : Equivalent signal diagram.

A2.4.3.Three-variable network. Measurements were performed on the network shown in Fig.A2.8a. The scheme to calculate transfer functions is given in Fig.A2.8b. The effective values of the resistors are due to the input impedance of the amplifiers. This network was used to test the AR fitting on a system with more than two variables in the presence or absence of noise sources. One of the special features of this network is the absence of direct transfer between output 1 and 3; we expect the identification result to show the same. Two experiments were performed on the system: exp. 4 with all noise sources present, exp. 5 with that of signal 2 switched off. In both experiment the signals were low-pass filtered at 10.0Hz and 614400 samples were taken of each with an interval of 2 ms. First exp. 4 will be discussed.

Δ(ms)	p	ρ_{12}	ρ_{13}	ρ_{23}
32	27	0.669	0.135	0.284
16	50	0.395	0.045	0.149
8	100	0.211	0.006	0.074
4	100	0.109	-0.002	0.037
2	90	0.071	-0.009	0.016

Table A2.2 Noise source correlation coefficients as function of sampling time for experiment 4.

The first point of interest is the dependence of the noise covariance on sampling interval. This was checked as described in the previous section. Now three correlation coefficients ρ_{12},ρ_{13} and ρ_{23} are obtained. Results are given in Table A2.2 . Again the effect is clear. 2 ms was the shortest possible interval in the analysing system while preserving sufficient spectral resolution. For this condition the diagonalisation was sufficient for ρ_{13} and ρ_{23}, less sufficient for ρ_{12}. This is understandable as the shortest time constants in the system are between 1 and 2. The resulting NCR's for Δ=2 are shown in Fig.A2.9, together with their true values. The remaining correlation between n_1 and n_2 causes the sum to deviate from unity, mainly for x_1 and x_2. Apart from this effect the NCR's are fairly correct.

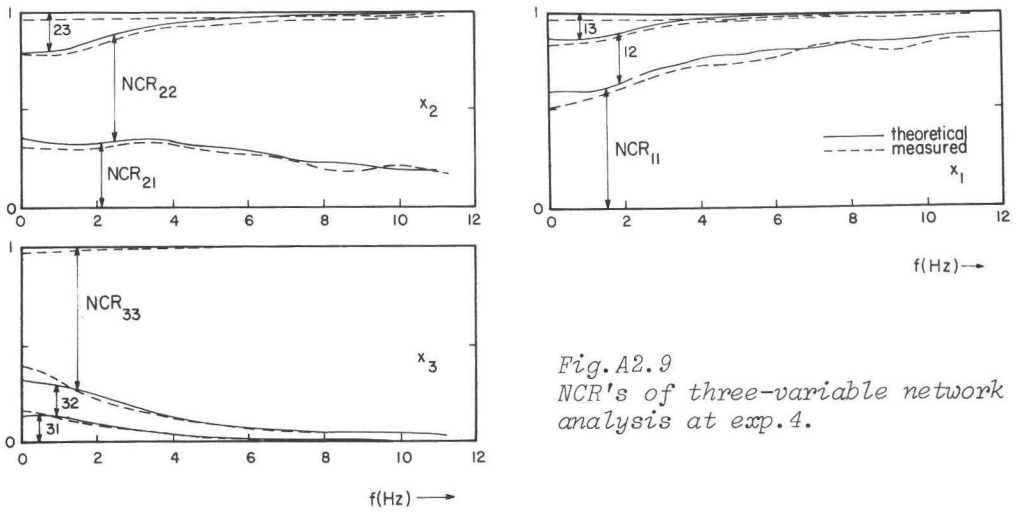

Fig. A2.9
NCR's of three-variable network analysis at exp. 4.

The fitted transfer functions are shown in Fig.A2.10. The measured curves agree with their theoretical ones, the small oscillations are due to finite precision. The deviation for H_{23} may be due to the nonperfect diagonalisation. It can also be noted that the precision decreases with the corresponding NCR

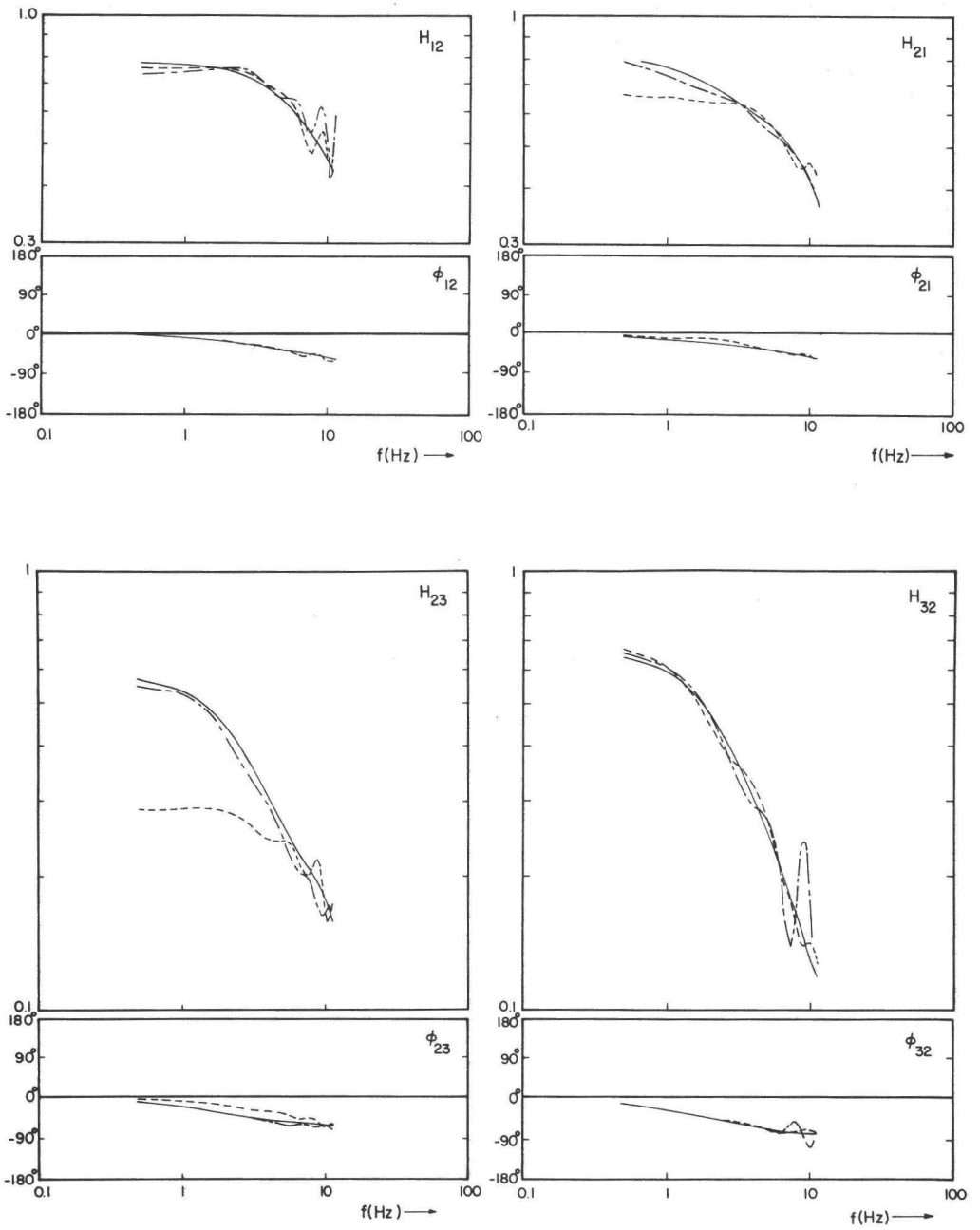

Fig.A2.10
Transfer functions from AR-modelling of the three-variable network at exps. 4 and 5.
———————: *theoretical*
— — — — — —: *complete analysis (exp.4)*
——— — ———: *partial analysis (exp.5)*

value as has been discussed in Sect.A2.3.3. The estimates for H_{13} and H_{31} are not shown. In the physical system they are not present, in the analysed system their value was very small compared to the other transfer functions (approx. 0.02 for the gain).

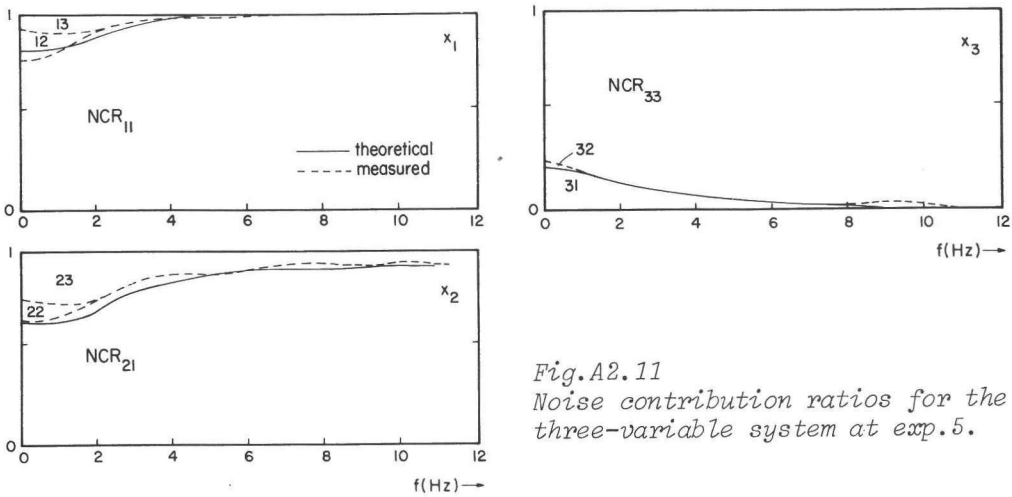

Fig.A2.11
Noise contribution ratios for the three-variable system at exp.5.

An interesting test on the modelling procedure is formed by experiment 5 where the second noise source is missing. The expected consequence is the impossibility to determine other H's than H_{21} and H_{23}. For this case only an analysis with Δ=2 ms was performed. The observed noise correlation coefficients were ρ_{12}=0.061, ρ_{13}=0.004 and ρ_{23}=0.040. The strength of the identified noise sources, relative to the signal variance, was $3.3\ 10^{-7}$, $2.3\ 10^{-7}$ and $3.6\ 10^{-7}$ resp. for n_1, n_2 and n_3. It can be seen that the second noise source is still rather large and that some correlation remains. Furthermore numerical problems arise due to the fact that the determinant of the noise matrix Σ is very small; this is a good indication that one of the noise sources is missing. The consequence of the remaining noise covariance is the remnant of NCR_{i2} in the NCR plots in Fig.A2.11, mainly for the first two signals at frequencies under 2 Hz. The sum of NCR_{i3} and NCR_{i2} is approximately the expected value for NCR_{i3}; it looks as if part of the noise n_3 is transferred to n_2. The transfer functions H_{21} and H_{23} are estimated correctly above 2Hz, at lower frequencies deviations exist; the other transfer functions show large oscillations and are meaningless as expected. For this case a partial identification technique as described in A2.3.3 may be performed. The conclusions are that than the obtained NCR's are correct, although some effect remains of the non-ideal diagonalisation. The identified transfer functions also agree well with their theoretical expectations (also shown in Fig.A2.10). It has to be noted that for the x_1-x_3 partial identification the obtained transfer functions are the products H_{13}=H_{23}.H_{12}, etc. as can be readily understood from Fig.A2.8b.

Effect of signal bandwidth. Using the 3-variable system discussed above with sources n_1 and n_3 present and using x_1 and x_3 as outputs the effect of filtering on the modelled noise sources was studied. Table A2.3 shows the observed correlation coefficients ρ_{13} for different conditions.

Δ(ms)	p	5Hz	10Hz	20Hz
64	25	0.199		
32	25	0.097	0.071	
16	25	0.050	0.035	0.017
8	50	0.012	0.010	0.009
4	100	0.012	0.010	0.009
2	100	0.006	0.006	0.007

Table A2.3 Noise source correlation coefficients as funtion of sample time and bandwidth (Exp 5).

It can be concluded that an increase of bandwidth leads to a reduction of the correlation. This can be understood from the point that, in the present case, signal coherence decreases with frequency. Increasing bandwidth means the addition of more, less correlated noise to the signals so the effective correlation decreases. It is worthwile to mention that analysis of reactor signals leads to increased correlation if the signal coherence increases with frequency in the analysed band (Chapter 6). This is in accordance with the abovementioned observations.

A2.References

1. Box,G.E. and G.M.Jenkins. Time series analysis, forecasting and control, Holden-Day, San Francisco (1970).
2. Jenkins,G.M. and D.G.Watts. Spectral analysis and its applications, Holden-Day, San Fransisco (1968).
3. Childers,D.G.(ed). Modern spectrum analysis, IEEE-Press, New York (1978).
4. Eykhoff,P.(ed). Trends and progress in system identification, Pergamon Press (1981).
5. Robinson,E.A. Multichannel time series analysis with digital computer programs, 2nd Ed., Holden-Day, San Fransisco (1978).
6. Bendat,J.S. and A.G.Piersol. Random data, Wiley-Interscience, New York (1971).
7. Hoogenboom,J.E.,H.van Dam,E.B.J.Kleiss,G.C.van Uitert and D.Veldhuis. Progress in Nucl.Energy 9,279-290 (1982).
8. Verhagen,C.D.J.M. Collegehandleiding Systemen en Signalen I, Delft (1973).
9. Durbin,J. Rev.Inst.Int.Stat. 28,233-243 (1960).
10. Whittle,P. Biometrica 50,129-134 (1963).
11. Upadhyaya,B.R.,M.Kitamura and T.W.Kerlin. Ann.Nucl.Energy 62,1-11 (1980).
12. Fukunishi,K. Nucl.Sci.Eng. 62,215-225 (1977).
13. Allen,J.W. Progress in Nucl.Energy 1,603-614 (1977).
14. Akaike,H. Ann.Inst.Statist.Math. 23,163-180 (1971).
15. Akaike,H. IEEE Trans.Autom.Contr AC-19,716-723 (1974).
16. Sawaragi,Y.,T.Soeda and T.Nakamizo (1981). Chapter 3 in 4.
17. Wellstead,P.E. and J.M.Edmunds. Int.J.Control 21,689-699 (1973).
18. Matsubara,K. J.Nucl.Sci.Techn. 17,737-746 (1980).
19. Bos,A van de. IEEE Trans.Inform.Theory IT-17,493-494 (1971). Reprinted in 3.
20. Kitamura,M.,K.Matsubara and R.Oguma. Nucl.Sci.Eng 70,106-110 (1979).
21. Ulrich,T.J. and T.N.Bishop. Rev.Geophysics and Space Phys. 13,183-200 (1975). Reprinted in 3.

APPENDIX 3. A MODEL FOR THE DYNAMICS OF A BOILING WATER REACTOR.

A3.Abstract.

A model has been established to derive the dynamic characteristics of the Dodewaard reactor. It is founded on the basic physical processes that govern reactor dynamics. The values of the different parameters in the model are estimated from experimental and theoretical data. The transfer functions of reactivity and steam flow to power and pressure are obtained. The sensitivity to changes in several parameters is investigated and can be understood.

A3.1. Introduction.

A model has been established that predicts the relation of variations in several physical variables in the reactor system. These are both neutronic variables (flux, reactivity effects) as well as process variables (like thermal power, pressure, steam flow, control valve positions). The need for such a model is given by the desire to understand the spectra, transfer functions and response functions that were measured both by noise techniques and by perturbation measurements. Furthermore, an independently obtained model may be of use in the validation of these results (see also Chapter 6 and Appendix 1).

The model discussed in this appendix is founded on the basic relations between the physical quantities that govern reactor behaviour. These relations often contain non-linear terms which disable an easy solution of the differential equations involved. However, due to the fact that our main interest lies in noise behaviour and other small-signal characteristics, a linearisation of the equations is possible around the steady-state conditions. This enables a frequency-domain approach after the Fourier transformation of the linearised formulae. (For larger deviations such as transient analysis, the non linear behaviour plays an important role and other approaches, like analog computer simulations may be useful).

The model leads to a set of transfer functions between the output and the input variables. Many quantities can act as output (power, pressure, steam flow,

(fuel)temperature, void content). For the inputs it is useful to take those, by which normal reactor operation is controlled or that act as noise sources in the fluctuation behaviour. During normal operation only three variables can be manipulated: control rods (to control reactivity), steam flow (to control pressure) and feedwater flow (to control reactor water level). For the noise measurements control rods can be neglected, because these serve as burn-up compensation and are repositioned only incidentally. Reactivity fluctuations (mainly due to the boiling process) replace their role as input variables, although it is not a directly measurable input variable.

Steam flow forms a second input; this is motivated by the fact that the pressure control system acts on it and because it is one of the important noise sources in the system (see Chapter 6).

Feedwater flow variations appear to have a very small effect on the reactor as far as noise is considered (1). Its influence on e.g. power is very indirect and completely masked by other processes. Feedwater flow is further neglected as an input variable.

For the general outline of the model two zones are regarded. The first is the reactor core. For the dynamics a point-kinetics approximation is used with (external plus feedback) reactivity as input. Power and pressure determine the evaporation of water and the steam content in the core. Steam is removed from the core to the second zone (i.e. the out-of-core part of the vessel). Here pressure build-up takes place due to steam production and (controlled) steam removal to the turbine. Vessel pressure is generated by the amount of steam in the available volume. Core pressure is directly determined by vessel pressure. Reactivity feedback occurs due to coolant (moderator) and fuel temperature and due to core void fraction.

A schematic representation of the reactor is shown in Fig.A3.1 with the main variables of interest shown (see also A3.2 and Table A3.4). In the following sections the model details are evaluated and some results given.

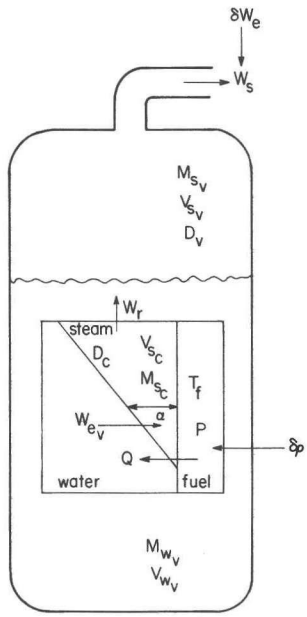

Fig.A3.1
Schematic representation of the reactor with the main variables of interest shown. (see A3.2 and Table A3.4).

A3.2. Basic model equations.

For the neutronics a point-kinetics model is assumed. Power fluctuations δP are caused by reactivity fluctuations $\delta\rho$ via the well-known equations

$$\frac{d}{dt}\delta P(t) = \frac{\delta\rho}{\Lambda}P_0 - \frac{\beta}{\Lambda}\,\delta P(t) + \Sigma_i\lambda_i\delta C_i(t) \qquad (1)$$

$$\frac{d}{dt}\delta C_i(t) = \frac{\beta_i}{\Lambda}\delta P(t) - \lambda_i\delta C_i(t) \qquad (2)$$

These equations are already linearised around steady-state power P_0. The quantities β, β_i, C_i and λ_i have their usual meaning as delayed-neutron parameters, Λ is the neutron generation time. Fourier transformation yields (s denotes the complex angular frequency $j\omega$)

$$\delta P(s) = P_0 G(s)\delta\rho(s) \qquad (3)$$

with G(s) the zero-power reactivity transfer function

$$G(s) = \left[s\Lambda+\Sigma_i\beta_i s/(s+\lambda_i)\right]^{-1} \qquad (4)$$

For the remaining part the equations will directly be given in their linearised, Fourier transformed version.

The reactivity input $\delta\rho$ is the sum of the external and feedback reactivity:

$$\delta\rho(s) = \delta\rho_e(s) + \delta\rho_{fb}(s) \qquad (5)$$

The generated power heats the fuel and is transferred to the coolant as a heat current Q. If it is assumed that fuel temperature fluctuations are much larger than coolant temperature fluctuations, the heat current and fuel temperature are independent of coolant temperature and given by the heat balance:

$$sC_f\delta T_f(s) = \delta P(s)-\delta Q(s) \qquad (6)$$

with

$$\delta Q(s) = G_f(s)\delta P(s) \qquad (7)$$

$G_f(s)$ is the fuel heat transfer function. For a simple model with a single fuel time constant it is given by

$$G_f(s) = (1+s\tau_f)^{-1} \qquad (8)$$

with the fuel time constant τ_f determined by the ratio of fuel heat capacity C_f and total heat transfer coefficient k_{fc}. For a better approach, a transfer function with several time constants is necessary (see A3.3).

The transferred heat is used to generate steam. The evaporation mass flow W_{ev} is given by

$$W_{ev}(t) = Q(t)/h_{eff}(t) \qquad (9)$$

where h_{eff} is the effective evaporation enthalpy of the water (including the amount of energy required to heat the water from feedwater temperature to boiling temperature). Its steady-state value is easily determined as

$$h_{eff} = P_0/W_{s0} \qquad (10)$$

where P_0 and W_{s0} are the steady-state power and ex-vessel steam flow, resp. For a dynamic model, fluctuations in h_{eff} due to variations in boiling temperature (pressure) have to be taken into account. Then,

$$\delta W_{ev}(s) = \frac{\delta Q(s)}{h_{eff}} - P_0 \frac{1}{h^2_{eff}} h_D \delta D(s) \qquad (11)$$

with h_D the pressure derivative of the evaporation enthalpy and δD the pressure fluctuation.
In A3.3 it will be argued that the removal of steam from the core can be described by a simple lag model, characterised by τ_s, the average steam residence time. The equations for removal flow W_r, steam mass M_{sc}, steam volume V_{sc} and void fraction α are

$$\delta W_r(s) = \delta M_{sc}(s)/\tau_s \qquad (12)$$

$$s\delta M_{sc}(s) = \delta W_{ev}(s) - \delta W_r(s) \qquad (13)$$

$$\delta V_{sc}(s) = \frac{1}{\sigma_s} \delta M_{sc}(s) - \frac{1}{\sigma_s} \alpha_0 V_c \sigma_D \delta D(s) \qquad (14)$$

$$\delta\alpha(s) = \delta V_{sc}/V_c \qquad (15)$$

In these equations it is assumed that the change in in-core steam mass M_{sc} is given by the difference of evaporation and removal mass flow. M_{sc} determines directly the in-core steam volume V_{sc} and void fraction α via the steam density σ_s. Pressure dependence is incorporated by the density-pressure derivative $\sigma_D = \frac{\delta\sigma_s}{\delta D}$. The amount of water in the core is simply the remaining volume.
The core pressure D_c is assumed to be equal to the vessel pressure D_v. This pressure is generated by the amount of steam present in the vessel (M_{sv}) and the volume V_{sv} occupied by it; this volume is equal to the volume left by the water. The amount of water in the vessel (M_{wv}) is the total amount of water in the system (which decreases due to evaporation and is balanced by the feedwater) minus the amount of water in the core. As we have assumed a constant

feedwater flow we, obtain for the fluctuations

$$s\delta M_{sv}(s) = \delta W_f(s) - \delta W_s(s) \tag{16}$$

$$\delta V_{sv}(s) = -\delta V_{wv}(s) = -\delta M_{wv}(s)/\sigma_w \tag{17}$$

$$\delta M_{wv}(s) = \delta M_w(s) - \delta M_{wc}(s) = -\frac{1}{s}\delta W_{ev}(s) + \sigma_w \delta V_{sc}(s) \tag{18}$$

Here M_w is the total amount of water in the system, W_s the ex-vessel steam flow and σ_w the (constant) water density. Eqs.(16) and (17) determine the steam density in the vessel which is directly related to the pressure:

$$\delta D = D_\sigma \delta\sigma_s = D_\sigma\left(\frac{1}{V_{s0}}\delta M_{sv}(s) - \frac{\sigma_s}{V_{s0}}\delta V_{sv}(s)\right) \tag{19}$$

with $D_\sigma = 1/\sigma_D$ the ratio between steam pressure and steam density fluctuations and V_{s0} the steady state steam volume in the vessel. In these equations it is assumed that the steam remains in saturation condition; the variations in steam volume and mass are assumed slow with respect to the time constants involved in the evaporation process (which may be considered much smaller than τ_s).
The steam flow W_s, introduced in Eq.(16) is determined by vessel pressure via the pressure control system and the external steam flow fluctuations δW_e :

$$\delta W_s(s) = C(s)\delta D(s) + \delta W_e(s) \tag{20}$$

where C(s) is the controller transfer function discussed in A3.3.
Finally the relations for the feedback reactivity have to be established to close the feedback loops in the model. Three processes are involved: fuel temperature (via nuclear Doppler effect) and moderator temperature and core void content (via moderator density and neutron spectrum effects). The relations hold

$$\delta\rho_{fb} = \delta\rho_1 + \delta\rho_2 + \delta\rho_3 \tag{21}$$

with

$$\delta\rho_1 = \rho_f \delta T_f \tag{22a}$$

$$\delta\rho_2 = \rho_m \delta T_m \tag{22b}$$

$$\delta\rho_3 = \rho_\alpha \delta\alpha \tag{22c}$$

ρ_f, ρ_m and ρ_α are the fuel temperature, moderator temperature and core void reactivity coefficients. Moderator temperature has not been included directly

into the model but it is coupled to the pressure via changes in the boiling temperature:

$$\delta T_m = T_D \delta D \qquad (23)$$

At this point all the necessary relations between the variables in the model have been established, except for the evaluation of the parameters involved. These are discussed in the next section. The relation between the variables is illustrated by Fig.A3.2. All relations can be gathered into transfer functions from the input variables ($\delta\rho_e$ and δW_e) to the other variables, of which we shall regard the power P and pressure D. The derivations of these transfer functions will not be shown here; results are discussed in section A3.4.

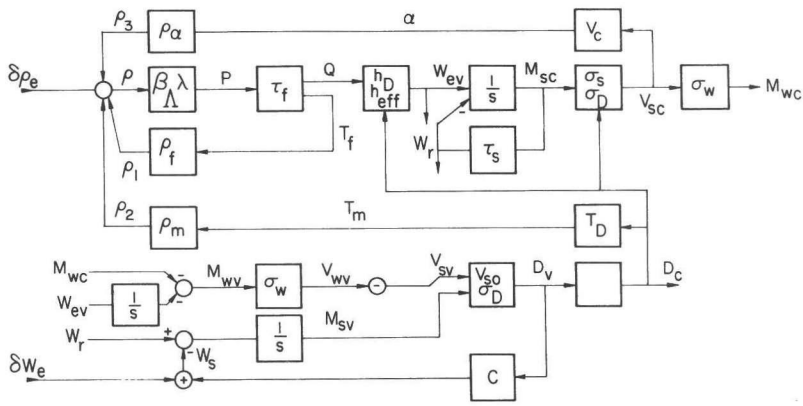

Fig.A3.2 Block diagram of the reactor model.

A3.3. Evaluation of model parameters.

In this section the parameters that were introduced in the model equations (1)-(23) will be evaluated. The parameters are based on nominal operating conditions: P_0=164MW, D_0=70bar, T_m=285°C, α_0=0.35 and W_{so}=71kg/s=255t/hr. Also end-of-cycle (EOC) conditions are assumed with an average burnup of 16MWd/kgU at which most experiments were performed.

Neutronic parameters. These are the neutron generation time Λ and the delayed neutron parameters β_i and λ_i. The neutron generation time is only of influence in the higher frequencies (above 10 Hz) which are not of primary interest in the present situation; a value of 50μs is assumed. The values for β_i and λ_i for the several fissionable isotopes are known (2). The main problem affecting the effective delayed fraction β is the relative contribution to power production of ^{235}U and ^{239}Pu fission. These fraction can be obtained from cross section and burnup calculations (3). Resulting values are β=0.62% (begin-of-cycle

(BOC), burnup 9.4MWd/kg, 26% Pu-fission) to 0.58% (EOC, burnup 16MWd/kg, 37% Pu-fission).

Fuel time constants. The most simple model for the heat transfer from fuel to coolant is a single time constant model: the response of fuel temperature and heat current on a power step is given by an exponential function $\exp(-t/\tau_f)$. The fuel time constant τ_f is determined by heat transfer coefficient k_{fc} and heat capacity C_f. k_{fc} can be obtained from average fuel temperature and power density. The design values for the Dodewaard reactor (4) give an average fuel temperature of 500/590°C at nominal power (fresh core/EOC). The heat capacity of UO_2 is approx 0.33 J/kg°C (5) which gives a time constant of 4.6 to 6.5 sec. The use of this time constant in the model leads to unsatisfactory results; the thermohydraulic feedback appears too slow with respect to measurements (see Ch. 5 and App. 1).

A more detailed analysis of the heat transfer gives rise to smaller time constants. Heat removal from the fuel is established by heat diffusion through the UO_2 pellets, the fuel-to-cladding gap, the cladding and the boiling film. This is a distributed parameter system of which the response to power fluctuations can better be approximated by a multi-time constant model. Iriarte (6) gives some approximate results. To obtain more accurate values a computer program was written that solves the stationary and time- dependent heat diffusion equation in the fuel pin. Values for fuel and zircaloy heat diffusion coefficients and specific heats were taken from Ref.5. Values for gap conduction and boiling heat transfer were taken from the design values (4) (k_{gap}=0.4W/cm²°C and k_{film}=1.4W/cm²°C). The stationary temperature profiles were calculated for three conditions:

1. Nominal power (155W/cm).
2. Nominal power, closed gap.
3. 270 % overpower (574W/cm).

The second case is motivated by the fact that in irradiated fuel (due to swelling and thermal expansion) the gap may become closed and heat transfer improves substantially; this is a realistic end-of-cycle condition. The third case is performed as a check on the correctness of the data used. A total power peak factor 3.7 is the design overpower at which no fuel melting may occur.

For case 1 and 2 a stepwise power decrease of 5% from nominal was introduced and the surface heat flux relaxation computed. The results enabled the fitting of two time constants to the response, leading to a fuel heat transfer function (see Eqs.(6) and (7))

$$G_f(s) = A_{f1}/(1+s\tau_{f1}) + A_{f2}/(1+s\tau_{f2}) \qquad (24)$$

From the observed mean fuel temperature, together with power and heat capacity

estimate also a single time constant τ_f can be obtained. Results of the calculations are given in Table A3.1.

The maximum fuel (centre) temperature is below the UO_2 melting point (approx. 2840°C) for case 3. The average fuel temperatures agree with Ref.4 for nominal power. This validates the model and data used. For the dynamic behaviour, it can be seen that the closure of the gap causes a smaller time constant and lower temperatures. Furthermore, the two time constant model exhibits a substantial faster heat transfer than the single time constant model; for case 2 even more than for case 1. This effect will give rise to higher frequencies involved in the reactivity feedback; it is discussed further in Sect.A3.4. An indication that these estimates are realistic is found in measurements of fuel response with a fuel elongation meter, which indicate a relative fast response (7) although no accurate results are available (8).

case	$T_{f,\delta avg}$ (°C)	$T_{f,\delta max}$ (°C)	τ (s)	A_{f1}	τ_{f1} (s)	A_{f2}	τ_{f2} (s)
1	580	760	6.5	0.88	7.9	0.12	1.2
2	470	615	4.1	0.77	5.4	0.23	0.8
3	1725	2580	8.6				

Table A3.1 Calculated fuel temperatures, time constants and fractions (see text).

Steam parameters. The steam densities and the dependence on pressure can easily be obtained from steam tables (9). For nominal conditions σ_s=36.5kg/m³, σ_w=740kg/m³ and σ_D=0.58kg/m³bar. The effective evaporation heat h_{eff} is obtained from the power and steam flow and amounts 2.31 10^6J/kg. This has to be compared with the amount of energy required to heat the water from feedwater temperature (approx. 130°C) to 285°C plus evaporation (which is estimated from Ref.9) to be 2.23 10^6J/kg.

For the pressure dependence of h, the variations of boiling temperature and of evaporation heat with pressure have to be taken into account. Both are included in the net steam enthalpy; from steam tables h_D=-1250J/kg,bar.

In the model also the volumina V_c and V_{so} are necessary. V_c is the water plus steam volume within the elements, V_c=2.05m³. V_{so}, based on the vessel volume left by an effective water level of 0.5m above chimney with no further components in the vessel, is 22.3m³.

Core steam removal. A fluctuation in the heat flow Q causes an instantaneous variation in the void content of the core. The void fluctuation profile has approximately the same shape as the axial power distribution. The void is swept from the core by the coolant flow through the bundles; the upper part of

the void very soon after its generation and the lower part after a residence time determined by velocity profile and core dimension. An exact solution of the steam removal requires a quite complicated analysis with knowledge of power and velocity profile. A simplified model for steam removal is the exponential decay

$$\delta M_{sc}(t)=\delta M_{sc}(0)\exp(-t/\tau_s) \tag{25}$$

where the time constant τ_s can be considered as the average steam residence time in the core. This approach has been used by other authors (10,11) and will be used in the present model. The steam time constant can be calculated by a simple balance of production and removal in the steady state:

$$W_{ro} = M_{so}/\tau_s = W_{evo} = P_o/h_{eff} \tag{26}$$

$$M_{so} = \alpha_o V_c \sigma_s \tag{27}$$

$$\tau_s = \frac{1}{P_o} h_{eff} \alpha_o V_c \sigma_s \tag{28}$$

Note that τ_s is a parameter in the linearised model and is dependent on operating conditions. The relations between reactor power and void fraction, as obtained in the thermohydraulic analysis of the core (4), will predict the variation of τ_s with power level. For nominal conditions τ_s=0.34s. This value can also be interpreted as the time, required for the steam transport from half core height (0.9m) to core top (1.8m) with an average steam velocity of 2.65m/s. This value agrees well with measurements of the void velocity profile (12 and Chapter 4).

Reactivity coefficients. The reactivity feedback in the model is determined by three reactivity coefficients, accounting for the effects of fuel temperature (ρ_f), moderator temperature (ρ_m) and moderator void fraction (ρ_α). The transfer functions resulting from the model are very sensitive to the reactivity coefficients so an accurate estimation is required.
The fuel temperature coefficient ρ_f is due to the nuclear Doppler effect in the resonance absorption in ^{238}U. It is mainly determined by fuel geometry and moderator-to-fuel-ratio and it is fairly independent on precise fuel conditions (enrichment,burn-up) due to the low enrichment of LWR fuel. The value of -2pcm/^{o}C obtained as design value (13) may thus be considered reasonable. This coefficient is however of minor importance with respect to the other two.
The moderator temperature and void fraction reactivity coefficients are generally larger. Both are related to changes in the moderator density σ_m and, as a second order effect, the thermal neutron spectrum. This spectrum varies due to density variations (large effect) and directly due to neutron temperature vari-

ations (smaller effect and neglected). Because of this same origin the two coefficients can be discussed simultaneously:

$$\rho_m = \frac{\partial \rho}{\partial T_m} = \frac{d\rho}{d\sigma_m}\frac{\partial \sigma_m}{\partial T_m} \tag{29}$$

$$\rho_\alpha = \frac{\partial \rho}{\partial \alpha} = \frac{d\rho}{d\sigma_m}\frac{\partial \sigma_m}{\partial \alpha} \tag{30}$$

with ρ the reactivity and σ_m the moderator density. Using the water density σ_w, it is obtained

$$\sigma_m = (1-\alpha)\sigma_w \tag{31}$$

$$\frac{\partial \sigma_m}{\partial \alpha} = -\sigma_w \tag{32}$$

$$\frac{\partial \sigma_m}{\partial T_m} = (1-\alpha)\frac{d\sigma_w}{dT_m} \tag{33}$$

The quantity determining the reactivity effect is the moderator density coefficient $d\rho/d\sigma_m$. Values for ρ_α and ρ_m can be found in the design report (13). These coefficients are, however, very sensitive to enrichment, burnup, control rod positions, poison and void fraction. Since reactor startup several changes in fuel and operating conditions have occured so that the design values are not reliable. Several methods will be used to obtain good values: theoretically via cross section calculations, experimentally from low-power temperature coefficient measurements and from control rod movements.

Neutron cross section calculations are executed for fuel management and operation purposes. These calculations give the infinite medium multiplication constant k_{inf}, neutron migration area M^2, thermal neutron diffusion length L and several other variables, for different burnup and void conditions. From these data we obtain the reactivity coefficients as follows. First, compute the control buckling B_c^2 (to be distinguished from the core geometrical buckling B^2) so that

$$k_{eff} = k_{inf}/(1+M^2B^2)(1+L^2B_c^2) \tag{34}$$

equals unity for operational conditions (α_0=0.35). B_c^2 counts for the control rod reactivity worth in the core. For varying void fraction, k_{eff} can be calculated by Eq.(34). Using available data (cross sections for α=0, 0.35 and 0.70) a parabolic fit of k_{eff} as function of α is possible, from which the void reactivity coefficient ρ_α is obtained. With the use of Eqs.(29)-(33) and the temperature dependence of the water density (9) the moderator temperature coefficient ρ_m is also gained. Results are shown in Table A3.2. A check on the obtained results can be found from an extrapolation of the calculated temperature coefficient to low temperature, BOC conditions for which measured data are

available (15). From Table A3.2 it is obtained that $\rho_\alpha(\alpha=0$, BU=9.2MWd/kg) is -0.057. For water at 285°C, σ_w=736kg and $d\sigma_w/dT$ at 50°C is -0.46kg/m³°C; this gives a value for ρ_m at 50°C of -3.6pcm/°C which is to be compared with -3pcm/°C from Ref.15 (although this last figure includes the zero-power Doppler reactivity and measurements at the begin of various cycles may differ by a factor two).

A third way to estimate ρ_α is from the control rod experiment (Appendix 1) which results in a value of -0.09. This value is in very good agreement with the other results.

The moderator temperature coefficient used in the model calculations can be easily derived from the void coefficient. In the model calculations the value actually used is the sum of ρ_m and ρ_f to compensate for the fact that, in the model, moderator temperature changes do not affect fuel temperature so an underestimation of reactivity feedback results. The model calculations were done with the values ρ_α=-0.093, ρ_m=-17.5pcm/°C and ρ_f=-2pcm/°C, unless mentioned otherwise.

para-meter	Burnup (MWd/kg U/Pu) 5.6	9.2	12.0	16.4
$\alpha=0$				
k_{inf}	1.218	1.170	1.134	1.075
$M^2(cm^2)$	59.3	59.4	59.6	59.8
$L^2(cm^2)$	6.69	6.75	6.83	7.05
$\alpha=0.35$				
k_{inf}	1.209	1.164	1.131	1.079
$M^2(cm^2)$	83.3	83.4	83.5	83.8
$L^2(cm^2)$	8.43	8.41	8.45	8.62
$\alpha=0.7$				
k_{inf}	1.185	1.143	1.115	1.070
$M^2(cm^2)$	134.	134.	134.	134.
$L^2(cm^2)$	11.9	11.7	11.6	11.6
$B_c^2(cm^{-2})$	0.016	0.011	0.007	0.001
$k_{eff}(\alpha=0)$	1.051	1.041	1.032	1.017
$k_{eff}(\alpha=0.7)$	0.901	0.917	0.930	0.952
$\rho_\alpha(\alpha=0)$	-0.077	-0.057	-0.037	-0.004
$\rho_\alpha(\alpha=0.35)$	-0.216	-0.177	-0.146	-0.093

Table A3.2 Neutronic parameters as function of burnup and void fraction.

Pressure control. The pressure control system is the main controller of the reactor during normal operation. Power is kept constant due to the negative void reactivity, as long as pressure fluctuations are suppressed. A general outline of the controller can be found in (16). The controller input is a pressure sensor on the main steam line. The signal is filtered to decrease the higher frequency variations and then input to an electro/hydraulical servo system. The steam flow from reactor vessel to turbine is regulated by two parallel control valves. As a strong nonlinear relation between valve opening and steam flow exists, valve characteristics and controller behaviour are dependent on operating conditions. Overall controller gain (steam flow variation divided by input pressure variation) has to be established by measurements, for which the control rod experiment (Appendix 1) and noise measurements (Ch.6) are suited. The dynamic behaviour (filter characteristics, break frequencies of amplifiers, etc) are obtained from these experiments, from documentation and from separate experiments. The general structure of the controller transfer function is

$$C(s) = \frac{D_o}{W_{so}} \frac{\delta W_s(s)}{\delta D(s)} = A_c K_c H_f(s) H_b(s) \qquad (35)$$

which gives the relation between (normalised) steam flow variations and (normalised) pressure fluctuations. A_c is the static gain from pressure fluctuations to valve position variations, the valve coefficient K_c is the ratio of flow variations to valve position variations, $H_f(s)$ the active filter transfer function and $H_b(s)$ the filtering due to the upper break frequencies of the several components. A_c and K_c are dependent on operating conditions. H_f has the general form

$$H_f(s) = (1+s\tau_{c1})/(1+s\tau_{c2}) \qquad (36)$$

For H_b ,in practice, a few time constants can be distinguished with values in the range of 0.03 to 0.20 s (17). In the model calculations the effect of H_b was neglected.

Using the data of several sources the values for A_c, K_c, τ_{c2} and τ_{c2} are given in Table A3.3. It is clear that different sources give rather different values. For the gains this may be understood by different operating conditions. For the time constants the cause is not clear. It has to be commented that for Ref.16 the values are nominal ones from the original electronic schemes; the measurements of Ref.17 were performed to check the actual values. The effect of different values of the pressure controller parameters is discussed in A3.4.

A complication to the pressure control system is that the controller input pressure sensor is not on the reactor vessel but on the main steam line, just before the control valves. This introduces a flow-dependent pressure drop

Ref.	Condition	A_c	K_c	τ_{c1} (s)	τ_{c2} (s)
16	164 MW	3.1		1.65	3.3
	144 MW	2.3		1.65	3.3
17	62% valve	10.6			
	34% ope-			0.9	6.4
	74% ning			1.6	3.0
App.1	144 MW	4.5	0.86	-	13.
Chap.6	164 MW	2.0	0.5	-	6.0
	144 MW		1.1		

Table A3.3 Pressure controller parameters estimated from different sources.

between vessel and controlled pressure of approx. 2.2bar at normal conditions. This effect is accounted for in the model. Characteristics of both vessel pressure and controlled pressure are evaluated in A3.4.

Apart from the actively controlled steam flow a natural control path exists. Pressure increase gives rise to a larger mass flow at constant valve position. This natural regulation has to be added to the effect of the controller. For the flow from the vessel to the (vacuum) condenser the following relation holds

$$D=A\sigma_s v_s^2 = \frac{B}{\sigma_s} W_s^2 \qquad (37)$$

from which can be derived

$$\frac{\delta W_s}{W_{s0}} = 0.5\left[\frac{\sigma_D}{\sigma_s}D_0+1\right]\frac{\delta D}{D_0} = 1.06\frac{\delta D}{D_0} \qquad (38)$$

Pressure propagation. It was assumed throughout this section that vessel pressure fluctuations immediately affect the core pressure. This is of course not completely true; apart from the (very fast) acoustic pressure transmission through the reactor water, the core steam content has to be compressed to meet the changed vessel pressure. This process is not very fast as an amount of water has to be transported. A very simple model regards the core steam volume as a spring and the amount of water in the core and chimney as inertial mass. This system has a resonance frequency of approx.25Hz, if the difference in flow area in the chimney and in the bundles is taken into account. It can be concluded that in the frequency range of interest the core pressure fluctuations may be considered equal to the vessel pressure fluctuations.

A3.4. Results.

Using the model developed in the previous sections the transfer functions between input and output variables may be computed. The effect of variations or inaccuracies in the different parameters can also be obtained. The input variables considered are reactivity and steam flow perturbations; the outputs are reactor power, vessel pressure and controlled pressure.

A parameter study was performed for void reactivity coefficient ρ_α, fuel time constants and controller parameters. For eight different cases the transfer functions were calculated:

0. Zero-power, P_0=1mW
1. P_0=164MW, ρ_α=-0.093, A_cK_c=4.0, τ_{c1}=13s, τ_{c2}=1.5s, τ_{f1}=5.4s, A_{f1}=0.77, τ_{f2}=0.8, A_{f2}=0.23 (standard conditions)
2. ρ_α=-0.18
3. τ_{f1}=4.1s, A_{f1}=1.0
4. τ_{f1}=7.9s, A_{f1}=0.88, τ_{f2}=1.2s, A_{f2}=0.12
5. τ_{c1}=3.3s
6. τ_{c1}=3.3s, A_cK_c=8.0
7. P_0=123MW.

The resulting transfer functions are shown in Figs A3.3 to A3.7. They are all based on normalised signals: fluctuations of power, pressure and flow relative to their stationary values. Reactivity is of course absolute.

The reactivity to power transfer function or generally called the reactivity transfer function (RTF) is shown in Figs A3.3 and A3.4. The reactivity feedback causes a strong decrease with decreasing frequency, compared to the zero-power RTF. In the region 0.5 to 2 Hz an increase is observed, with a maximum of 220 reached at 0.6 Hz. A study of the effect of changes in different parameters leads to the following conclusions.

-An increase of void coefficient causes an increase of the maximum to 250 at 0.7 Hz due to the stronger positive feedback in this region.

-The use of the single time constant fuel transfer function (case 3) gives a peak at lower frequencies; the peak height remains nearly unchanged. This can be understood from the larger effective time constant. The time constants have no effect on the RTF at very low frequencies. A same tendency is observed when the open-gap time constants are used (case 4). The RTF decreases a little at low frequencies due to the higher fuel temperature variations with associated doppler reactivity.

-For lower power conditions the feedback becomes smaller everywhere; the resulting RTF is larger in the low frequency region and less peaked.

-The effect of variations in pressure controller parameters is studied in Fig.A3.4. It appears that the effect on the RTF is very small.

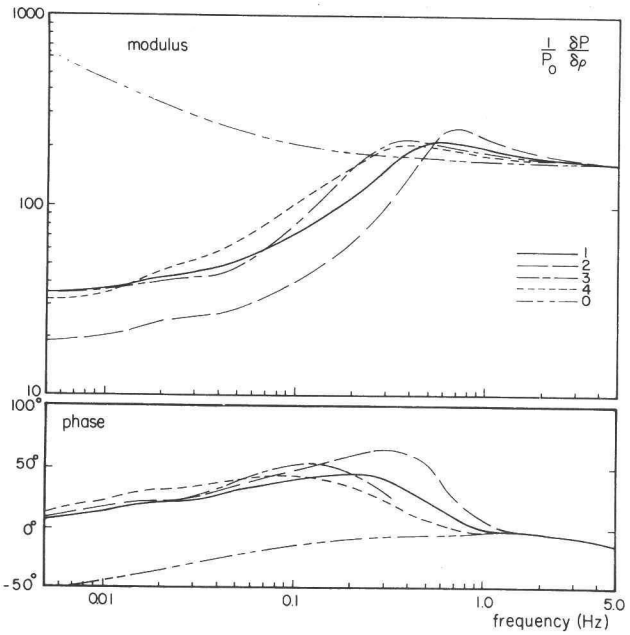

Fig. A3.3
Normalised transfer functions from reactivity to power (cases 0,1,2,3,4).

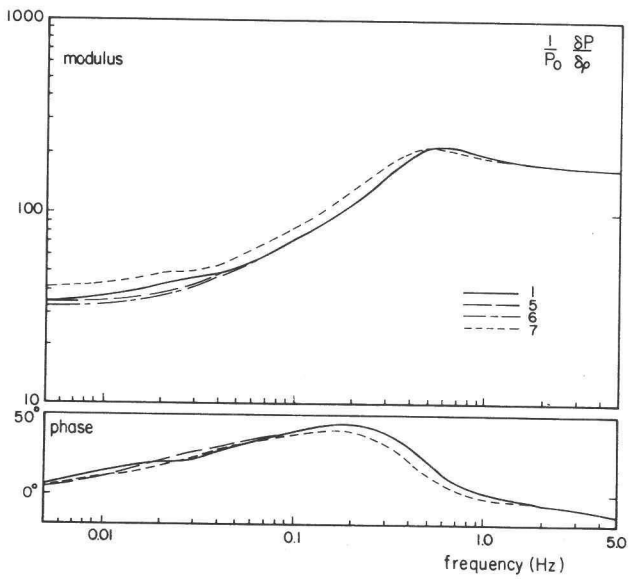

Fig. A3.4
Normalised transfer functions from reactivity to power (cases 1,5,6,7).

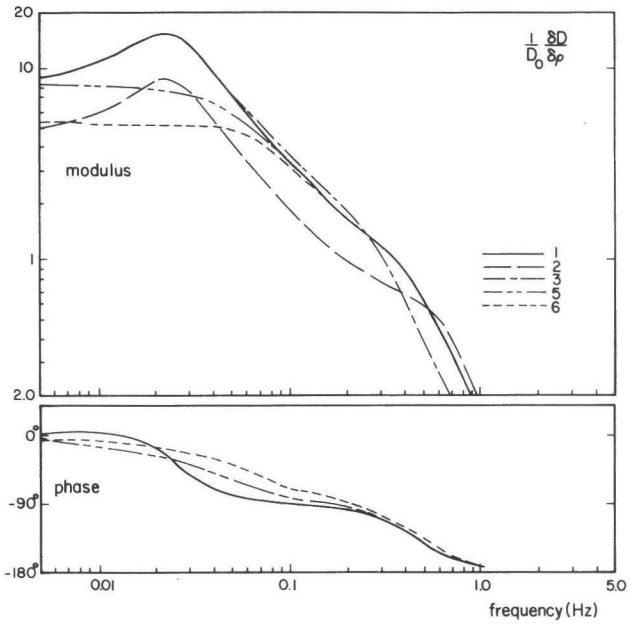

Fig.A3.5
Normalised transfer functions from reactivity to pressure.

The transfer function of reactivity to vessel pressure is shown in Fig.A3.5. In general it decreases strongly with frequency due to the integrating behaviour of fuel heat capacity and vessel volume. At low frequencies the fluctuations are suppressed by the control system. In case 1 and 2 the break frequency of the controller is only 0.012 Hz so that higher frequencies are not sufficiently removed. This causes a peak at 0.025 Hz in the pressure fluctuations. For the cases 5 and 6 with a faster controller this effect is not present. The influence of ρ_α and fuel time constants on the behaviour can be understood from the changes in power (thus steam) production due to the changes in the RTF. The response of the controlled pressure to reactivity changes is very similar to that of the vessel pressure; results are not shown.

The transfer functions of steam flow to power and pressure are given by Figs A3.6 and A3.7. The integrating character of the vessel for steam flow changes is clear; the changes in suppression of pressure noise with controller parameters too. The influence of the reactivity coefficient may be understood from the associated change in RTF and the larger reactivity effect caused by void compression. For the controlled pressure the effect of a flow- dependent pressure drop becomes visible above 0.1 Hz in Fig.A3.7.

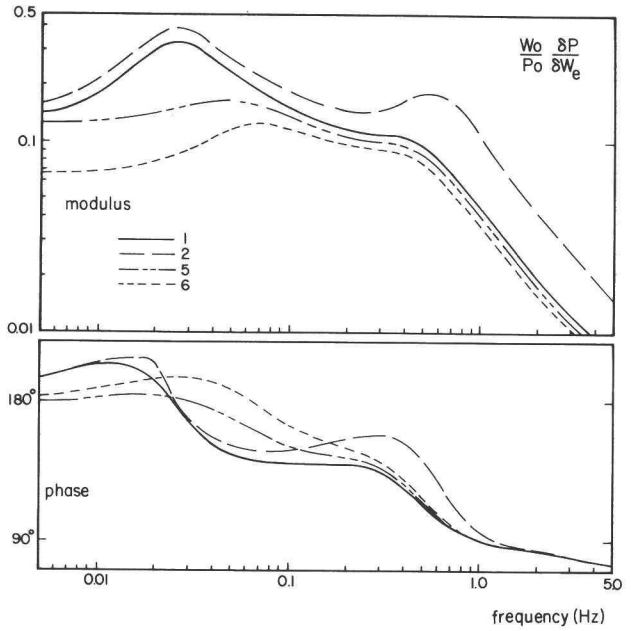

Fig. A3.6
Normalised transfer functions from steam flow to power.

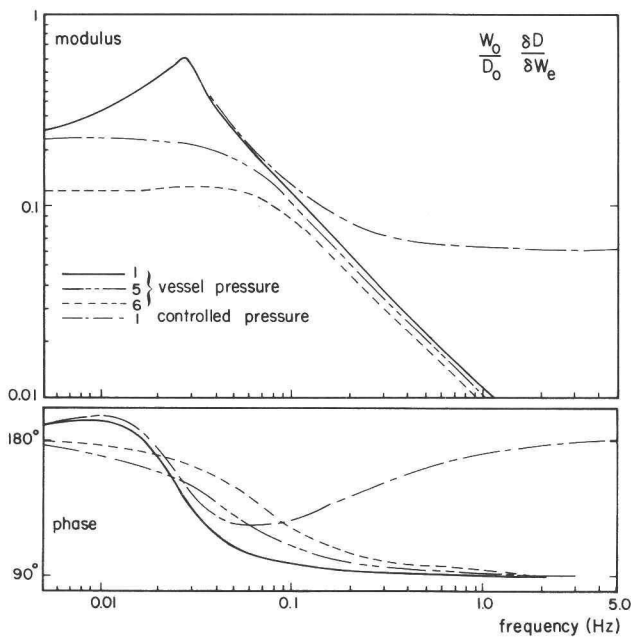

Fig. A3.7
Normalised transfer functions from steam flow to pressure.

Concluding it can be stated that the model gives results that are physically understandable. Comparison with measurements (Chapter 5, Appendix 1) may validate the measurement results and furthermore clarify the effect of changes in the parameters. For instance, the experimentally determined RTF indicates that rather small fuel time constants may be present. Also the occurence of the 0.02 Hz pressure fluctuations, since long observed in the reactor, may be understood from a large controller time constant.

A3.References

1. Veer,J.H.C van der and E.B.J.Kleiss. Report IRI-131-79-02, IRI, Delft, (1979). (In Dutch).
2. Lewins,J. Nuclear reactor kinetics and control, Pergamon Press, (1978).
3. Bruggink,J. Private communication (1978).
4. Thermohydraulics design report. J.Hoekstra, private communication.
5. Fenech,H.(ed.) Heat transfer and fluid flow in nuclear systems, Pergamon Press (1981).
6. Iriarte,M.Jr. Nu.Sci.Eng 7,26-32 (1960).
7. Nissen,W.H.M. Private communication (1982).
8. Veer,J.H.C.van der, Report 9907-81,Kema,Arnhem (1981).(In Dutch).
9. Handbook of Chemistry and Physics, 60th ed. CRC-press (1979).
10. Matthey,M. Progress in Nuclear Energy 1,151-162 (1977)
11. Veer,J.H.C.van der. Progress in Nucl.Energy 9,607-618,(1982)
12. Kleiss,E.B.J. Report IRI-131-79-03, IRI, Delft (1979).(In Dutch).
13. Physics design report. J.Hoekstra, private communication.
14. Oosterkamp,J.W. Private communication (1982).
15. Bruggink,J.C.(1980), by private communication with J.Hoekstra.
16. Klei,J.W. Report 272, vakgroep Meet- en Regeltechniek, Afd. Werktuigbouwkunde, TH Delft (1981).(In Dutch).
17. A.Noels and J.H.C.van der Veer. Private communication (1982).

P	Thermal power	164MW
D_c, D_v	Core, Vessel pressure	70bar
W_s	Steam flow to turbine	70.6kg/s
T_m	Core water temperature	285°C
T_D	Pressure derivative of T_m	1.0°C/bar
h_{eff}	Effective evaporation enthalpy	2.31 10^6J/kg
h_D	Pressure derivative of h_{eff}	-1250J/kg/bar
V_c	Core water+steam volume	2.05m³
V_{so}	Steam volume in vessel	22.3m³
α	Core void fraction	0.35
τ_s	Steam residence time in core	0.34s
σ_w	Water density	740kg/m³
σ_s	Steam density	36.5kg/m³
σ_D	Pressure derivative of σ_s	0.58kg/m³/bar
ρ_f	Doppler reactivity coefficient	-2pcm/°C
ρ_m	Moderator temperature coefficient	-18pcm/°C
ρ_α	Void reactivity coefficient	-0.09
τ_{f1}, τ_{f2}	Fuel time constants	see A3.4
A_{f1}, A_{f2}	Contributing fractions of τ_{f1}, τ_{f2}	id.
τ_{c1}, τ_{c2}	Controller time constants	id.
A_c	Controller gain	id.
K_c	Valve coefficient	id.
β_i, λ_i	Delayed neutron parameters	see Ref.2
Λ	Neutron generation time	50μs

Table A3.4 Symbols and used values of the main model parameters/variables.

NAWOORD.

Bij het afsluiten van mijn promotie-onderzoek wil ik eenieder bedanken die bijgedragen heeft aan de totstandkoming van dit proefschrift.
Mijn promotor, prof.dr.ir.H. van Dam ben ik erkentelijk voor de mogelijkheid binnen de vakgroep reactorfysica van het Interuniversitair Reactor Instituut te kunnen werken en voor zijn stimulerende begeleiding, die me toch veel zelfstandigheid liet. Eduard Hoogenboom dank ik voor de nuttige discussies en het nauwgezet doorlezen van het concept van dit proefschrift. Piet de Leege, Jelle Schut, Jan de Roode, Dick Veldhuis en Dick de Haas hebben vaak extra hun best voor me gedaan. Zij en mijn overige collega's, binnen en buiten de vakgroep reactorfysica, waren altijd belangstellend en behulpzaam bij de (soms vele) voorkomende problemen en zorgden voor een plezierige werksfeer.
De directie van de Gemeenschappelijke Kernenergiecentrale Nederland ben ik erkentelijk voor de geboden gelegenheid om onderzoek te verrichten in de centrale te Dodewaard. De heren J.Hoekstra en W.J.Oosterkamp waren altijd vol interesse en bereid over vele zaken van gedachten te wisselen. W.Nissen, G. van Bernebeek en W. de Zeeuw dank ik voor hun enthousiaste en bereidwillige medewerking bij de experimenten en het stillen van mijn honger naar informatie en documentatie. Met name van Wim Nissen heb ik veel hulp gehad. Ook met J. van der Veer heb ik vaak uitstekend kunnen samenwerken. Nita Brands verzorgde snel en netjes de vele tekeningen en dhr.A.R.Suiters de foto's waarvoor ik hen dankzeg.
Tenslotte dank ik al mijn vrienden voor hun belangstelling en medeleven in deze, vaak drukke, periode.

STELLINGEN

I

De door Upadhyaya voorgestelde methode voor de correctie van correlaties in de met een autoregressief model gevonden ruisbronnen, berust niet op een correcte analyse van de oorzaken van de correlaties en leidt tot onjuiste resultaten.

-Upadhyaya,B.R., M.Kitamura and T.W.Kerlin. Ann.Nucl.Energy 7,1-11,(1980).
-Dit proefschrift, Appendix 2.

II

De door Bergdahl bij het analyseren van ruissignalen geconstateerde afhankelijkheid van de signaalvolgorde, berust waarschijnlijk op onvoldoende rekennauwkeurigheid van het gebruikte computerprogramma.

-Bergdahl,B.G. and R.Espefält. Progress in Nucl.Energy 9,149-160,(1982).

III

De betrouwbaarheid van de uit ruissignalen van neutronendetectoren verkregen stoomsnelheden in de splijtstofelementen van kokend-water reactoren, wordt beperkt door het ontbreken van experimenten waarbij de verkregen resultaten met onafhankelijke methoden geverifieerd worden.

-Behringer,K. and R.Crowe. Atomkernenergie 38,47-57,(1981).

IV

Ook voor kerncentrales geldt, dat de grootste niet de beste behoeven te zijn.

V

Het testen van computerprogramma's door aanbiedende programmabibliotheken zou dienen te geschieden met gelijksoortige computers en compilers als die, waarvoor de programma's bedoeld zijn.

VI

Een van de oorzaken van de oppositie tegen kernenergie is het conservatisme bij de veiligheidsanalyses, waarbij door gebrek aan voldoende nauwkeurige gegevens, de gevolgen van allerlei gebeurtenissen te ernstig worden ingeschat.

VII

Het beschikbaar komen van betere gegevens, als bedoeld in stelling VI, maakt het mogelijk om conservatieve marges te verkleinen en veiligheidseisen te verlichten, met gunstige economische gevolgen voor de centrales. Dit zal echter de publieke acceptatie van kernenergie niet vergemakkelijken.

-Levinson,M. and F.Rahn. Nuclear Technology 53,99-110,(1981).

VIII

Bij (brede maatschappelijke) discussies over energie lijkt de wet van behoud ervan wel eens te worden vergeten.

IX

De toepassing van polariserend glas in koplampen, voorruiten en spiegels van auto's kan de verblinding bij nachtelijk verkeer verminderen.

X

De populariteit van klimmuren als trainingsmogelijkheid voor alpinisten vereist een herwaardering van het begrip geveltoerisme.

XI

De opkomst van het 'free climbing' binnen het alpinisme is een weerspiegeling van de veranderende waardering voor techniek in de samenleving.

Delft, 16 juni 1983

Erik Kleiss